DEUTSCHES ELEKTRONEN-SYNCHROTRON DESY

DESY 81-003
January 1981

SELECTED TOPICS IN e^+e^- PHYSICS

by

Sau Lan Wu
Department of Physics, University of Wisconsin, Madison, Wisconsin, USA
and
Deutsches Elektronen-Synchrotron DESY, Hamburg

NOTKESTRASSE 85 · 2 HAMBURG 52

DESY 81-003
January 1981

SELECTED TOPICS IN e^+e^- PHYSICS*

by

Sau Lan Wu

Department of Physics, University of Wisconsin, Madison, Wisconsin, USA+

and

Deutsches Elektronen Synchrotron DESY, Hamburg, Germany.

Abstract: Selected topics of recent experimental results from the high-energy electron-positron storage rings are presented. The topics include some of the τ and charm physics from SPEAR, the upsilon physics from DORIS and CESR, and the $\gamma\gamma$ physics and quark and gluon physics from the PLUTO and TASSO Collaborations at PETRA. Related data from the JADE and MARK J Collaborations at PETRA are discussed in separated papers at this School.

* Rapporteur talk, Proceedings of the Arctic School of Physics, July 27 - August 7, 1980, Äkäslompolo, Lapland, Finland.

+ *Supported in part by the US Department of Energy, contract EY-76-C-02-0881.*

Content:

1. INTRODUCTION

During the last six years, since the discovery of J/ψ in 1974[1] much of the exciting experimental results in high-energy physics has come from electron-positron storage rings. In this heroic period of ample activity, we have learned in particular about a new quantum number charm[2], another new quantum number bottom[3], a heavy lepton τ[4], and quarks and gluons in the form of jets[5-11].

In 1978 the energy of DORIS was upgraded to just above 5 GeV in order to investigate the properties of the ϒ family. The other e^+e^- storage ring in Hamburg, PETRA (Positron-Electron Tandem Ring Accelerator) was proposed at the time of the J/ψ discovery and became operational in 1978. Almost exactly a year later, CESR (Cornell Electron Storage Ring) began to produce e^+e^- annihilation events. In 1980 PEP (Positron Electron Project) has become operational. Activities in this area of physics is phenomenal.

As indicated in the table of contents, the selected topics to be discussed are the τ and charm physics from SPEAR, the upsilon physics from DORIS and CESR, the γγ physics and the quark and gluon physics from PETRA. There are five detectors at PETRA, namely CELLO, JADE (JApan Deutschland and England), MARK J, PLUTO and TASSO (Two Arm Spectrometer SOlenoid, also Italian poet of the sixteen century). Of these five, the CELLO was moved into the beam only this year, while the results from the JADE and MARK J are going to be presented at this conference by Eichler and Pohl respectively. I shall therefore concentrate mostly on the PLUTO and TASSO results, so far as PETRA data are concerned.

We conclude this introduction with two topics of general interest.

A) Cross sections of e^+e^- physics are often expressed in terms of R

$$R = \frac{\text{cross section under consideration}}{\text{total cross section for } e^+e^- \rightarrow \mu^+\mu^-} \qquad (1.1)$$

at the same energy. More precisely, the denominator is not the actual total cross section for $e^+e^- \rightarrow \mu^+\mu^-$, but rather the theoretical total cross section in the lowest-order QED without weak interactions. This theoretical total cross section is

$$\sigma(e^+e^- \rightarrow \mu^+\mu^-) = \frac{2\pi\alpha^2}{3s}\beta(3 - \beta^2), \qquad (1.2)$$

where β is the velocity of the produced muons, and the mass of the electron has been neglected. (α is the fine-structure constant and s is the square of the center-of-mass energy). In (1.2) the factor $\beta(3-\beta^2)$ is extremely close to 2; it is for example $(2\text{-}10^{-4})$ for a beam energy of 1 GeV. Replacing this factor by 2 and the result is

$$\sigma(e^+e^- \to \mu^+\mu^-) = \frac{86.856}{s}\ \text{nb} \qquad (1.3)$$

with s in units of GeV^2. Thus R is really

$$R = \frac{1}{86.856}\ (s \text{ in GeV}^2)\ (\text{cross section under consideration in nb}) \qquad (1.4)$$

As a specific example, the η inclusive cross section has been given in terms of nanobarns by DASP (Double-Arm Spectrometer) at DORIS and in terms of R by the Crystal Ball at SPEAR. Comparison requires conversion through (1.4)

B) All the existing e^+e^- storage rings are essentially circular in shape. The electrons and positrons usually move in opposite directions within the same vacuum pipe under the same guiding magnetic field, DORIS being the most noteworthy exception when operating below the maximum energy. The main limitation in energy is due to synchrotron radiation from the electrons and positrons. It is for this reason that there is now a proposal from SLAC to build a single-pass linear collider, thus avoiding synchrotron radiation.

There is however a benefit from synchrotron radiation. Because of the guiding magnetic field, electrons with spin antiparallel to the magnetic field have lower energy than those parallel to the magnetic field. Because of synchrotron radiation, the electrons eventually become predominately antiparallel and the positron parallel to the magnetic field. Theoretically[12], the polarization buildup as a function of time is given by

$$P(t) = P_o\,(1 - e^{-t/t_o}) \qquad (1.5)$$

where $$P_o = \frac{8}{5\sqrt{3}} = 92.4\% \qquad (1.6)$$

and $$t_o = \frac{8}{5\sqrt{3}}\ \frac{\alpha}{r_o^2}\ \frac{\rho^2 R}{\gamma 5}\ \frac{1}{c} \qquad (1.7)$$

In (1.7), $r_o \sim 2.818 \times 10^{-13}$ cm is the classical radius of the electron, ρ is the bending radius and R the average radius of the guiding field, γ is the ratio of the beam energy to the electron mass and c is of course the velocity of light. For example, at E = 15 GeV, the PETRA and PEP time constant t_o is about 20 minutes.

In writin down the theoretical expectations (1.5) - (1.7), we have ignored complications due to machine resonances, which tend to destroy the polarization. Recent experimental measurements on the electron-beam polarization at PETRA[12] are shown in Fig. 1.1, where the beam energy is 15.2 GeV. This measurement is obtained through backward Compton scattering by a circularly polarized photon beam, converted from a linearly polarized laser pulse from an argon laser by a Pockels crystal. The helicity of the photon beam can be easily changed by reversing the high voltage applied to the Pockels crystal. The vertical coordinate in Fig. 1.1 is

$$V_a = \frac{n_R - n_L}{n_R + n_L} \qquad (1.8)$$

where n_R and n_L are the number of back-scattered photons with suitable cuts where the incident laser beam is right- and left-handed respectively. The relation between V_a and the polarization of the electron beam is not simple; the observed polarization at 15.2 GeV without the depolarizer, is (40±10)%. This is considerably lower than the theoretical maximum value of 92.4% in (1.6). In fact, if the energy of the electron beam is increased by 100 MeV to 15.3 GeV, a nearby machine resonance destroys the polarization completely.

2. NEW RESULTS FROM SPEAR

In what is referred to as the standard model, there are three families of quarks and leptons:

$$\begin{pmatrix} u \\ d \\ \nu_e \\ e \end{pmatrix} \quad \begin{pmatrix} c \\ s \\ \nu_\mu \\ \mu \end{pmatrix} \quad \begin{pmatrix} t \\ b \\ \nu_\tau \\ \tau \end{pmatrix} \qquad (2.1)$$

In each family, there are in order a quark of baryon number 1/3 and charge 2/3, a quark of baryon number 1/3 and charge -1/3, a neutral lepton, and a charged lepton. The quarks are supposed to be available in three colors, while the leptons are color singlets.

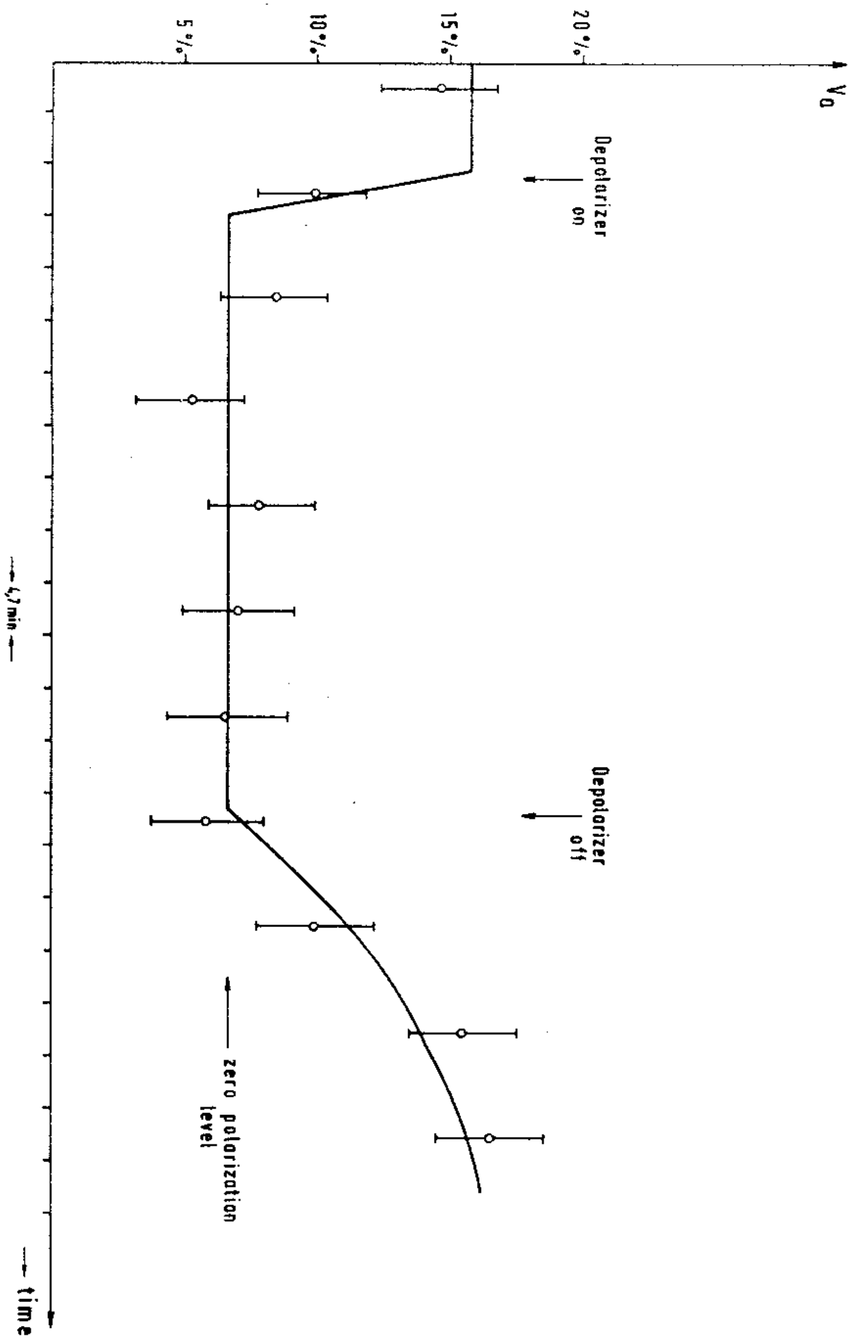

fig. 11

Fig. 1.1 Polarization of the electron beam at PETRA. The beam at 15.2 GeV is depolarized by a fast depolarizing device. After switching off this device the polarization builds up again.

Since the SPEAR energy is insufficient to produce particles with b quantum number, their investigation concentrates on the τ lepton and particles associated with the quantum number of charm c. Some of the recent experimental results are presented in this order here.

2.1 τ-decay

The branching ratio of the Cabibbo favored decay mode

$$\tau \to \rho \nu \qquad (2.2)$$

was reported by the DASP Collaboration at DORIS several years ago[13]. Recently, this branching ratio was determined by MARK II[14] based on statistics larger than those previously published by DASP[15] and MARK II[16]. What is observed is

$$e^+e^- \to \tau^+\tau^-$$

with $\tau^\mp \to \left.\begin{matrix} e^\mp \\ \mu^\mp \end{matrix}\right\} + 2\nu$

and $\tau^\pm \to \pi^\pm\pi^0\nu$

As shown in Fig. 2.1 the $\rho^\pm$ peak is clearly present with very little background.

Similarly the Cabibbo suppressed decay mode,

$$\tau \to K^*(892)\nu \qquad (2.3)$$

has recently been seen for the first time by MARK II[14]. This is observed through

$$e^+e^- \to \tau^+\tau^-$$
$$\tau^\mp \to \left.\begin{matrix} e^\mp \\ \mu^\mp \end{matrix}\right) + 2\nu$$
$$\tau^\pm \to \pi^\pm K_S^0 \nu$$

The number of events is much less, but the K^* peak is still visible as shown in Fig. 2.2.

In Table 2.1 the branching ratios are given for the two leptonic decay modes[17] and the three two-body decay modes[14] so far observed. The theoretical branching ratios are of those of Tsai[18]. Although theoretically expected at the level of 0.5%, the decay mode $\tau^\pm \to K^\pm\nu$ has not yet been seen experimentally. In this table, to save excessive writing, $\tau^\pm \to \rho^\pm\nu$ means $\tau^+ \to \rho^{+}\bar{\nu}_\tau$ and $\tau^- \to \rho^-\nu_\tau$ for example.

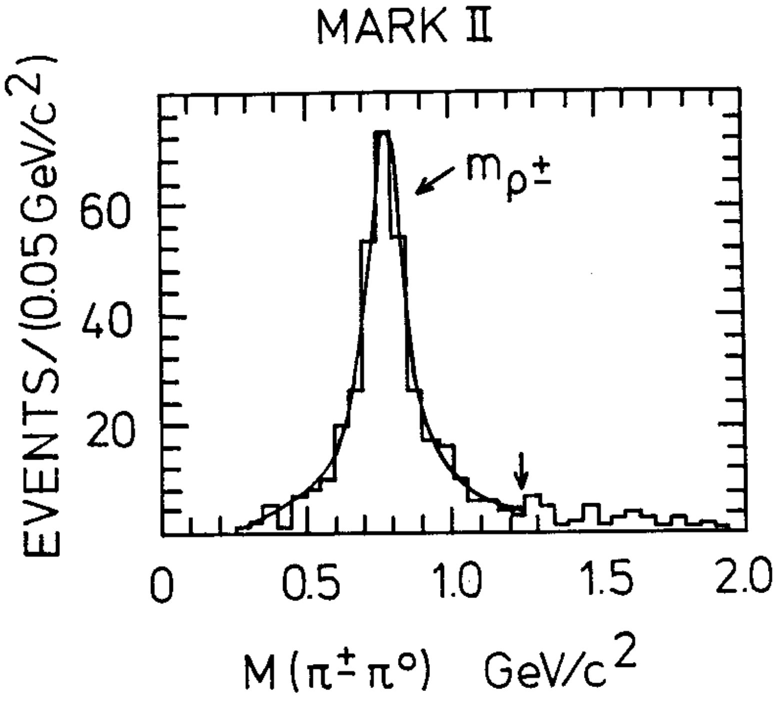

Fig. 2.1 - The $\pi^\pm\pi^0$ invariant mass spectrum for events which have a lepton at the primary vertex.

31885

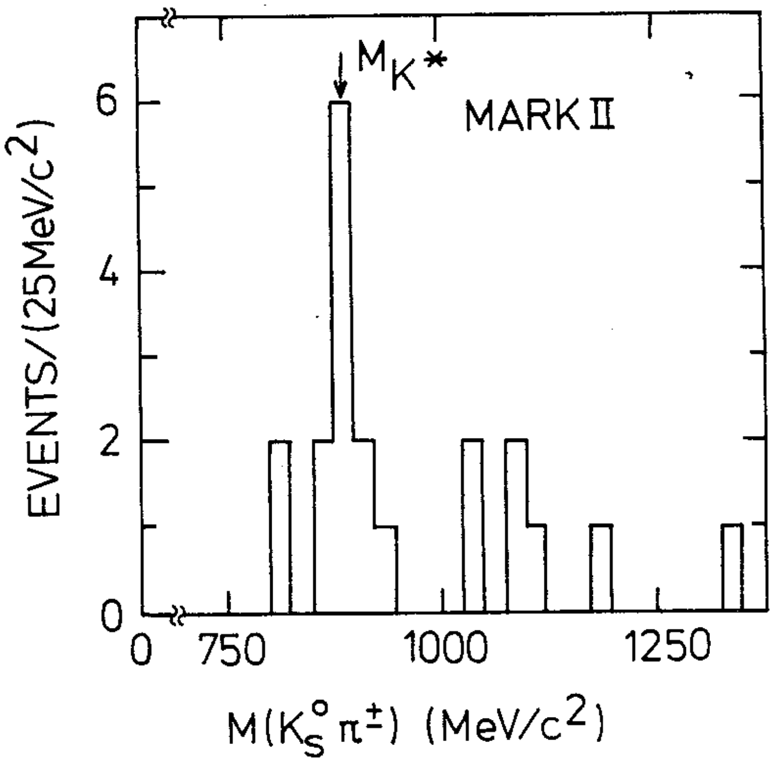

Fig. 2.2 - $K_S^0\pi^\pm$ invariant mass spectrum for events which have a lepton at the primary vertex.

31887

Theoretically, the ratio of these two modes observed recently can be easily understood by referring to the two quark diagrams of Fig. 2.3. Since the first one is Cabibbo favored and the second one Cabibbo suppressed, their ratio is

$$\frac{B(\tau^{\pm} \to K^{*\pm}\nu)}{B(\tau^{\pm} \to \rho^{\pm}\nu)} = \tan^2\theta_c \; f_{ps} \qquad (2.4)$$

where θ_c is the Cabibbo angle ($\tan^2\theta_c = 0.05$) and $f_{ps} = 0.93$ is a phase space factor. The data are thus in agreement with the standard model.

Table 2.1 - Observed single-channel decay modes of the tau lepton

Decay Mode	Branching ratio	
	experimental	theoretical
$\tau^{\pm} \to e^{\pm}\nu\nu$	$(17.5 \pm 1.1)\%$	17.6%
$\tau^{\pm} \to \mu^{\pm}\bar{\nu}\nu$	$(18.5 \pm 1.2)\%$	17.2%
$\tau^{\pm} \to \pi^{\pm}\nu$	$(9.1 \pm 1.1)\%$	10.5%
$\tau^{\pm} \to \rho^{\pm}\nu$	$(24.0 \pm 9.0)\%$ DASP	$(21.5 \pm 1.5)\%$
	$(21.6 \pm 1.8 \pm 3.2)\%$ MARK II	
$\tau^{\pm} \to K^{*\pm}(892)\nu$	$(1.7 \pm 0.7)\%$	$(1.0 \pm 0.1)\%$

2.2 Life time of $D^{\pm}$ and D^0 and their ratio

The D are the pseudoscalar mesons with charm quantum number but not strangeness quantum number. The quark content are supposed to be:
$D^+(c\bar{d})$, $D^0(c\bar{u})$, $\bar{D}^0(\bar{c}u)$, and $D^-(\bar{c}d)$. Numerous decay modes together with their branching ratios are known for these mesons. We restrict our discussions to their life times.

In the emulsion neutrinos experiment at FNAL, 10 neutral D's and 5 charged D's are observed. From these events the lifetimes τ_0 for D^0 and $\tau_{\pm}$ for $D^{\pm}$ are found to be[19,20]

$$\tau_0 = (1.01 \, {}^{+0.43}_{-0.27}) \times 10^{-13} \text{ sec.}$$

and

$$\tau_{\pm} = (10.3 \, {}^{+10.5}_{-\;4.1}) \times 10^{-13} \text{ sec.} \qquad (2.5)$$

Thus these two lifetimes are strikingly different. Their ratio is shown in Table 2.2.

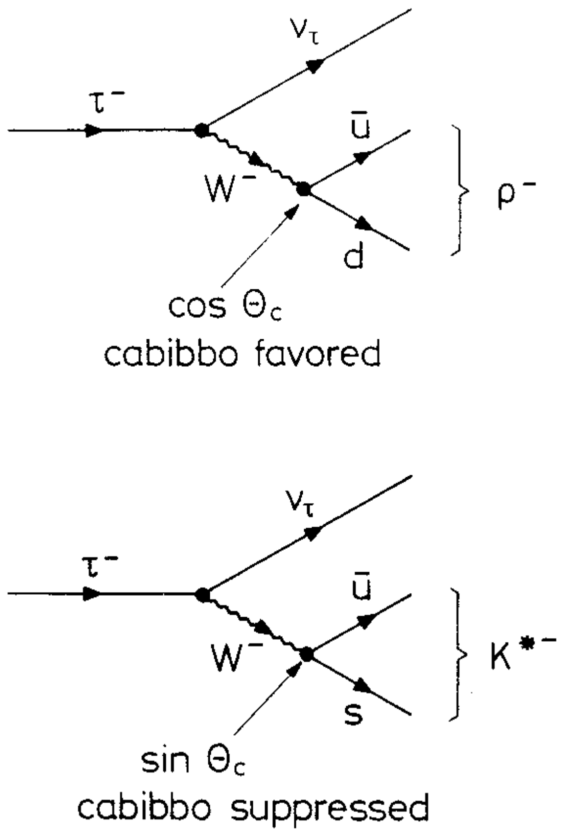

15.12.80

32106

Fig. 2.3 - Quark diagrams for the decays $\tau^- \to \rho^-\nu_\tau$ and $\tau^- \to K^{*-}\nu_\tau$ in the standard model.

This ratio of lifetime was first measured by DELCO[21] at SPEAR and more recently by MARK II[22]. The methods used are rather complicated, but the basic idea is to make use of the equality of the semi-leptonic widths of $D^\pm$ and D^0:

$$\Gamma_{SL}(D^\pm) = \Gamma_{SL}(D^0).$$

The theoretical reason is that, as shown in Fig. 2.4, the diagrams for these semileptonic decays are essentially identical. Accordingly,

$$\frac{\tau_\pm}{\tau_o} = \frac{\text{semi-leptonic branching ratio of } D^\pm}{\text{semi-leptonic branching ratio of } D^0} \qquad (2.6)$$

The DELCO and MARK II results are also shown in Table 2.2.

Table 2.2 - Ratio $\tau_\pm/\tau_o$ of the lifetimes of $D^\pm$ and D^0

DELCO	> 4.3 (95% C.L.)
Emulsion	$10 ^{+11}_{-5}$
MARK II	$3.1 ^{+4.6}_{-1.4}$

All three determinations of this ratio are in reasonable agreement with each other. In any case, $\tau_\pm$ is significantly larger than τ_o. The most reasonable theoretical explanation[23] of this difference is that, as shown in Fig. 2.5 there is only one diagram for the non-leptonic Cabibbo favored decay of D^+, while for D^0, there is an additional W-exchange diagram.

2.3 $F^\pm$

The F mesons, with both charm and strangeness quantum numbers, were first seen at DASP[24] through the decay mode

$$F^\pm \rightarrow \pi^\pm \eta.$$

Seven events were recorded with a mass of

$$(2030 \pm 60)\ \text{MeV}$$

Recently F has been seen in three separate experiments:

A) Photoproduction experiment with the Omega spectrometer at CERN (WA4) shows a peak in three channels[25] as shown in Fig. 2.6.

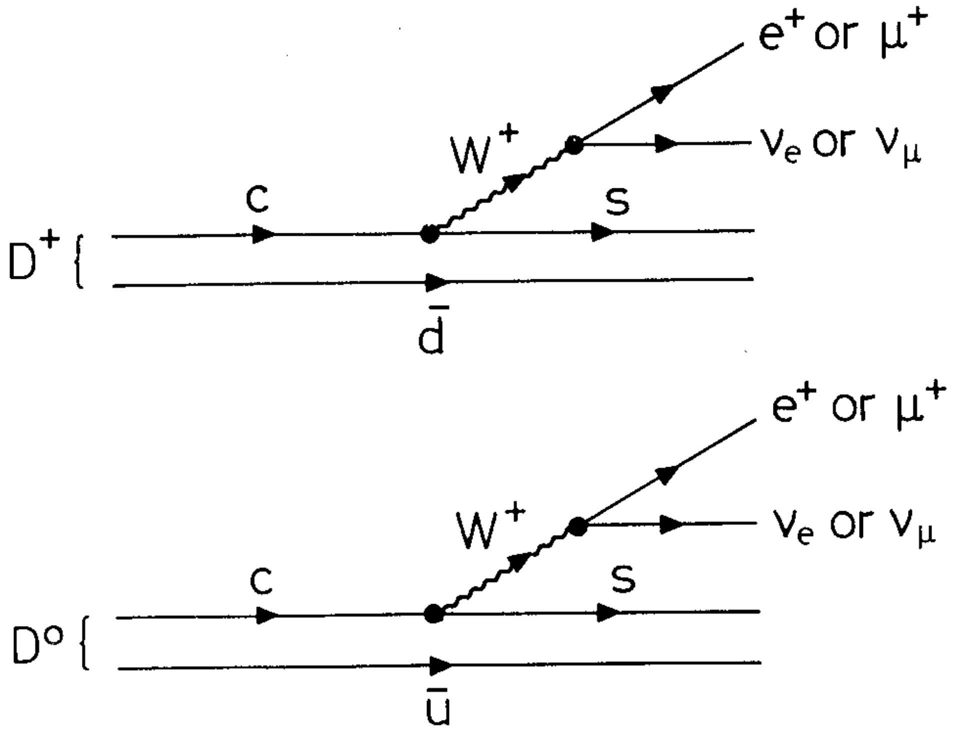

Fig. 2.4 - Quark diagrams for the semileptonic decay of the D mesons

31916

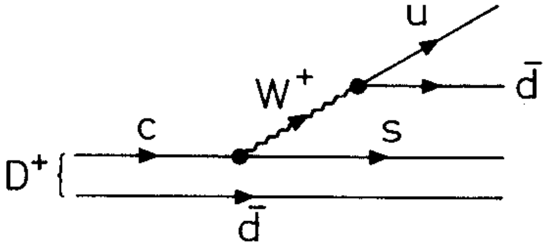

(a) D$^+$ decay

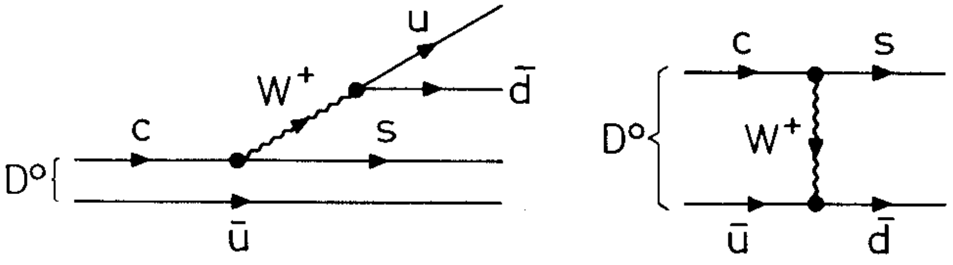

(b) D^o decay

31915

Fig. 2.5 - Quark diagrams for the non-leptonic decay of the D mesons.

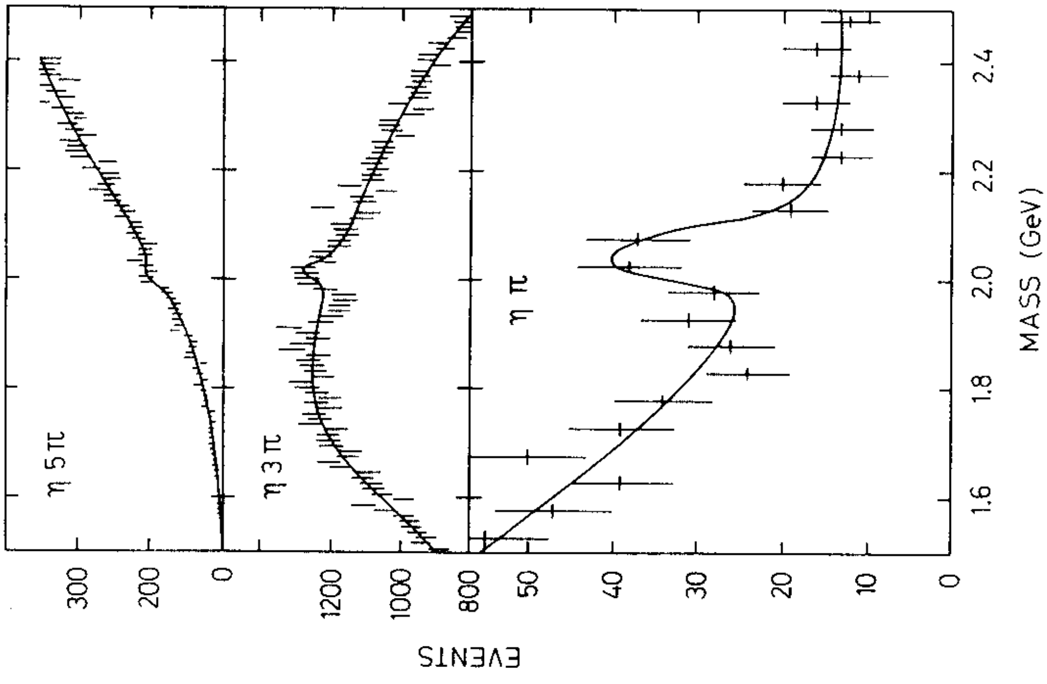

31910

Fig. 2.6 - Mass spectra of the η + nπ systems from WA4 experiment.

$\eta + \pi$	2047 ± 25 MeV
$\eta + 3\pi$	2021 ± 15 MeV
$\eta + 5\pi$	2008 ± 20 MeV.

The η's are identified by their 2γ decay mode. The majority of the F signal in the η5π system appears to come from the η'3π channel.

B) The emulsion experiment of Ushida et al. gives two events[19,20]:

$\pi^+\pi^-\pi^-\pi^0$ (2026 ± 56) MeV

and $K^+\pi^+\pi^-\bar{K}^0$ (2089 ± 121) MeV

C) The emulsion experiment of Ammar et al.[26] has one event:

$\pi^+\pi^+\pi^-\pi^0$ (2017 ± 25) MeV.

All these events are most naturally interpreted as F's and no reasonable alternative has been proposed.

The emulsion data (B) and (C) also give an estimate of F lifetime[23]

$$(2.0\ ^{+1.8}_{-0.8}) \times 10^{-13} \text{ sec.}$$

On the other hand, no evidence for F is seen by the Crystal Ball at SPEAR. The preliminary result[27] from Crystal Ball on R(η) as a function of center of mass energies is shown in Fig. 2.7 where R(η) is defined as

$$R(\eta) = \frac{\sigma(e^+e^- \to \eta X)}{\sigma(e^+e^- \to \mu^+\mu^-)}$$

This data on η inclusive production show neither threshold behavior near 4.1 GeV nor any indication of a peak near 4.4 GeV, in disagreement with the DASP data[24].

2.4 Radiative decay J/ψ

We next discuss a most interesting decay

$$J/\psi \to \gamma + \text{ordinary hadrons} \qquad (2.7)$$

By ordinary hadrons we mean hadrons not connected with charm; in fact, this adjective "ordinary" merely excludes the process

$$J/\psi \to \gamma + \eta_c \qquad (2.8)$$

to be discussed in section 2.5. Since the mass of η_c is quite close to that of J/ψ, the photon from (2.8) is quite soft, just over 100 MeV. Thus experimentally the process (2.8) is comfortably excluded by requiring the photon energy to be more than say, 300 MeV.

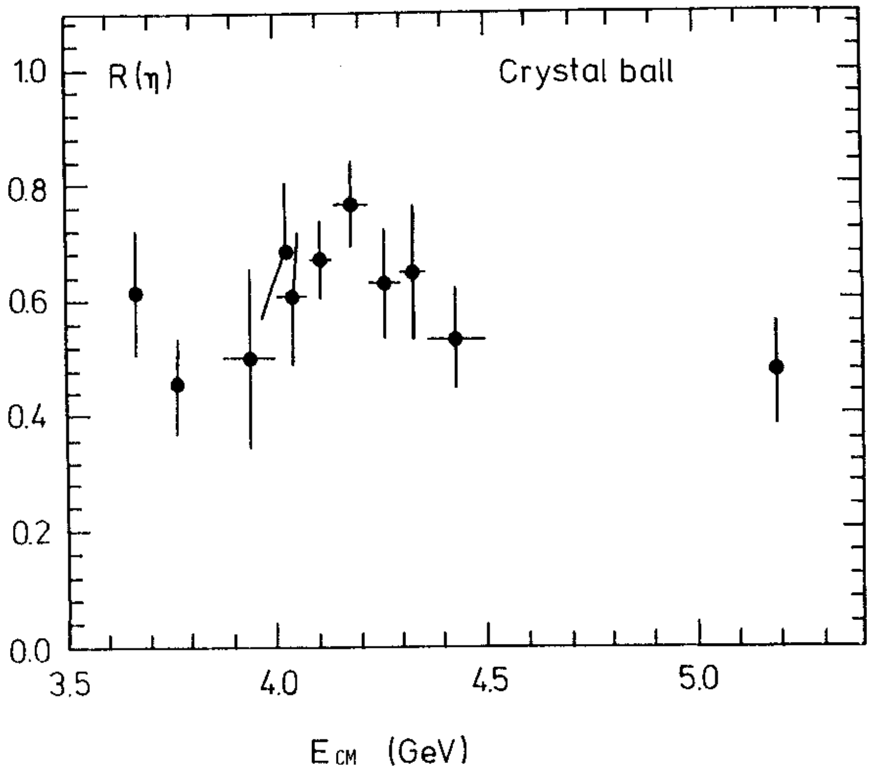

31903

Fig. 2.7 - Plot of ratio

$$R(\eta) = \frac{\sigma(e^+e^- \to \eta X)}{\sigma(e^+e^- \to \mu^+\mu^-)}$$

as a function of center-of-mass energy.

Consider first the inclusive process (2.7). Theoretically, this proceeds through the diagram of Fig. 2.8(a) as compared with that shown in Fig. 2.8(b) for $J/\psi \rightarrow$ hadrons, guaranteed to be ordinary hadrons. Because of the similarity of these two diagrams, their ratio is simply

$$\frac{\Gamma_{\gamma gg}}{\Gamma_{ggg}} = \frac{36}{5} \left(\frac{2}{3}\right)^2 \frac{\alpha}{\alpha_s} = 0.13, \qquad (2.9)$$

where 36/5 is a colour factor, 2/3 is due to charge of the charm quark, and α_s is the quark-gluon strong coupling constant. In getting the numerical value 0.13 above, α_s has been taken to be 0.18, as calculated from the ratio of the leptonic to the hadronic width of J/ψ[28]. It follows from (2.9) that the branching ratio for the process (2.7) is

$$B(J/\psi \rightarrow \gamma + \begin{smallmatrix}\text{ordinary}\\ \text{hadrons}\end{smallmatrix}) = 0.13\ (1+0.13)^{-1}\ [1-(R+2)B(J/\psi \rightarrow e^+e^-)-B(J/\psi \rightarrow \gamma\ \eta_c)] \quad (2.10)$$

with R = 2, $B(J/\psi \rightarrow e^+e^-) = 7\%$ and $B(J/\psi \rightarrow \gamma\eta_c) = 1\%$ (see section 2.5) we get

$$B(J/\psi \rightarrow \gamma + \text{ordinary hadrons}) \approx 0.08\ . \qquad (2.11)$$

A more detailed calculation shows that in leading order QCD the photon spectrum is approximately linear:

$$\frac{1}{N}\frac{dN}{dx} \sim 2x \qquad (2.12)$$

where $x = 2E_\gamma/m_{J/\psi}$.

We emphasize that the statements in the last paragraph are all theoretical. What is the actual situation ?

The recent data from MARK II are shown in Fig. 2.9, where the upper data points are from the total number of observed photons and the lower points are due to $\gamma\gamma$ decay modes of π^0 and η. The difference, shown in Fig. 2.10, gives the rate for the decay (2.7). Note that N_{tot} is the total number of observed photons and hence is not the N of (2.12). Also shown in Fig. 2.10 is the QCD result (2.12), with resolution taken into account. It is seen that the experimental data disagrees with this lowerst order QCD prediction.

The data for $x < 0.6$ have rather large error bars due to the subtraction. If the data for $x > 0.6$ are integrated, the result given by MARK II is

$$B(J/\psi \rightarrow \gamma + \text{hadrons with } 2E_\gamma/m_{J/\psi} > 0.6) = (4.1 \pm 0.8)\%. \qquad (2.13)$$

We next turn our attention to specific decay channels. The following decays have been clearly observed:

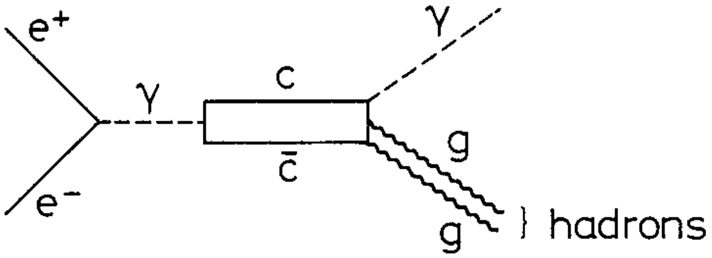

(a) $e^+e^- \rightarrow J/\psi \rightarrow \gamma$ +ordinary hadrons

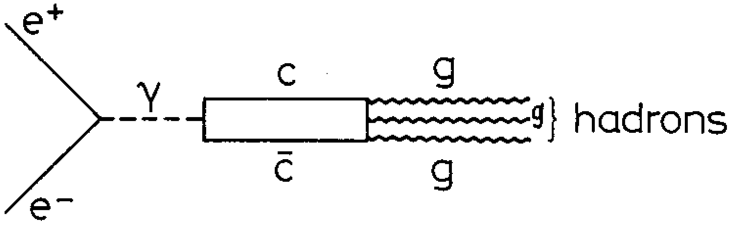

(b) $e^+e^- \rightarrow J/\psi \rightarrow$ hadrons

31913

Fig. 2.8 - Quark diagrams for some J/ψ decays.

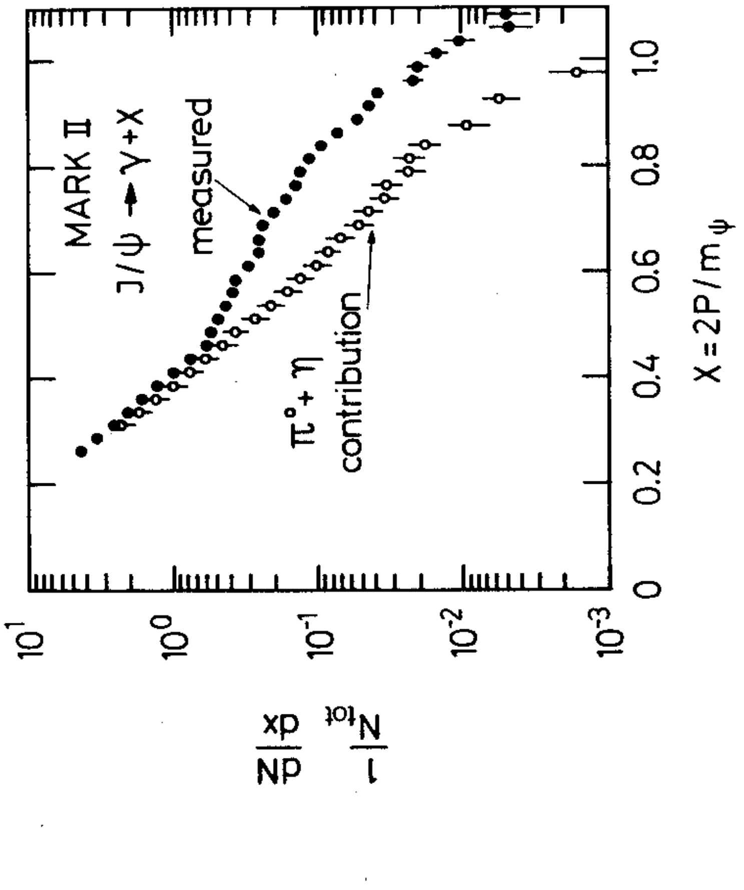

31886

Fig. 2.9 - Inclusive γ distribution, $(\frac{1}{N_{tot}})\frac{dN}{dx}$, as a function of x. The solid data points represent the measured γ spectrum and the open points represent the γ spectrum predicated from measurement of the π^0 and η distributions.

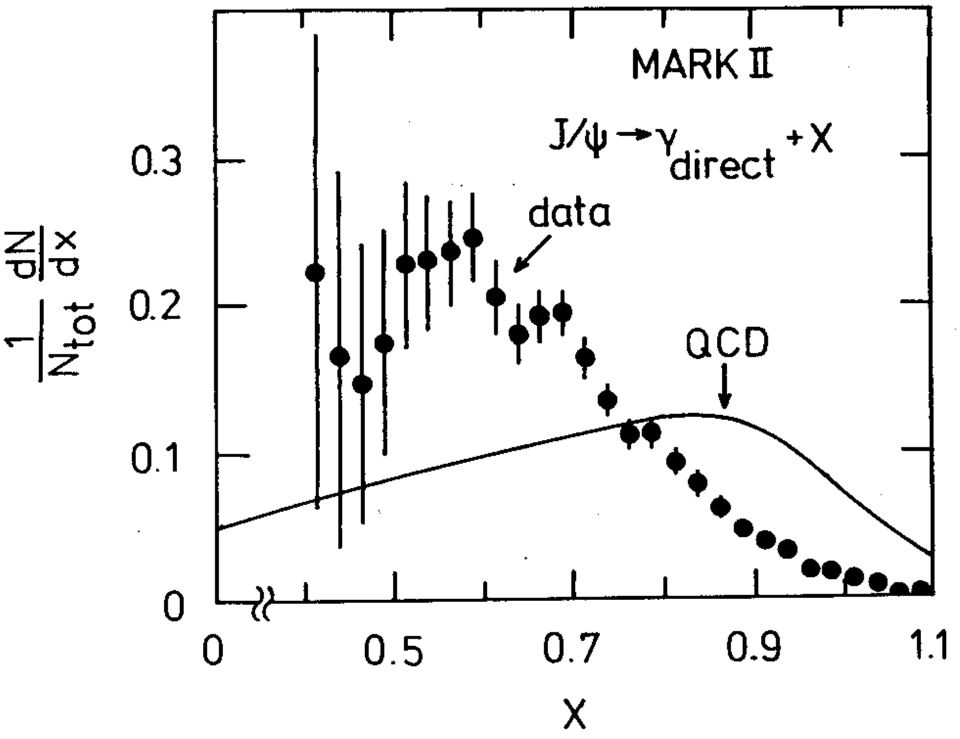

Fig. 2.10 - Direct photon momentum distribution. Curve shows the leading-order QCD prediction.

31889

$$J/\psi \rightarrow \gamma \eta$$
$$J/\psi \rightarrow \gamma \eta'$$
$$J/\psi \rightarrow \gamma + f(1270)$$

and very recently at SPEAR

$$J/\psi \rightarrow \gamma + E(1420) \quad .$$

The observed branching ratios are listed in Table 2.3.

Table 2.3 - Branching ratios for exclusive radiative decay of J/ψ

Decay	Mode seen	Branching ratio	Ref.
$J/\psi \rightarrow \gamma\pi^0$	$\gamma\gamma$	$(7 \pm 5) \times 10^{-5}$	DASP[29]
$J/\psi \rightarrow \gamma \eta$	$\gamma\gamma$	$(8 \pm 2) \times 10^{-4}$	DASP[29]
	$\gamma\gamma$	$(12 \pm 2) \times 10^{-4}$	Crystal Ball[31]
	$\gamma\gamma$	$(13 \pm 4) \times 10^{-4}$	DESY-Heidelberg[33]
	$\gamma\gamma$	$(9 \pm 4) \times 10^{-4}$	MARK II[32]
$J/\psi \rightarrow \gamma \eta'$	$\rho^0\gamma$	$(24 \pm 7) \times 10^{-4}$	DESY-Heidleberg[33]
	$\gamma\gamma$	$(69 \pm 17) \times 10^{-4}$	Crystal Ball[31]
	$\gamma\gamma$	$(22 \pm 17) \times 10^{-4}$	DASP[29]
	$\rho^0\gamma$	$(34 \pm 7) \times 10^{-4}$	MARK II[32]
$J/\psi \rightarrow \gamma f(1270)$	$\pi^+\pi^-$	$(20 \pm 3) \times 10^{-4}$	PLUTO[34]
	$\pi^+\pi^-$	$(15 \pm 4) \times 10^{-4}$	DASP[30]
	$\pi^+\pi^-$	$(13 \pm 3) \times 10^{-4}$	MARK II[32]
$J/\psi \rightarrow \gamma E(1420)$	$\eta\pi\pi$	$(23 \pm 15) \times 10^{-4}$ *	Crystal Ball[31]
	$K\bar{K}\pi^0$	$(34 \pm 24) \times 10^{-4}$ *	Crystal Ball[31]
	$K\bar{K}\pi^0$	$(36 \pm 14) \times 10^{-4}$ *	MARK II[32]

* These values are for $B(J/\psi \rightarrow \gamma + E(1420)) \times B(E(1420) \rightarrow \text{mode seen})$

The inclusive spectrum from the Crystal Ball is given in Fig. 2.11, showing the η, η' and E peaks. The data in connection with the decay into E are shown in Fig. 2.12 and Fig. 2.13 from the Crystal Ball and MARK II respectively. Although the indication with E(1420) is not completely certain, the mass and width observed by MARK II[35] are

$$M \; = \; 1440 \; {}^{+10}_{-15} \; \text{MeV}$$

and
$$\Gamma \; = \; 50 \; {}^{+30}_{-20} \; \text{MeV}$$

in good agreement with the E meson.

Since E meson is not one of the best known mesons, I copy here the information given in the Particle Properties Data Booklet of April 1980.

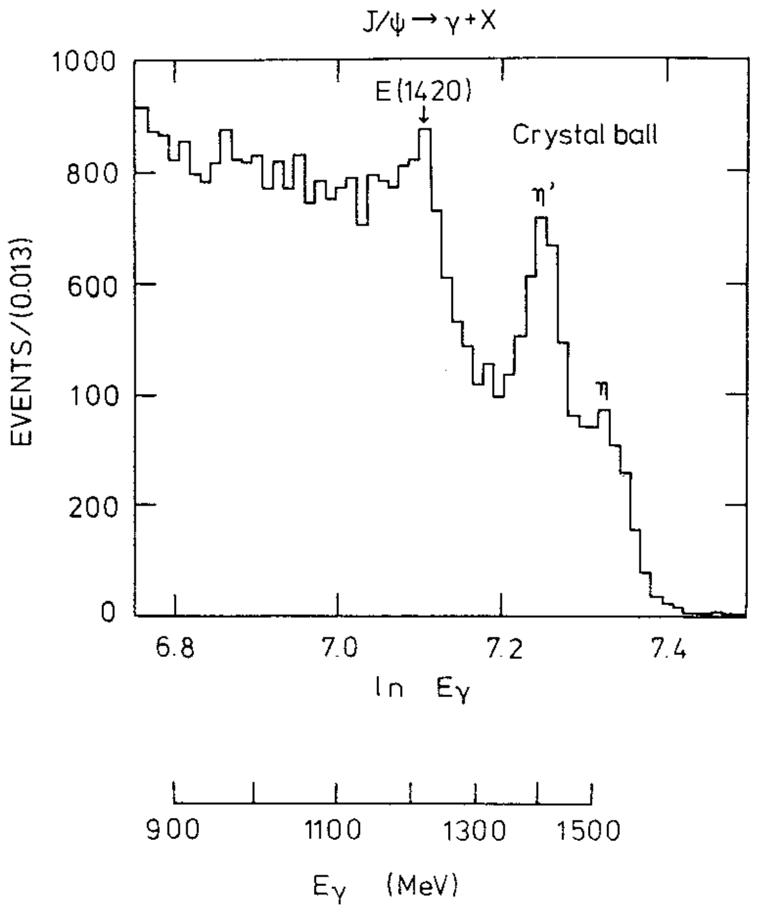

31896

Fig. 2.11 - The inclusive photon spectrum observed in J/ψ decays by the Crystal Ball Collaboration.

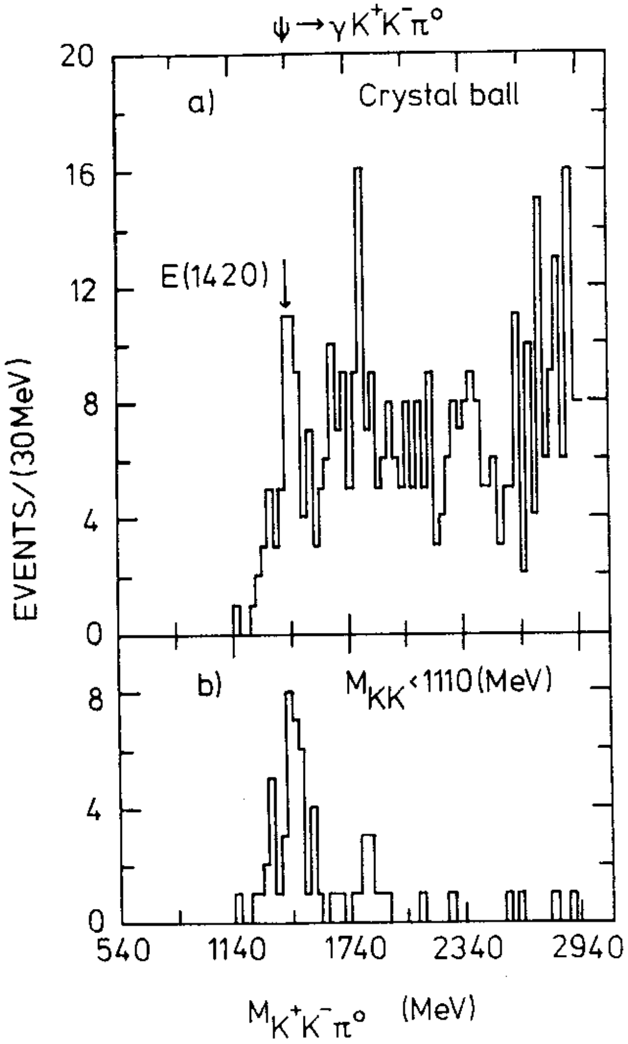

Fig. 2.12 - The $K^+K^-\pi^o$ mass spectrum for $J/\psi \rightarrow \gamma K^+K^-\pi^o$
a) no M_{KK} cut
b) for $M_{KK} < 1110$ MeV
from the Crystal Ball Collaboration.

31911

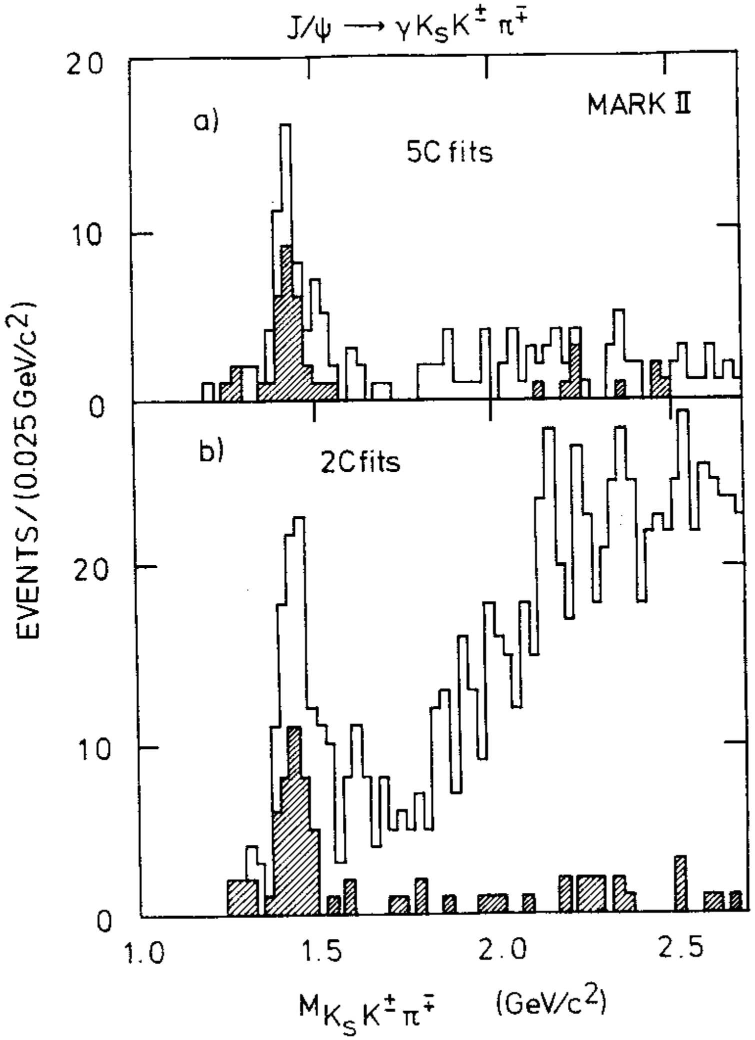

31909

Fig. 2.13 The $K_S K^{\pm} \pi^{\mp}$ mass spectrum for $J/\psi \rightarrow \gamma K_S K^{\pm} \pi^{\mp}$ candidate events which satisfy (a) a 5C fit to this hypothesis (b) a 2C fit (observation of the photon not required). Events in the shaded region have $m_{KK} < 1.05$ GeV. The data were obtained by the MARK II Collaboration.

E(1420) $I^G = 0^+$ $C = +$

$M = 1416 \pm 10$ MeV $\Gamma = 60 \pm 20$ MeV

Decay modes: $K\bar{K}\pi$ (prob. $K^*K^- + \bar{K}^*K$) seen

$\eta\pi\pi$ possibly seen

$\delta\pi$ possibly seen

The E meson is not a well established resonance. One can see that the information is rather meager. Here δ(980) is a well established resonance that decays into $K\bar{K}$ and $\pi\pi$.

Since E(1420) is a rather obscure resonance, why is there any special interest in the decay $J/\psi \to \gamma E$? This is due to a very interesting but somewhat speculative argument of Scharre et al.[35,36] that E meson may be a glueball. The underlying reason for giving such an argument is the purely theoretical observation that, as shown in Fig. 2.8(a) the decay $J/\psi \to \gamma$ + hadrons is a good place to look for glueballs. Their argument is briefly as follows:

i) The branching ratio for $J/\psi \to \gamma E$ is unexpectedly large and is comparable to that of $J/\psi \to \gamma\,\eta'$, as already shown in Table 2.3.

ii) The corresponding ratio for $J/\psi \to \gamma + D(1285)$ is much smaller:

$$B(J/\psi \to \gamma D)\, B(D \to K\bar{K}\pi) < 7 \times 10^{-4} \qquad (2.14)$$

from MARK II[35]. The production of E and D are comparable in hadronic reactions and D is believed to be a 1^+ state.

iii) If the spin-parity of E is 0^-, then in SU(3) there is no place for E without starting another nonet. The first 0^- nonet is already full and consists of $\pi^\pm$, π^0, $K^\pm$, K^0, $\bar{K}^0$, η and η'.

We look forward to clarification of this question whether E is a glueball, including especially the determination of the spin of E meson.

2.5 η_c

The η_c candidate state was first observed by the Crystal Ball Collaboration[37] at SPEAR with a mass of 2978 ± 9 MeV and a natural line width < 20 MeV. Radiative transitions to this state are observed from ψ'(3684) and J/ψ(3095) in the inclusive photon spectra. Fig. 2.14 shows the inclusive photon spectrum obtained from hadronic decays of the ψ'. The transitions to the well known χ states are indicated in the figure. A clear signal of greater than 5 standard deviation is seen at $E_\gamma = 634 \pm 13$ MeV which corresponds to a

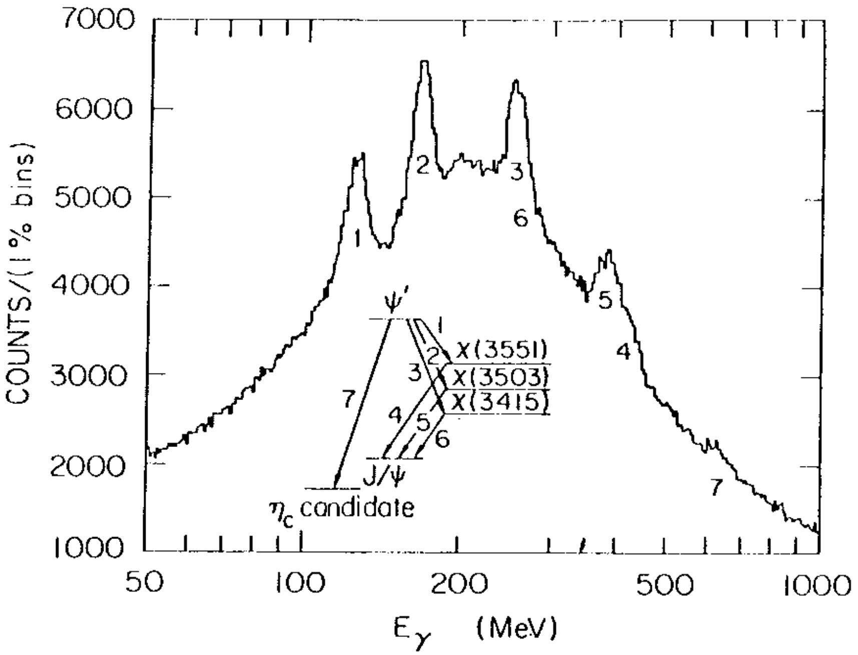

Fig. 2.14 - The inclusive photon spectrum from ψ' hadronic decays obtained by the Crystal Ball Collaboration. Counts are plotted in logarithmic bins since the resolution, ΔE/E, is nearly constant in E from NaI (Tl).

31898

transition to a state of mass = 2983 ± 16 MeV.

If the signal from the ψ' decay corresponds to the M1 transition $\psi' \to \gamma\,\eta_c$ then one would expect a signal at $E_\gamma \approx$ 110 MeV for $J/\psi \to \gamma\,\eta_c$. Fig. 2.15 shows the inclusive photon spectra from (a) ψ' decay and (b) J/ψ decay in the region of η_c before and after background subtraction. The best fits to these data give

$$M_{\eta_c} = 2981 \pm 15 \text{ MeV}, \quad \Gamma = 20\,^{+16}_{-11} \text{ MeV}.$$

The Crystal Ball Collaboration also obtained signals for the exclusive decays of $\eta_c \to \gamma\,\eta\,\pi^+\pi^-$ from events with three photons and two charged particles. Fig. 2.16 shows the energy spectrum of the low-energy photon for events which fit the $J/\psi \to \gamma\,\eta\,\pi^+\pi^-$ hypothesis. The peak of the photon spectrum corresponds to a η_c mass of 2974 ± 9 MeV and a line width of < 20 MeV.

Corroborating evidence also comes from MARK II[38] at SPEAR. MARK II obtains at state of mass 2980 MeV/c^2 which decays into several identified hadronic final states. The states chosen for study are the following:

$$\psi' \to \gamma\, p\bar{p}$$
$$\psi' \to \gamma\, \pi^+\pi^-\pi^+\pi^-$$
$$\psi' \to \gamma\, \pi^+\pi^-\, K^+K^-$$
$$\psi' \to \gamma\, \pi^+\pi^-\, p\bar{p}$$
$$\psi' \to \gamma\, K^\pm\, \pi^\mp\, K_S \quad (K_S \to \pi^+\pi^-)$$

Fig. 2.17 shows the hadronic mass spectrum from the background corrected direct-photon events. The results of a detailed analysis give

$$M_{\eta_c} = (2980 \pm 8) \text{ MeV}$$
$$\Gamma < 40 \text{ MeV} \quad (90\% \text{ confidence level}).$$

Properties of the η_c from the Crystal Ball and MARK II are listed in Table 2.4.

There are other interesting recent results from SPEAR concerning charm. Two examples of this topic that have not been summarized here are the properties of D^* mesons[39] and the branching ratios of the D mesons.[40]

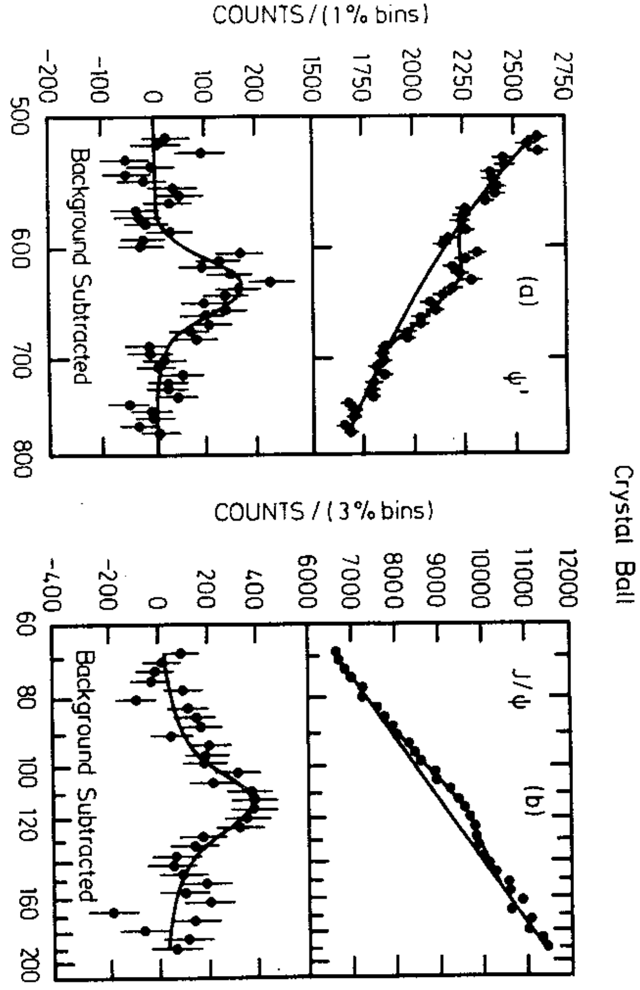

Fig. 2.15 - Inclusive photon spectra from (a) ψ' and (b) J/ψ decays in the region of the η_c with fit results overplotted (Γ = 20 MeV). Unsubtracted and background subtracted spectra are shown.

31890

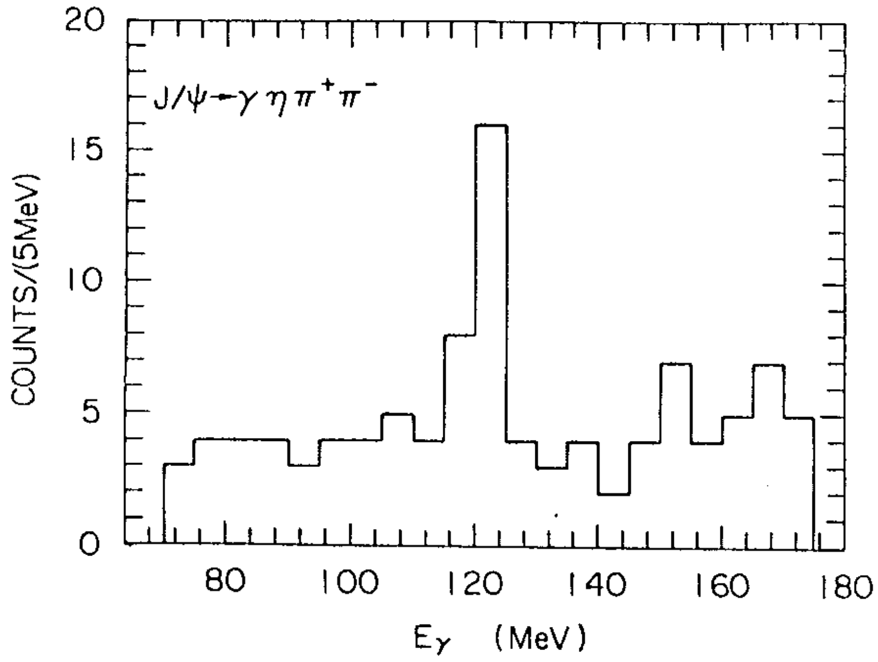

Fig. 2.16 - Fitted energy of the photon for events fitted to the hypothesis $J/\psi \to \gamma \eta \pi^+ \pi^-$ from Crystal Ball.

31897

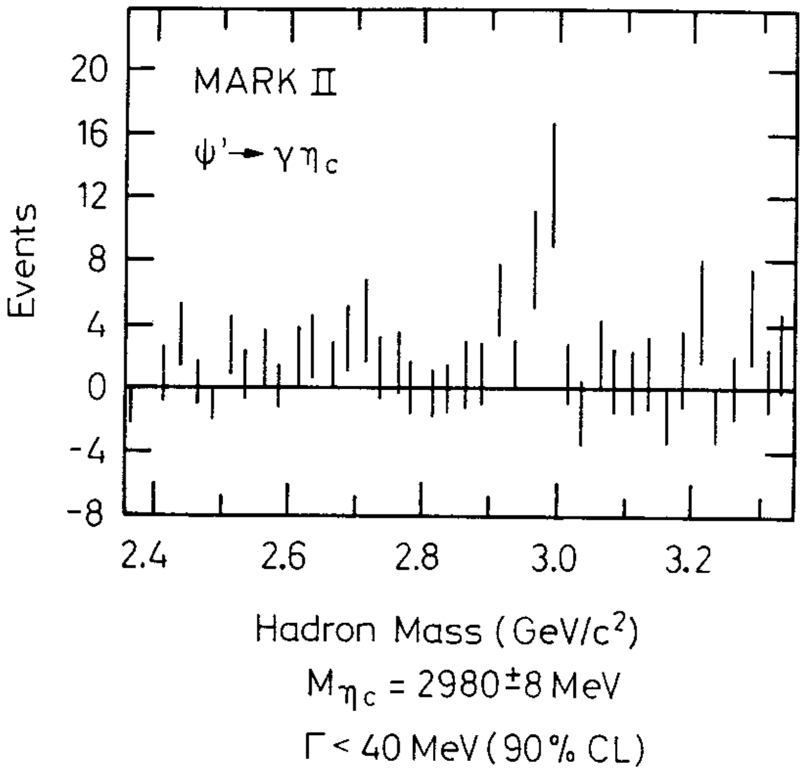

31888

Fig. 2.17 - Hadronic mass spectrum for background subtracted direct-photon event sample from MARK II.

Table 2.4 - Properties of η_c

Mass	2978 ± 9 MeV	Crystal Ball
Total Width	less than 20 MeV	Crystal Ball
Branching ratios		
$B(J/\psi \to \gamma\eta_c)$	∿ 1%	Crystal Ball
$B(\psi' \to \gamma\eta_c)$	$(0.43 \pm 0.08 \pm 0.18)\%$	Crystal Ball
$B(\psi' \to \gamma\eta_c)B(\eta_c \to K^{\pm}K_S\pi^{\mp})$	$(1.5\ ^{+0.8}_{-0.6}) \times 10^{-4}$	MARK II
$B(\psi' \to \gamma\eta_c)B(\eta_c \to \eta\pi^+\pi^-)$	$(3.1 \pm 1.1 \pm 1.5) \times 10^{-4}$	Crystal Ball
$B(\psi' \to \gamma\eta_c)B(\eta_c \to \pi^+\pi^+\pi^-\pi^-)$	$(5.7\ ^{+3.9}_{-2.4}) \times 10^{-5}$	MARK II
$B(\psi' \to \gamma\eta_c)B(\eta_c \to K^+K^-\pi^+\pi^-)$	$(4.0\ ^{+6.0}_{-2.5}) \times 10^{-5}$	MARK II
$B(\psi' \to \gamma\eta_c)B(\eta_c \to p\bar{p})$	$(8\ ^{+8}_{-4}) \times 10^{-6}$	MARK II
$B(\psi' \to \gamma\eta_c)B(\eta_c \to p\bar{p}\pi^+\pi^-)$	$< 5 \times 10^{-5}$ (90% C.L.)	MARK II

3. UPSILON PHYSICS FROM DORIS AND CESR

Five years ago, physics in connection with charm was called "new physics". In this sense, I shall now proceed from new physics to newer physics - physics in connection with the bottom quantum number.

Upsilon physics was born at Fermilab in 1977[3]. By now, four upsilon states are known. By analog with the ψ family, we shall call them $\Upsilon(1s)$, $\Upsilon(2s)$, $\Upsilon(3s)$ and $\Upsilon(4s)$.

3.1 $\Upsilon(1s)$, $\Upsilon(2s)$, and $\Upsilon(3s)$

The first two $\Upsilon(1s)$ and $\Upsilon(2s)$ were confirmed at DORIS two years ago. Since then, the amount of data has increased significantly. The data from DASP[41] are shown in Fig. 3.1. During the first energy scan at CESR in November and December 1979, all three resonances seen at Fermilab were measured. The result from the detector CLEO (which does not stand for anything but goes well with CESR) is shown [42] in Fig. 3.2.

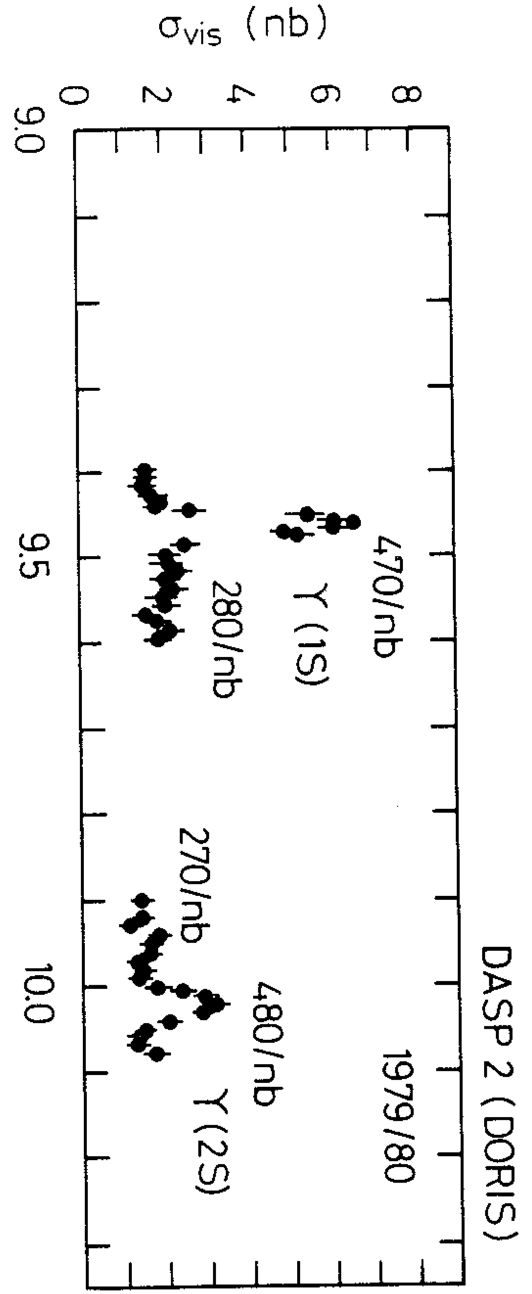

15.12.80

32099

Fig. 3.1 - DASP II cross section for $e^+e^- \to$ hadrons and luminosity for all energies in the $\Upsilon(1S)$ and $\Upsilon(2S)$ region scanned at DORIS.

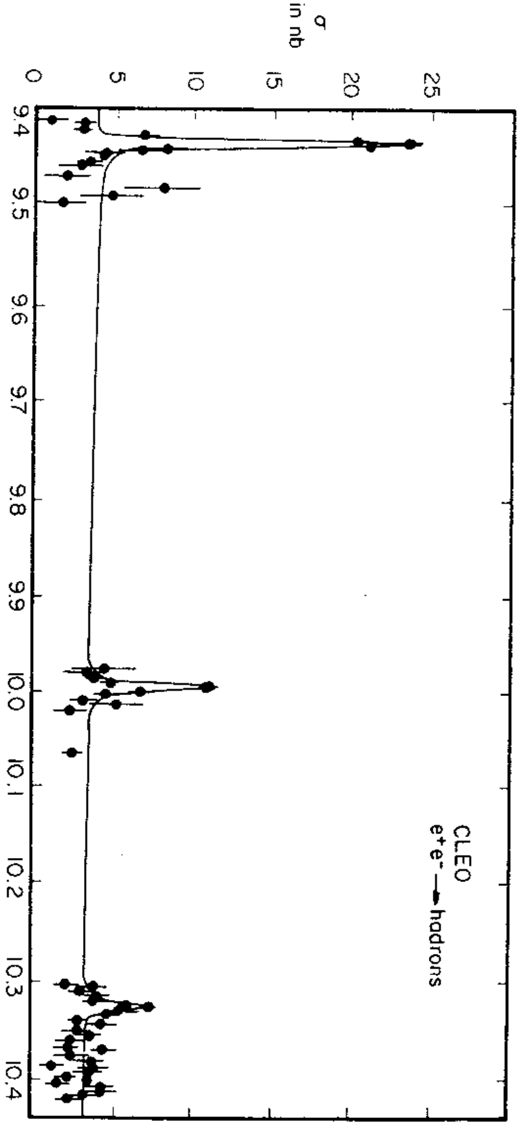

Fig. 3.2 - Total cross section for $e^+e^- \rightarrow$ hadrons in the region of the first three upsilon states, as measured by CLEO.

31905

3.1.1 Masses

The observed masses are shown in Table 3.1 including those from PLUTO, DASP II, and LENA at DORIS and from CLEO and CUSB at CESR. It is immediately noted that the results from DORIS and CESR do not agree, but differ by 20 to 30 MeV. The difference has however no significance, and is due to uncertainty in energy calibration of ± 10 MeV at DORIS and ± 30 MeV at CESR. For this reason, it is useful to refer all masses to that of $\Upsilon(1s)$, as also shown in Table 3.1. The errors in the table are all systematic.

Table 3.1 - Masses of upsilons

		DORIS[41]	CESR[43,44]
Masses	$\Upsilon(1s)$	9462 ± 10	9433 ± 28
Mass differences	$\Upsilon(2s) - \Upsilon(1s)$	553 ± 10	560 ± 3
	$\Upsilon(3s) - \Upsilon(1s)$		889 ± 4
	$\Upsilon(4s) - \Upsilon(1s)$		1114 ± 5

3.1.2 Electronic widths

By integrating the observed cross sections over energy, the partial width Γ_{ee} into e^+e^- is immediately obtained. More precisely, what is obtained is $\Gamma_{ee}\Gamma_h/\Gamma_{tot}$, where Γ_h is the partial width into hadrons, and Γ_{tot} is the total width. The experimental values obtained this way are given in Table 3.2, where the systematic error is as usual written after the statistical error. Their ratios are also tabulated here, because the systematic errors tend to be smaller in the ratio. Since

$$\Gamma_h / \Gamma_{tot} = 1 - 3\, B_{\mu\mu} \qquad (3.1)$$

and $B_{\mu\mu}$ is small (see section 3.1.3 below), the values listed for $\Gamma_{ee}\Gamma_h/\Gamma_{tot}$ are approximately correct also for Γ_{ee}. Somewhat more precisely, Γ_h/Γ_{tot} is about 0.9. In (3.1), the factor 3 comes from the three leptons e, μ, and τ.

There are by now very good reasons to accept these three upsilons $\Upsilon(1s)$, $\Upsilon(2s)$, $\Upsilon(3s)$ as bound states of $b\bar{b}$ where b is the bottom quark of (2.1). Indeed the "s" in the notion means s states for the quarks. The leptonic width clearly should be proportional to the square of the quark charge, which is -1/3 for b. In Fig. 3.3, the ratio Γ_{ee}/e_Q^2 is plotted for various 1^- mesons, and it is found to be remarkably constant.

Table 3.2 Experimental data on the decay widths of the upsilons.

	PLUTO[41]	DASP II[41]	LENA[41]	CLEO[43]	CUSB[44]
$\frac{\Gamma_{ee}\Gamma_h}{\Gamma_{tot}}$ (keV)					
1s	1.33 ± 0.14	1.35 ± 0.11 ± 0.22	1.23 ± 0.10 ± 0.14	0.925 ± 0.06 ± 0.14	
2s		0.61 ± 0.12 ± 0.11	0.55 ± 0.07 ± 0.06	0.468 ± 0.04 ± 0.07	
3s				0.288 ± 0.03 ± 0.05	
4s				0.221 ± 0.02 ± 0.03	
Ratio of $\frac{\Gamma_{ee}\Gamma_h}{\Gamma_{tot}}$					
2s/1s		0.45 ± 0.09 ± 0.05	0.45 ± 0.06 ± 0.02	0.51 ± 0.05 ± 0.05	0.39 ± 0.06
3s/1s				0.31 ± 0.04 ± 0.03	0.32 ± 0.04
4s/1s				0.24 ± 0.02 ± 0.03	0.25 ± 0.07
Branching ratio					
1s→μμ	(2.2 ± 2.0)%	(2.9 ± 1.3 ± 0.5)%	(3.5 ± 1.4 ± 0.4)%		
1s→ee	(5.1 ± 3.0)%				

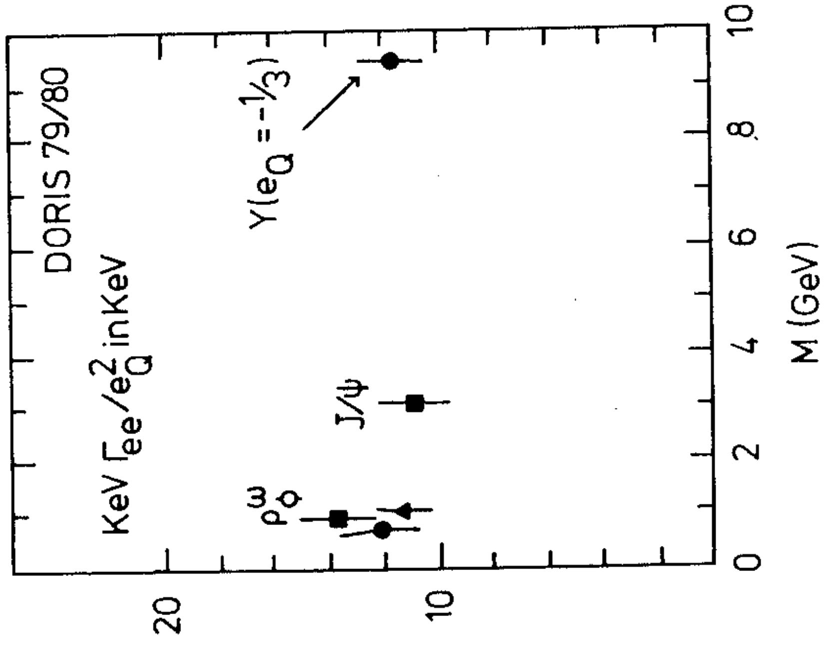

Fig. 3.3 - Ratio of the leptonic width to the quark charge for different vector mesons.

3.1.3 Branching ratio into $\mu^+\mu^-$

While the electronic width can be obtained relatively easily from the experimental data, it is much more difficult to get the total width. For this purpose, it is necessary to know the branching ratio into either e^+e^-, $\mu^+\mu^-$ or $\tau^+\tau^-$. (It is reasonable to assume these branching ratios to be the same). To date, the branching ratio into $\mu^+\mu^-$ has been determined with best accuracy. The results for $\Upsilon(1s)$ are summarized in Table 3.2.

The average of the three determinations at DORIS is

$$B_{\mu\mu} = (2.8 \pm 0.8)\% \qquad (3.2)$$

Using $\Gamma_{tot} = \Gamma_{ee}/B_{\mu\mu}$ and the DORIS values of Γ_{ee}, the total width of $\Upsilon(1s)$ is

$$\Gamma_{tot}(1s) = (43\ ^{+20}_{-11})\,\text{keV} \qquad (3.3)$$

This is to be compared with

$$\Gamma_{tot}(J/\psi) = (67 \pm 12)\ \text{keV} \qquad (3.4)$$

for J/ψ.

3.1.4 Upsilon decay

Unlike the charm families, very little is as yet known about the decay of the upsilons.

A) The PLUTO Collaboration has analyzed various distributions of the $\Upsilon(1s)$ decay. As seen for example from the thrust distribution shown in Fig. 3.4, the data are inconsistent with phase space or two jet decay but consistent with three gluons decay[45,46]. Assuming that the hypothesis of Υ decay into three gluons is correct, the polar angle distribution of the thrust axis with respect to the beam direction can distinguish between scalar and vector gluons. Fig. 3.5 shows that the data favor the distribution $1 + 0.39 \cos^2\theta$ for spin 1 gluons over the $1 - \cos^2\theta$ for spin 0 gluons[46].

B) The decay

$$\Upsilon(2s) \rightarrow \Upsilon(1s) + \pi^+ + \pi^- \qquad (3.5)$$
$$\qquad\qquad\quad \hookrightarrow e^+e^- \text{ or } \mu^+\mu^-$$

has been seen by[42] CLEO (2 events), CUSB (3 events) and LENA (7 events). The branching ratios are given as

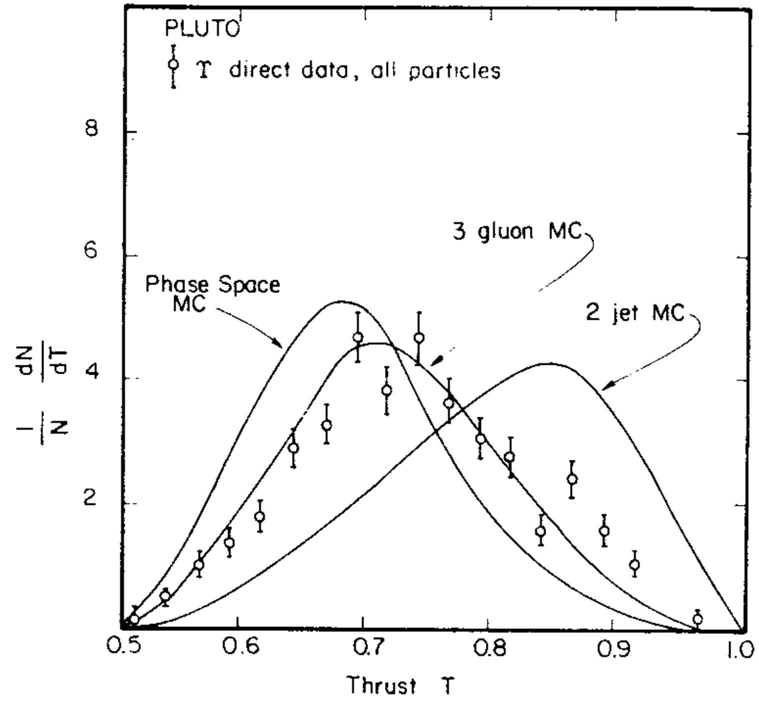

Fig. 3.4 - Thrust distribution of Υ-direct decay events (charge + neutral particles) from PLUTO in comparison to various models.

31893

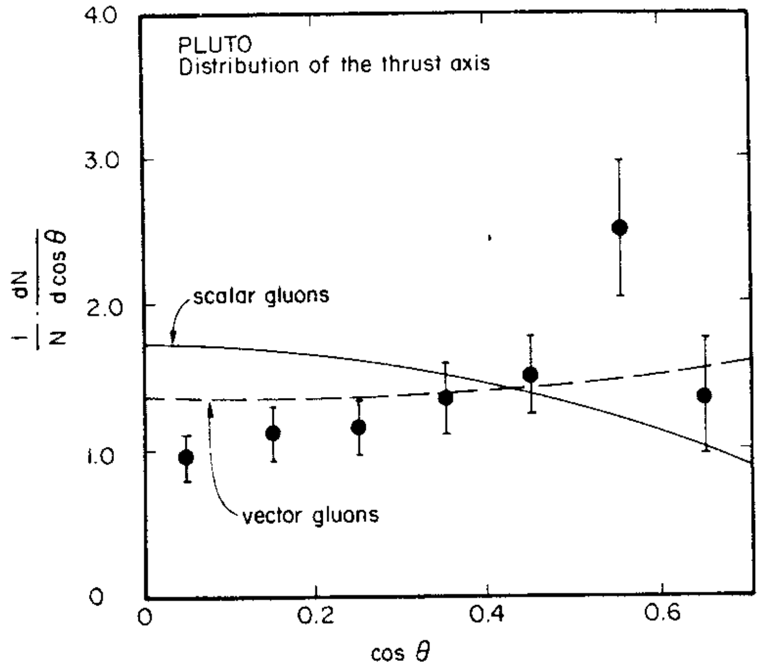

Fig. 3.5 - Distribution of the thrust axis in comparison to predictions of vector and scalar gluons.

31891

LENA	(27 ± 9)%
CLEO	(22 ± 16 ± 11)%
CUSB	(10 to 20)%

This is the first direct evidence that the $\Upsilon(2s)$ and $\Upsilon(1s)$ are closely related.

3.2 $\Upsilon(4s)$

This year a fourth upsilon was discovered at CESR. This new upsilon has rather different properties compared with the previous three states.

3.2.1 Mass

The observations of this new upsilon by CLEO and CUSB are shown in Figs. 3.6 and 3.7 respectively. In order to reduce the continuum background, CUSB carries out a cut in pseudo-thrust T' defined by[44]

$$T' = \max \frac{\Sigma|\vec{E}_{NaI} \cdot \hat{n}|}{\Sigma|\vec{E}_{NaI}|} \qquad (3.6)$$

where the maximum is taken over all unit vectors $\hat{n}$ perpendicular to the beam axis. This result of using a cut $T' < 0.85$ improves the signal to noise ratio. The mass differences between $\Upsilon(4s)$ and $\Upsilon(1s)$ is given in Table 3.1.

3.2.2 Width

It is evident from Figs. 3.6 and 3.7 that $\Upsilon(4s)$ is considerably wider than $\Upsilon(3s)$. The directly observed r.m.s. width in MeV by CLEO are[43]:

1s	3.14 ± 0.20
2s	3.53 ± 0.22
3s	3.76 ± 0.24
4s	9.00 ± 0.82

Here the first three values agree well with the energy spread of the accelerator. Taking this energy spread into account, the full width of $\Upsilon(4s)$ is determined to be

(12.6 ± 6.0) MeV	CUSB[44]
(19.3 ± 5.5 ± 5) MeV	CLEO[43]

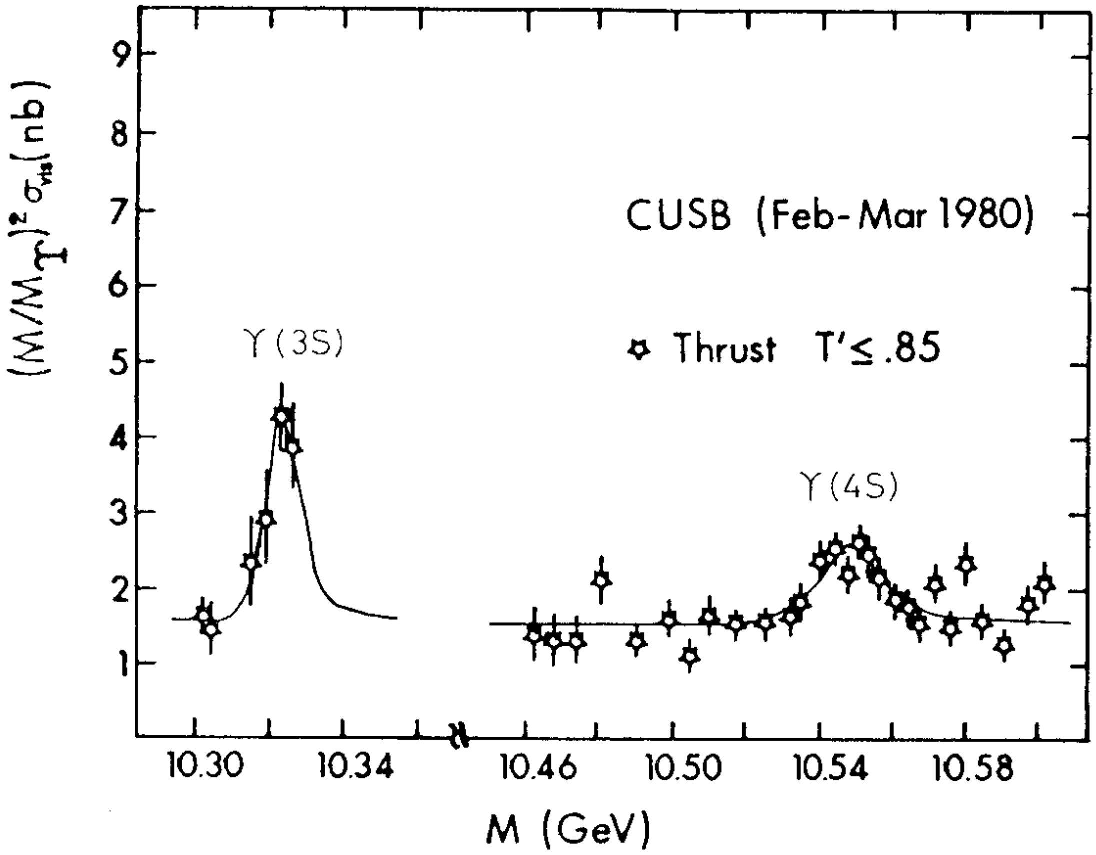

15.12.80

Fig. 3.7 - Observed cross section for $e^+e^- \to$ hadrons from CUSB near $\Upsilon(3S)$ and $\Upsilon(4S)$.

32108

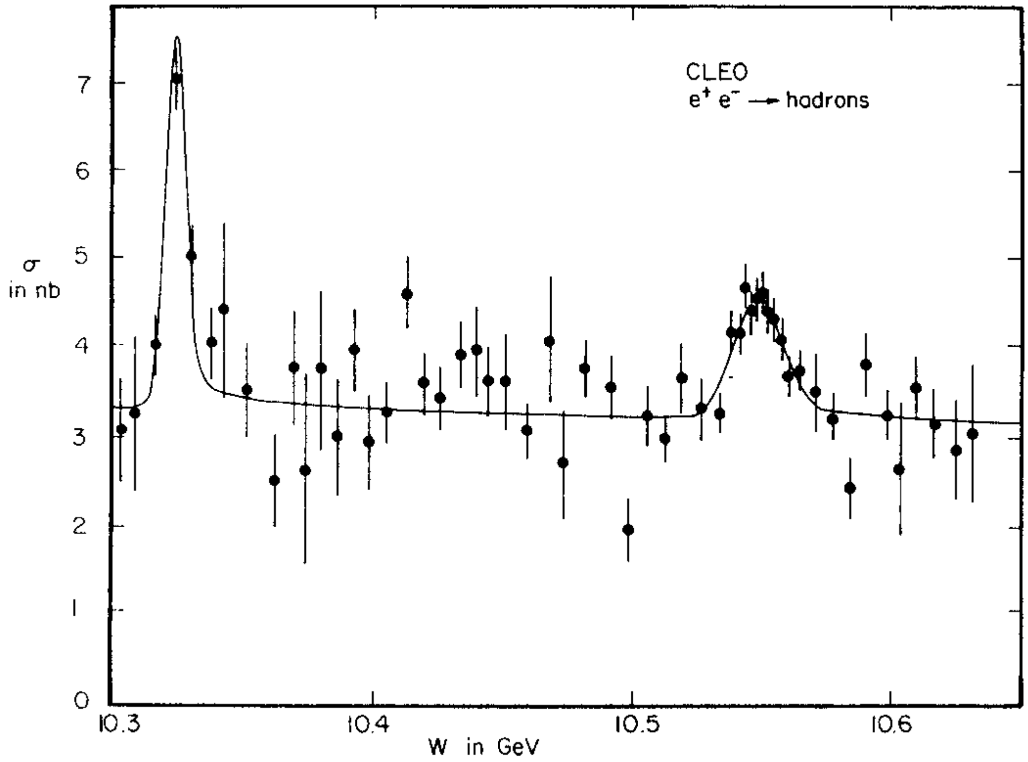

Fig. 3.6 - Total cross section for $e^+e^- \to$ hadrons as a function of center-of-mass energy, showing the third and fourth Υ-resonances

31907

3.2.3 Mass of the bottom meson

The four states are thus characterized by: narrow, narrow, narrow and broad. Even without any theory, something interesting has happened between $\Upsilon(3s)$ and $\Upsilon(4s)$.

By analog with the charm family, what has happened in the decay is likely to be

$$\Upsilon(4s) \rightarrow B\bar{B} \qquad (3.7)$$

where B is a meson with bottom quantum number. Since $\Upsilon(3s) \not\rightarrow B\bar{B}$, the mass of the lightest bottom meson must be between half of the $\Upsilon(3s)$ mass and half of the $\Upsilon(4s)$ mass:

$$5162 \text{ MeV} < M_B < 5274 \text{ MeV} \qquad (3.8)$$

on the CESR energy scale.

The question is raised whether the decay can be $\Upsilon(4s) \rightarrow B\bar{B}^*$ and $\bar{B}B^*$. By looking at the photon spectrum, CUSB has preliminary evidence against this alternative decay mode[42].

Again by analog with the D mesons, we expect theoretically four B mesons:

$B^+(\bar{b}u)$, $B^0(\bar{b}d)$, $\bar{B}^0(b\bar{d})$ and $B^-(b\bar{u})$.

3.2.4 Sphericity distribution

The event shape is different at $\Upsilon(4s)$ from the nearby continuum. Some average values have been measured by CLEO, and are listed[43] in Table 3.3. The difference is quite significant even though the values have not been corrected for detector acceptance.

Table 3.3 - Comparison of event shapes at $\Upsilon(4s)$ and the nearby continuum

	$\Upsilon(4s)$	Continuum between $\Upsilon(3s)$ and $\Upsilon(4s)$
Average charged multiplicity	8.48 ± 0.74	6.55 ± 0.06
Average sphericity	0.38 ± 0.05	0.232 ± 0.005
Average thrust	0.76 ± 0.03	0.848 ± 0.002

A more detailed comparison is given in Fig. 3.8. In this result of CLEO, the sphericity distribution is compared with a Monte Carlo simulation of $B\bar{B}$ production and decay, based on the standard model in which b quark decays via $b \rightarrow c + W^-$. The agreement is good. We shall return to this decay $b \rightarrow c + W^-$ in section 3.2.6.

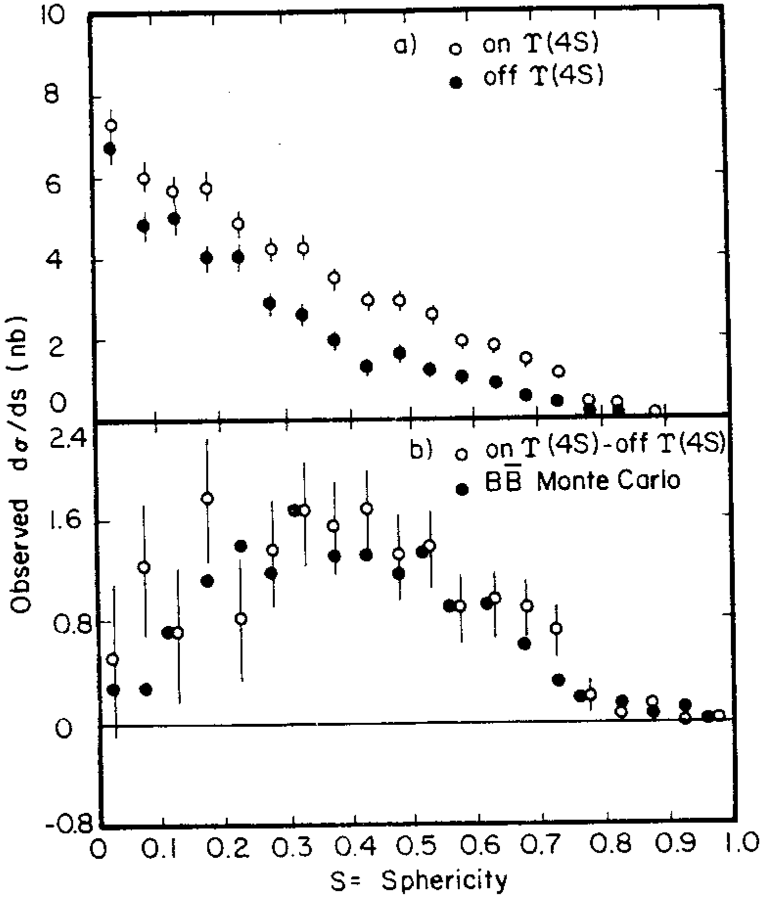

Fig. 3.3 - Observed sphericity distributions measured by CLEO at the $\Upsilon(4S)$ and in the nearby continuum.

31900

3.2.5 Electron and muon yields from B decay

The weak decay of B and $\bar{B}$ must lead to extra yield of leptons. The CUSB[44] comparison of the electron yields at $\Upsilon(3s)$, $\Upsilon(4s)$ and in-between continuum is shown in Fig. 3.9. In both figures, the pseudo-thrust cut $T' < 0.85$ is used to reduce background. This is a clear enhancement in electron yield at $\Upsilon(4s)$.

CLEO has measured both the electron yield and the muon yield, shown in Fig. 3.10 and Fig. 3.11 respectively. The branching ratios are[47,48]

$$
\begin{aligned}
B(B \rightarrow eX) &= (13 \pm 3 \pm 3)\% \\
B(B \rightarrow \mu X) &= (9.4 \pm 3.6)\%
\end{aligned}
\tag{3.9}
$$

If the two branching ratios are belived to be the same, the sum is given as $(22 \pm 6)\%$.

3.2.6 K yields from B decay

Using the information in the central drift chamber and the time-of-flight counters, CLEO determines the K/π ratio[43] as a function of the beam energy, as shown in Fig. 3.12. There is a clear increase in this ratio at the mass of the $\Upsilon(4s)$.

Why is the K yield so interesting ? The reason is that this can be used to determine how the b quark decays. The quark diagrams are shown in detail in Fig. 3.13 where it is seen that the average number of strange quarks (and hence K's) per $B\bar{B}$ event is 10/3 and 4/3 for $b \rightarrow cW^-$ and $b \rightarrow uW^-$ without detailed analysis.

Because of the acceptance and the momentum range where K and π can be separated, a detailed analysis requires a Monte Carlo computation. The results given by CLEO on the number of charged K per event in the accepted momentum interval (0.6 to 1.0 GeV/c) are:[42]

Observed from $B\bar{B}$	$0.40 \pm 0.09 \pm 0.02$
Monte Carlo ($b \rightarrow cW^-$)	0.22 ± 0.05
Monte Carlo ($b \rightarrow uW^-$)	0.06 ± 0.01
Ovserved from continuum	$0.06 \pm 0.01 \pm 0.01$
Monte Carlo (continuum)	0.08 ± 0.02 .

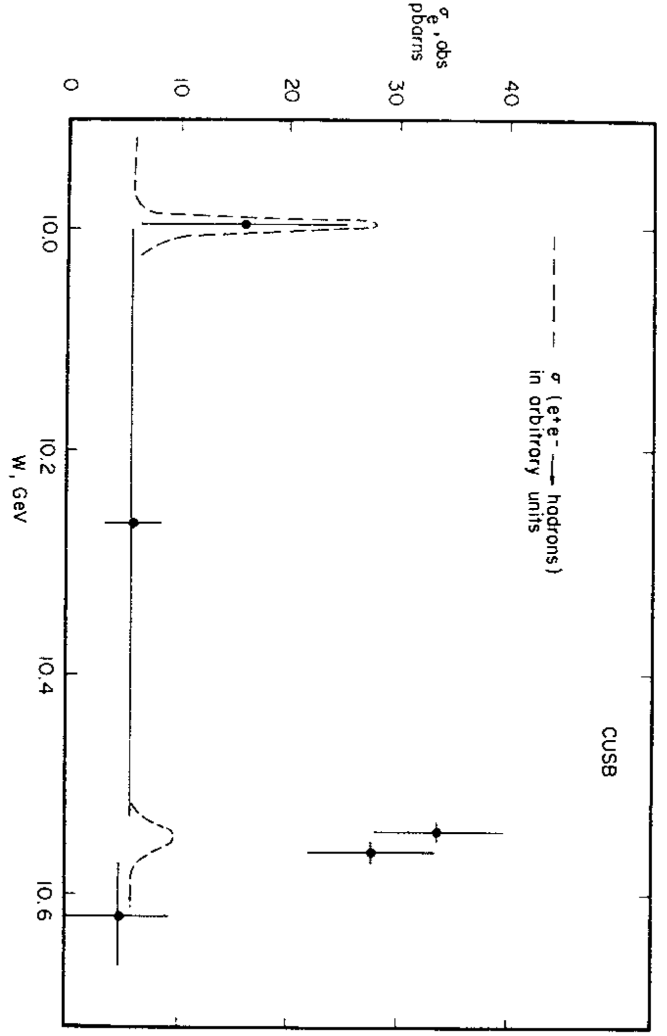

Fig. 3.9 - Observed inclusive electron cross section near the $\Upsilon(3S)$ and $\Upsilon(4S)$ from CUSB. The dashed line shows the behavior of the total hadronic cross section on an arbitrary scale.

31901

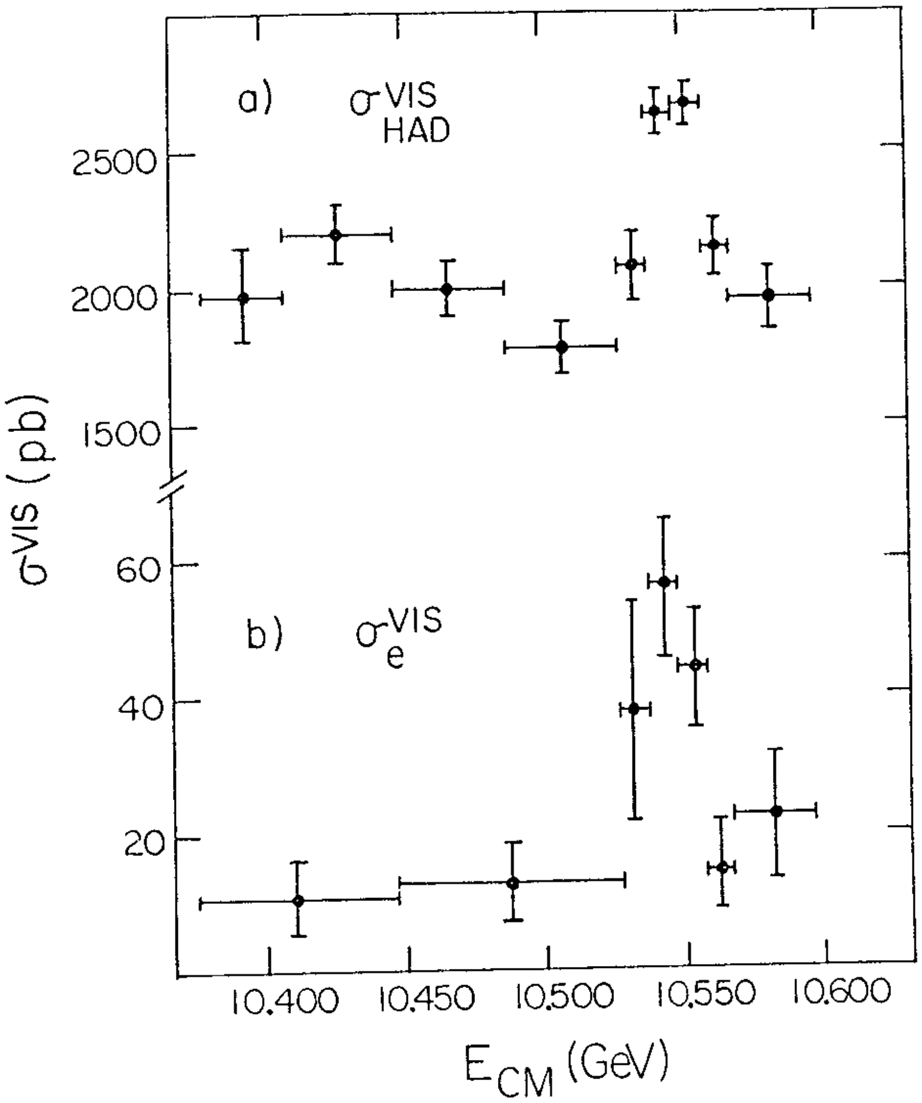

Fig. 3.10 - Visible cross sections for
a) hadronic events and
b) electron yield from hadronic events from CLEO as a function of center-of-mass energy near Υ(4S).

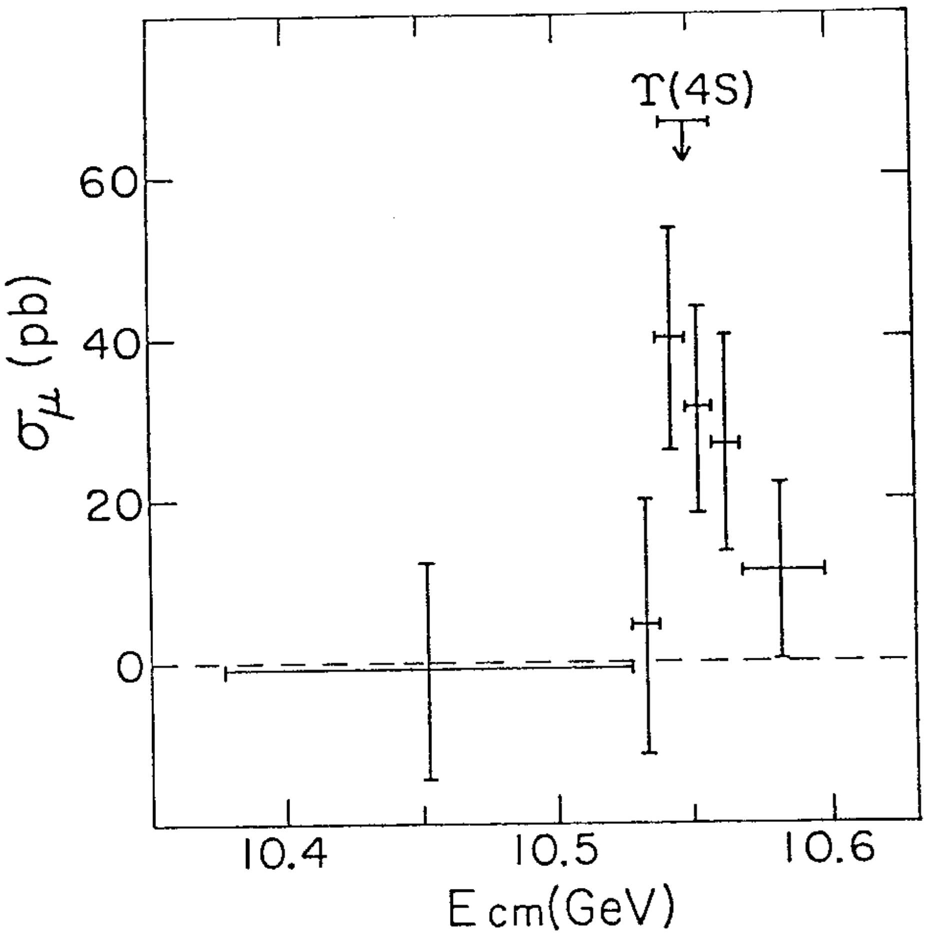

Fig. 3.11 - Muon yield from hadronic events from CLEO as a function of center-of-mass energy near Υ(4S).

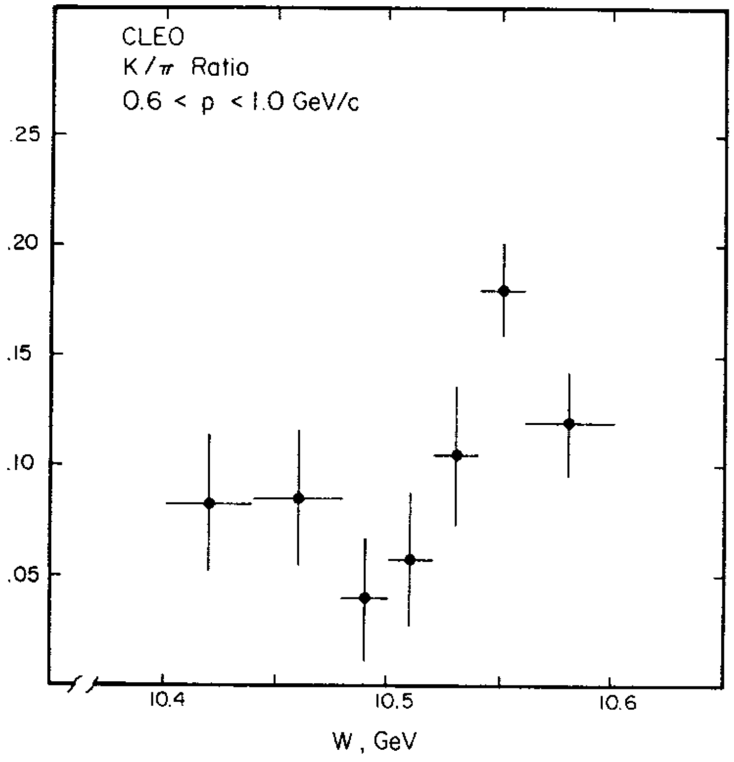

Fig. 3.12 - $K^{\pm}/\pi^{\pm}$ ratio from CLEO as a function of center-of-mass energy near ϒ(4S).

31895

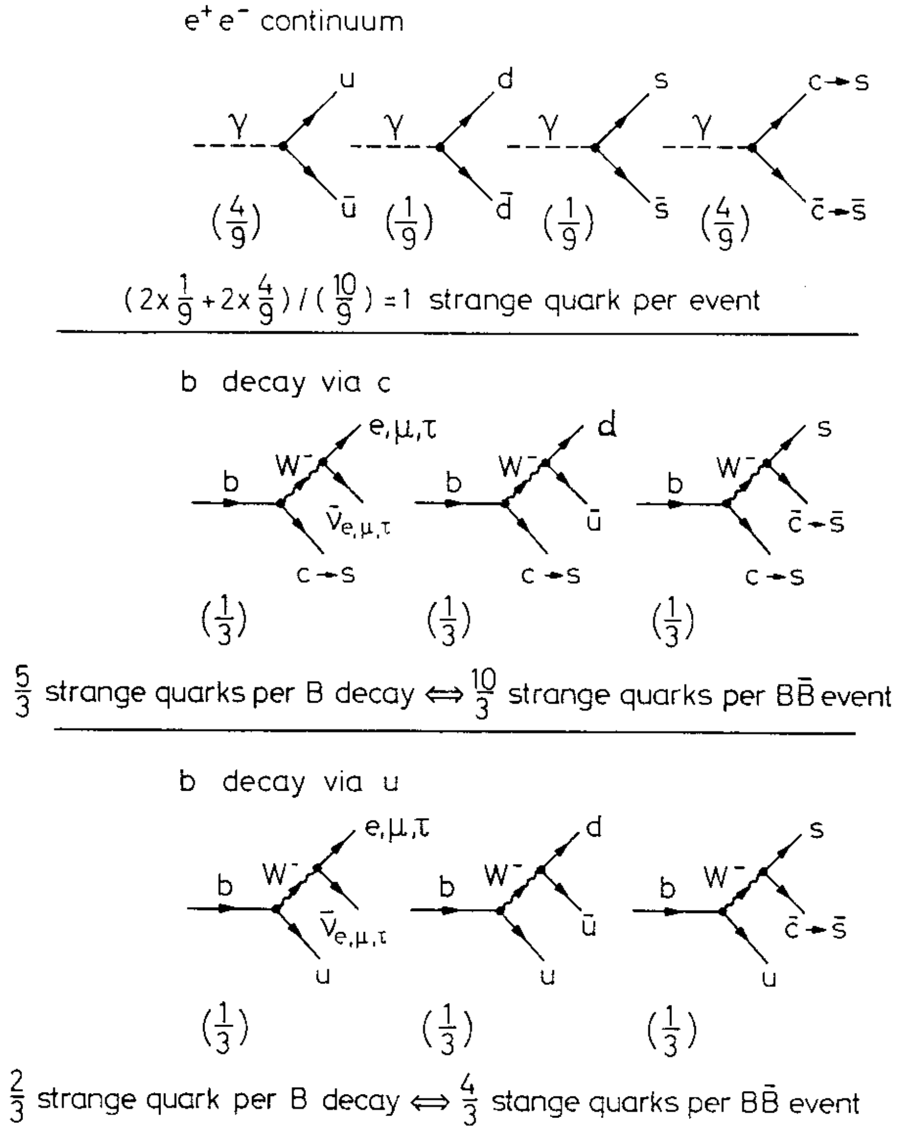

$(2\times\frac{1}{9}+2\times\frac{4}{9})/(\frac{10}{9})=1$ strange quark per event

$\frac{5}{3}$ strange quarks per B decay $\Longleftrightarrow$ $\frac{10}{3}$ strange quarks per $B\bar{B}$ event

$\frac{2}{3}$ strange quark per B decay $\Longleftrightarrow$ $\frac{4}{3}$ stange quarks per $B\bar{B}$ event

Fig. 3.13 - Quark diagrams for the production of strange quarks.

15.12.80

32098

When the favored $b \to cW^-$ Monte Carlo is used to correct for the momentum acceptance, this CLEO measured number translates into an average of

$$2.4 \pm 0.5 \pm 0.5$$

K's per B decay (charged and neutral).

Finally, an upper limit on the B lifetime is reported by CLEO[43] to be 10^{-10} sec.

4. QUARK AND GLUON PHYSICS FROM PLUTO AND TASSO AT PETRA

We have so far discussed charm physics in section 2 and upsilon physics in section 3. Next we go on to e^+e^- physics beyond the upsilons, and discuss some of the recent measurements that bear more directly on the properties of quarks and gluons - the most fundamental constituents of hadrons as of now.

4.1 Long-range charge correlation in opposite jets

In this section, we report the first observation of a long-range charge correlation in opposite jets in e^+e^- by the TASSO Collaboration[49]. We study the two-jet events from the reaction

$$e^+e^- \to q\bar{q} \to \text{two jets.}$$

The rapidity of each charged hadron in a two-jet event is defined as usual by $y = 1/2 \ln \left[(E + p_{\parallel}) / (E - p_{\parallel})\right]$, where $p_{\parallel}$ is the component of the momentum parallel to the jet axis. If n is the charged multiplicity of the event, then we difine a charge correlation function, the compensating charge flow $\bar{\Phi}$ by

$$\bar{\Phi}(y,y') = -\frac{1}{\Delta y \Delta y'} < \frac{1}{n} \sum_{k=1}^{n} \sum_{i \neq k} e_i(y)\, e_k(y') > \qquad (4.1)$$

where, for example, for the ith particle with rapidity y_i, $e_i(y) = +1$ or -1 according to the charge of this particle if y_i is inside an interval Δy around y and $e_i(y) = 0$ otherwise. In (1) < > means averaging over all events.

This charge correlation function is to be compared with the corresponding particle density function defined by

$$\bar{\rho}(y,y') = \frac{1}{\Delta y \Delta y'} < \frac{1}{n(n-1)} \sum_{k=1}^{n} \sum_{i \neq k} |e_i(y)|\, |e_k(y')| > \qquad (4.2)$$

where the sum is over all charged particles. The denominators n and n(n-1) in (4.1) and (4.2) are chosen such that

$$\int dy \int dy'\ \bar{\Phi}(y, y') = \int dy \int dy'\ \bar{\rho}(y, y') = 1 \qquad (4.3)$$

because $\sum_{i \neq k} e_i e_k = -n$ and $\sum_{i \neq k} |e_i||e_k| = n^2 - n.$ (4.4)

Let $P(y_+, y'_-)$, for example, be the probability of having a positively charged particle with rapidity y and a negatively charged particle with rapidity y'. In terms of this probability, $\bar{\rho}$ and $\bar{\Phi}$ are

$$\bar{\rho}(y,y') \propto P(y_+,y'_-) + P(y_-,y'_+) + P(y_+,y'_+) + P(y_-,y'_-) \qquad (4.5)$$

and $\bar{\Phi}(y,y') \propto P(y_+,y'_-) + P(y_-,y'_+) - P(y_+,y'_+) - P(y_-,y'_-)$ (4.6)

For practical purposes, it is more convenient to plot instead

$$\rho(y, y') = \bar{\rho}(y, y') \Big/ \int dy\ \bar{\rho}(y, y') \qquad (4.7)$$

and $\phi(y, y') = \bar{\Phi}(y, y') \Big/ \int dy\ \bar{\Phi}(y, y')$ (4.8)

such that $\int dy\ \rho(y, y') = \int dy\ \phi(y, y') = 1.$ (4.9)

Thus $\rho(y,y')$ is the probability that a charged particle with rapidity y' finds another charged particle with rapidity y, while $\phi(y,y')$ is the probability that the charge of a particle with rapidity y' is compensated by another particle of opposite charge with rapidity y.

Using the TASSO data with the additional cut that the total observed charge is 0 or ±1, $\rho(y,y')$ is plotted in Fig. 4.1 for (a) $-0.75 \leq y' \leq 0$ and (b) $-5 \leq y' \leq -2.5$. Also $\phi(y,y')$ is plotted in Fig. 4.2 for (a) $-0.75 \leq y' \leq 0$ and (b) $-5 \leq y' \leq -2.5$. A comparison of these figures shows the following features.

A) For small values of y', Fig. 4.1(a) shows a broad distribution while Fig. 4.2(a) shows a narrower distribution which peaks at $y \sim y'$. This is the evidence for a short range charge correlation. Moreover as y' becomes larger, there exhibits a peak adjacent to y' as shown in Fig. 4.2(b) but not so in Fig. 4.1(b). This further supports the evidence for short range charge correlation.

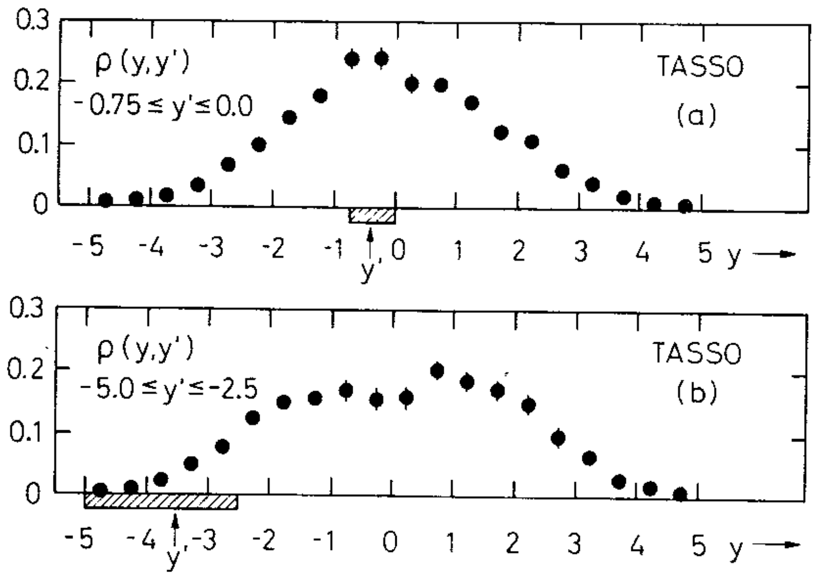

22.9.80

31715

Fig. 4.1 - The particle density function $\rho(y,y')$ as a function of y for (a) $-0.75 \le y' \le 0$ and (b) $-5 \le y' \le -2.5$. Here y and y' are the rapidity variables for charged particles. The data are from center-of-mass energies of 27 to 36 GeV.

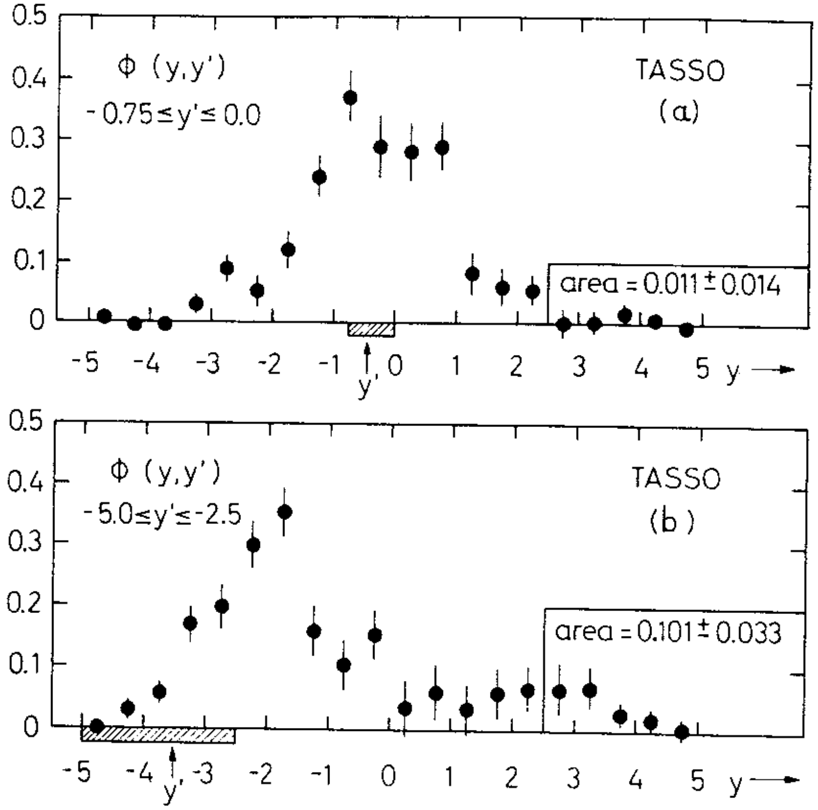

22.9.80

31716

Fig. 4.2 - The charge correlation function (y,y') as a function of y for (a) $-0.75 \le y' \le 0$ and (b) $-5 \le y' \le -2.5$. Here y and y' are the rapidity variables for charged particles. The data are from center-of-mass energies of 27 to 36 GeV.

B) As shown in Fig. 4.2(b), there is a noticeable rise in the ϕ distribution near large positive y when y' is large and negative. The area beyond $y \gtrsim 2.5$ is 0.101 ± 0.033 from Fig. 4.2(b) compared with the corresponding value of 0.011 ± 0.014 from Fig. 4.2(a) for small y'. This is the evidence of a long-range charge correlation in opposite jets from e^+e^- annihilation.

The result of long range correlation may be qualitatively understood as follows. With the schematic diagram of hadron production of Fig. 4.3 let the produced charged hadrons be ordered as shown there. Since the quark charges are $\pm 1/3$ and $\pm 2/3$, we have with this ordering $e_1 = 1$, $e_2 = -1$, $e_3 = 1$, $e_4 = -1$ etc. Although this ordering cannot be determined experimentally, it is strongly correlated with the rapidity ordering. Accordingly, the presence of a negative charge for large negative y increases the probability of the presence of a positive charge for large positive y', and vice versa. Thus our observation of a long range charge correlation in opposite jets gives independent corroboration of the picture of jet formation via a $q\bar{q}$ pair as shown in Fig. 4.3.

4.2 Two-photon physics

By two-photon physics, we mean the study of processes of the type

$$e^+e^- \rightarrow e^+e^- + \text{hadrons} \qquad (4.10)$$

The idea is that the positron and the electron each emit a photon, and the two photons interact to produce the hadrons. Such a process is shown diagrammatically in Fig. 4.4.

4.2.1 Significance

There are at least three independent reasons why two-photon physics is important

A) At high energies the total cross section for the process (4.10) is large. This is because of the possible smallness of Q_1^2 and Q_2^2 (in Fig. 4.4) which both appear in the denominator of the matrix element.

B) The charge-conjugation quantum number for a two-photon state is +1, and hence the hadrons can be a C = +1 resonance such as f^0. Because of this charge conjugation quantum number, such resonances do not appear directly in one-photon annihilation of e^+ and e^-. This is discussed in section 4.2.3.

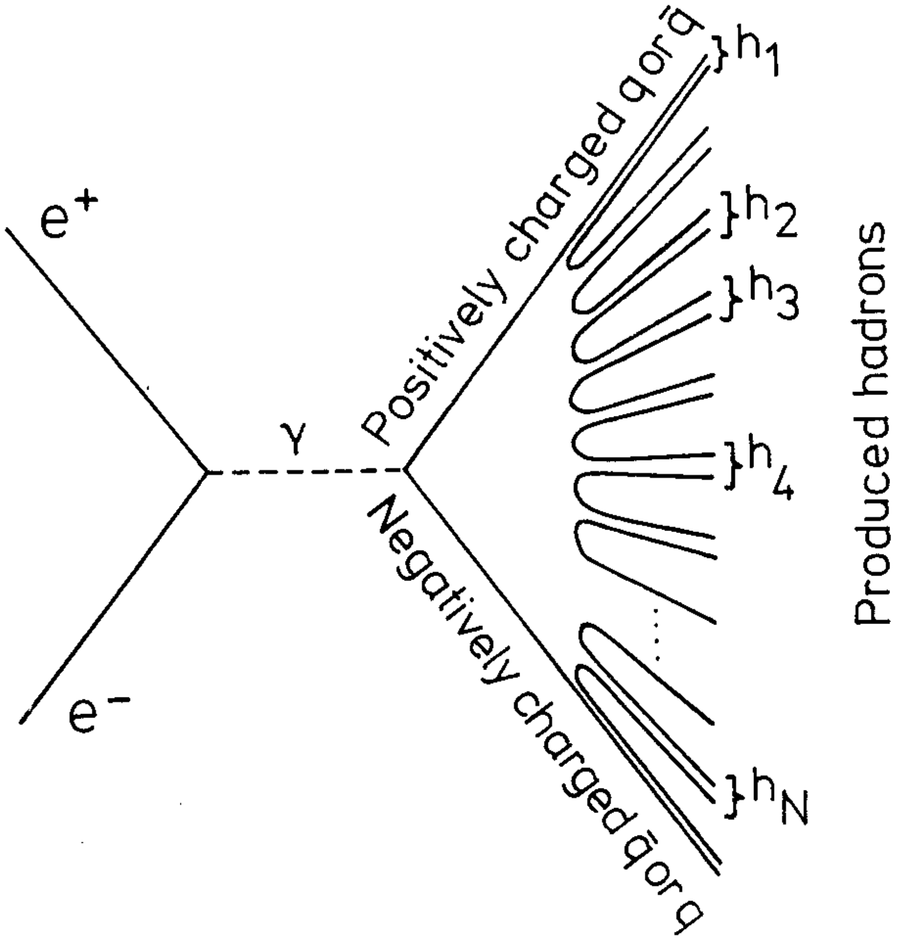

Fig. 4.3 - A schematic diagram of hadron production in e^+e^- annihilation.

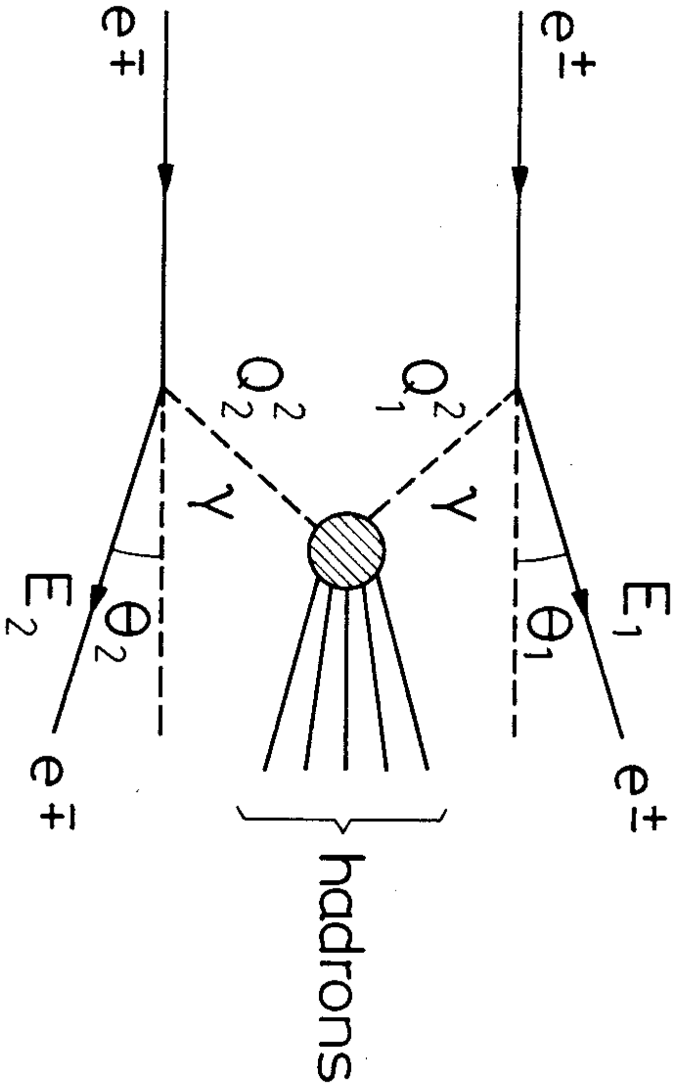

Fig. 4.4 - Diagram for $e^+e^- \to e^+e^-$ + hadrons.

C) Just as $e^+e^- \to q\bar{q}$ is similar to $e^+e^- \to \mu^+\mu^-$, the pair-creation process $\gamma\gamma \to q\bar{q}$ is entirely similar to $\gamma\gamma \to \mu^+\mu^-$, as shown in Fig. 4.5.

On the basis of this very simple quark picture, contrary to proton antiproton annihilation for example, high P_T jets are expected to occur with high probability. This may seem starting at first sight and is to be discussed in section 4.2.6 below.

4.2.2 Kinematics and terminology

With reference to Fig. 4.4 it is seen that

$$|Q_1^2| = -(E-E_1)^2 + \left[(E^2-m^2)^{1/2} - (E_1^2-m^2)^{1/2}\cos\theta_1\right]^2 + (E_1^2-m^2)\sin^2\theta_1 \qquad (4.11)$$

where E and E_1 are respectively the energy of the incoming and outgoing $e^\pm$ and m is the electron mass. Because of the smallvalueof the electron mass, for small θ_1 $|Q_1^2|$ is given accurately by

$$|Q_1|^2 = EE_1\theta_1^2 + m^2\,(E-E_1)^2 / (EE_1). \qquad (4.12)$$

In this formula, the first term and the second term are equal when

$$\theta_1 = \theta_0 = \frac{m(E - E_1)}{E\,E_1} \qquad (4.13)$$

If E is 15 GeV, then this θ_0 is about 0.5 mr even for a very low value of E_1 = 1 GeV. Therefore, for θ_1 much above 1 mr, the effect of the electron mass is negligible. This discussion of course holds for Q_2^2 as well. Also the center-of-mass energy W for the two photon system (and hence also for the hadrons) is given approximately by

$$W = 2\sqrt{(E-E_1)\,(E-E_2)} \qquad (4.14)$$

when m, θ_1, and θ_2 are neglected.

For the discussion of the two-photon physics, we shall use the following terminology. By a single-tagged event, we mean that the electron or the positron is observed in the forward detector. By an untagged or no-tag event, we mean that neither the electron nor the positron is detected in the forward detector.

The forward detector covers an angular range of typically a few degrees. For TASSO, the angular range is from 24 to 60 mr. For PLUTO, there are two forward detectors in each direction, a small angle tagging detector between 23 and 70 mr and a large angle one between 70 mr and 260 mr. Because of the logarithmic dependence of the event rate on the angle, the rates of single-

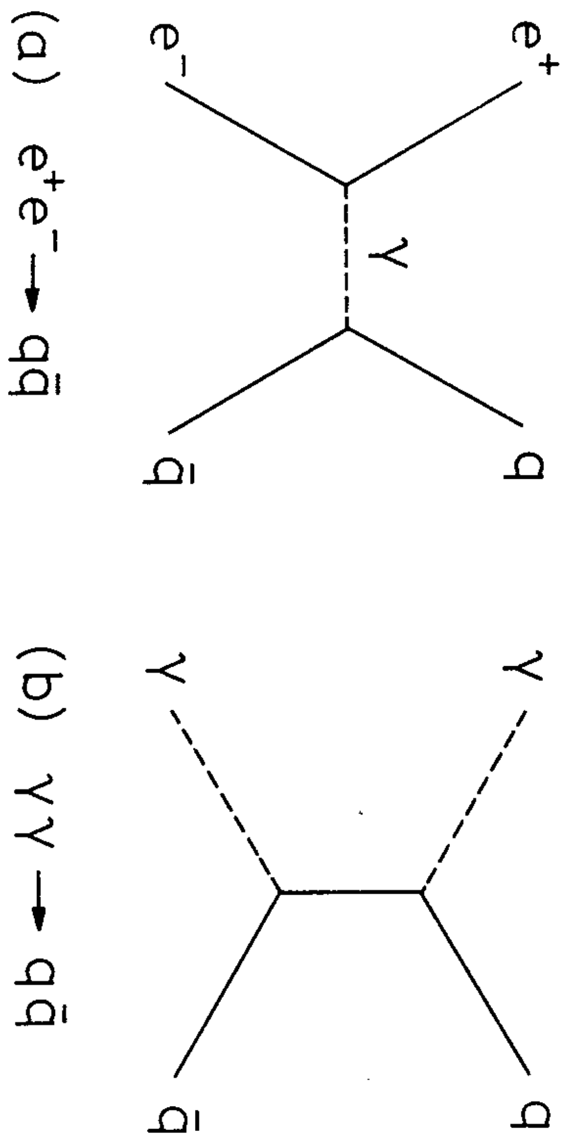

Fig. 4.5 - Diagrams for the creation of a $q\bar{q}$ pair.

tagged events are about the same for the small angle tagging detector and the large angle tagging detector. For a single-tagged event, θ_1 is in the range of a few degrees while θ_2 is small. In other words, $|Q_2^2|$ is small but $|Q_1^2|$ is not so small. As an example, for E = 15 GeV, $E_1 = E_2 =$ 7 GeV, θ_1 = 40 mr and θ_2 = 0, then by (4.12)

$$|Q_1^2| \;=\; 0.17\ \text{GeV}^2 \quad \text{and} \quad |Q_2^2| \;=\; 0.16\ \text{MeV}^2$$

Similarly, for most of the untagged events, both θ_1 and θ_2 are small, and hence both $|Q_1^2|$ and $|Q_2^2|$ are small. Needless to say, the rate for untagged events is much higher than the single-tagged events, but the single-tagged events are much better identified as due to the two-photon process (4.10)

4.2.3 $\gamma\gamma \rightarrow C = +1$ resonance

The process

$$e^+e^- \rightarrow e^+e^- + 2 \text{ prongs}$$

has been investigated by both PLUTO and TASSO under the no-tag condition by observing two oppositely charged tracks that are non-colinear but coplanar with the beam direction. The PLUTO result is shown in Fig. 4.6, while the TASSO result is shown in Fig. 4.7. In both Fig. 4.6 and Fig. 4.7 the number of events is given as a function of the invariant mass M of the two observed charged tracks, both assumed to be pions. The data are to be compared with the absolute QED predictions for the processes

$$e^+e^- \rightarrow e^+e^-\,e^+e^-$$

and

$$e^+e^- \rightarrow e^+e^-\,\mu^+\mu^- \quad .$$

The diagrams taken into account in this QED calculation include not only those due to the two-photon process, and are shown in Fig. 4.8. The contribution from the process

$$e^+e^- \rightarrow e^+e^-\,\pi^+\pi^-$$

is estimated to be roughly about 15%. The theoretical results are shown as the solid curves in Fig. 4.6 and Fig. 4.7(a) and are seen to be in good agreement with the experimental data for both M < 1 GeV and M > 1.5 GeV. There is however a significant excess of events between 1 and 1.5 GeV. This excess is shown in the insert of Fig. 4.6 for the PLUTO result and in Fig. 4.7(b) for the TASSO result.

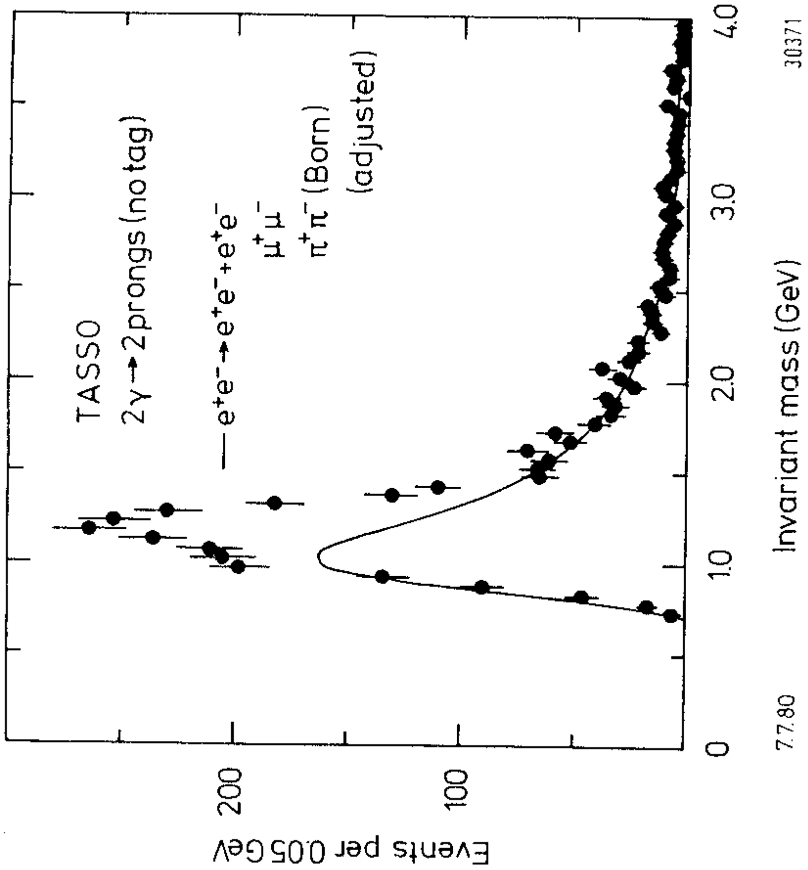

Fig. 4.7(a) - Invariant mass distribution of the two prong events from TASSO. The solid curve is an absolute QED prediction.

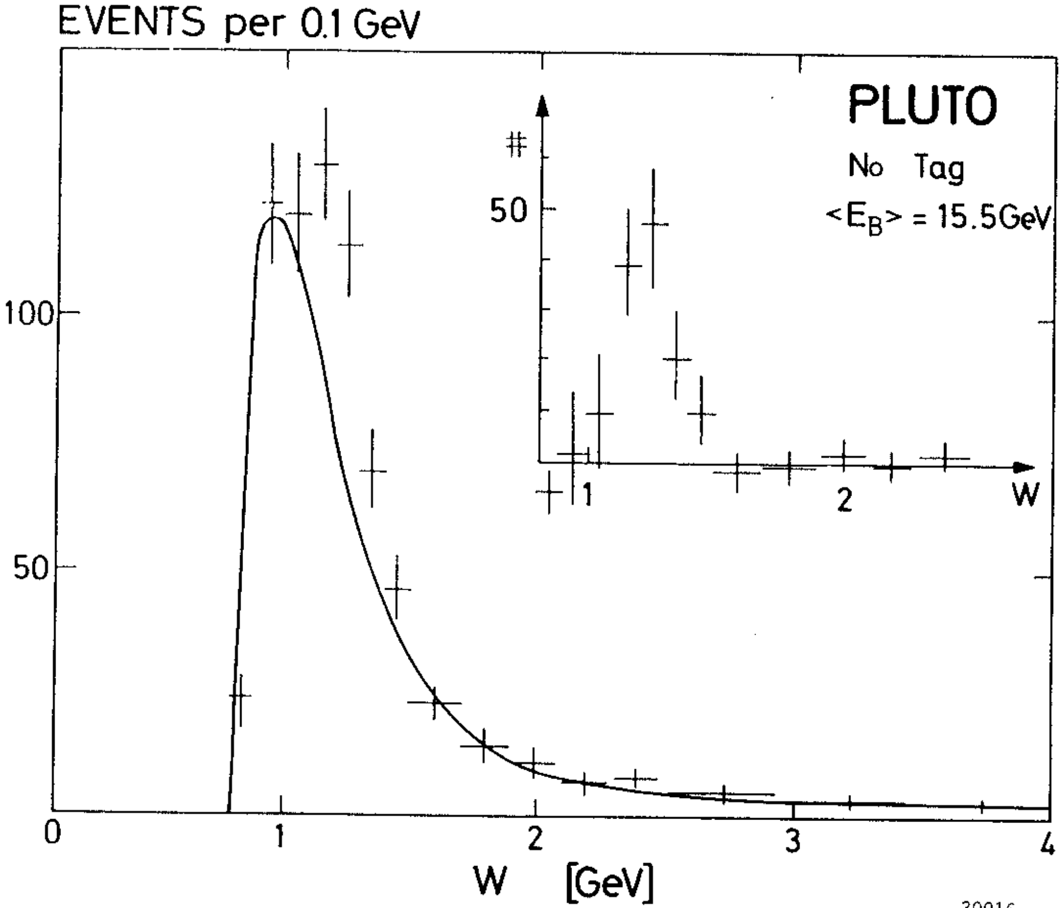

Fig. 4.6 - Invariant mass distribution of the two prong events from PLUTO. The solid curve is an absolute QED prediction. The insert show the difference between data and QED background.

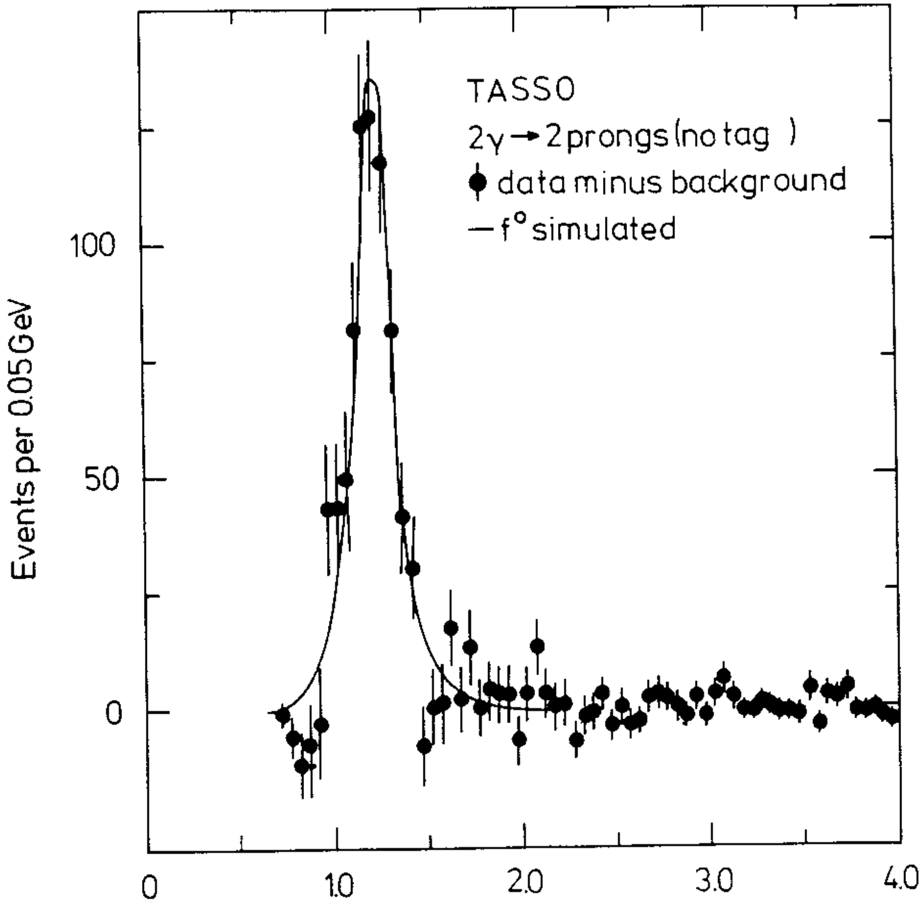

7.7.80 30372

Fig. 4.7(b) - Invariant mass distribution of the two prong events from TASSO with QED background subtracted.

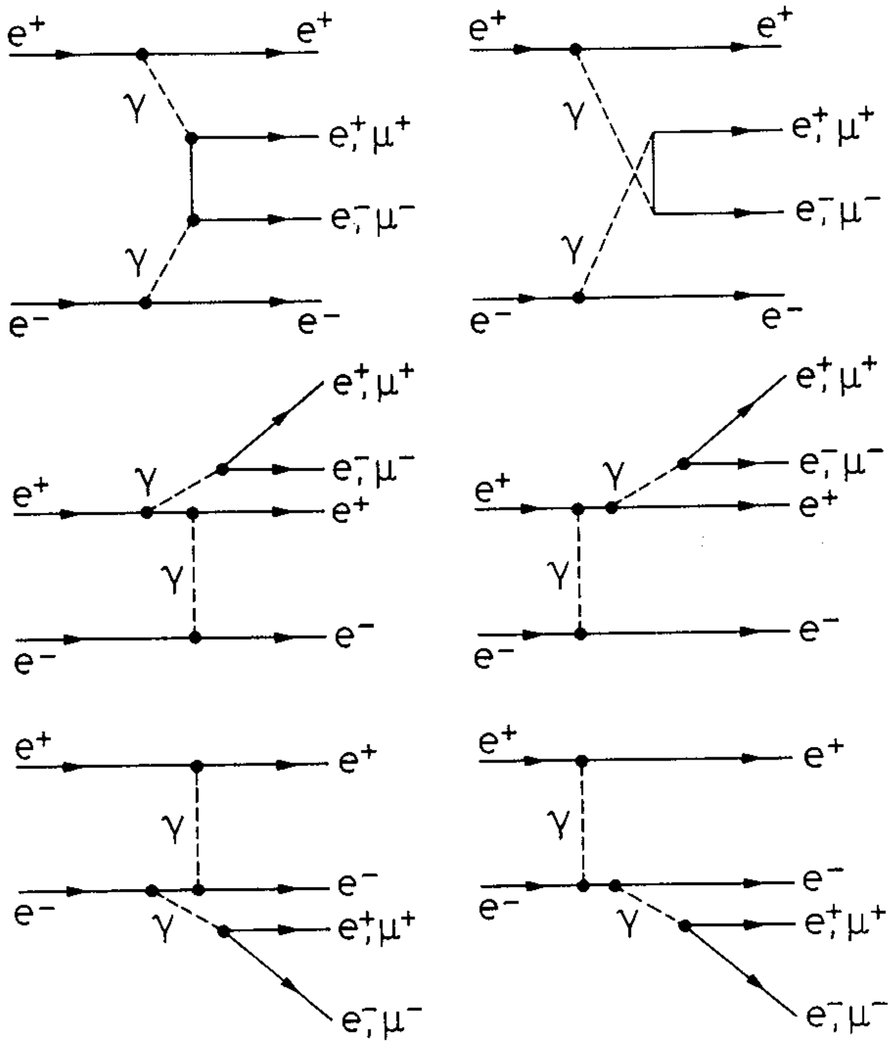

15.12.80 32102

Fig. 4.8 - Feynman diagrams for $e^+e^- \to e^+e^-e^+e^-$ and $e^+e^- \to e^+e^- \mu^+\mu^-$

What can this peak be ? The only candidates are $f^0(1270)$ and $\varepsilon^0(1300)$. Both of these resonances have C = +1 and natural spin-parity, and decay into $\pi^+\pi^-$. Since however $\varepsilon^0(1300)$ has a larger width of 200 - 400 MeV, its contribution must be small. Therefore these events are interpreted as due to the two-photon process (4.10) with

$$\gamma\gamma \rightarrow f^0(1270)$$

From the events, the partial width for

$$f^0(1270) \rightarrow \gamma\gamma$$

can be calculated. The result is, assuming that the helicity amplitude $\lambda = 1$,

$$\begin{aligned} \Gamma^{f^0}_{\gamma\gamma} &= (2.3 \pm 0.5 \pm 0.35)\ \text{keV} \quad \text{from PLUTO}^{50}\ \text{data} \\ \Gamma^{f^0}_{\gamma\gamma} &= (4.1 \pm 0.4 \pm 0.6)\ \text{keV} \quad \text{from TASSO}^{51}\ \text{data} \end{aligned} \tag{4.15}$$

where as usual the first error is statistical error and the second one is systematic error.

4.2.4 $\gamma\gamma$ total cross section

Ten years ago, when vector-meson dominance[52] was more generally accepted, the process

$$\gamma\gamma \rightarrow \text{hadrons} \tag{4.16}$$

was believed to proceed via the diagram of Fig. 4.9, where each photon was first turned into a vector meson, either ρ, ω, or ϕ at relatively low energies. We know now that this cannot be the whole story. As already mentioned in section 4.2.1 (C), (4.16) is also expected to proceed via the formation of two quark jets as shown in Fig. 4.5(b).

Through unitarity the total cross section for (4.16) is given by the imaginary part of $\gamma\gamma \rightarrow \gamma\gamma$ forward scattering, with electromagnetic effects due to electron and muon loops subtracted. Thus the diagram of Fig. 4.9 leads to those of Fig. 4.10(a), where either a pomeron p or some other Regge pole R is exchanged between the vector mesons. Similarly, the diagram of Fig. 4.5(b) leads to the quark diagrams of Fig. 4.10(b), where a third diagram with no imaginary part in the forward direction has been omitted. In order to determine the importance of the quark diagrams in the $\gamma\gamma$ total cross sections, the JADE, PLUTO, and TASSO Collaborations have measured this total cross section and compared with the expectations of vector-meson dominance. In vector-meson dominance, the cross section for two real photons can be estimated using Pomeron factorization

---

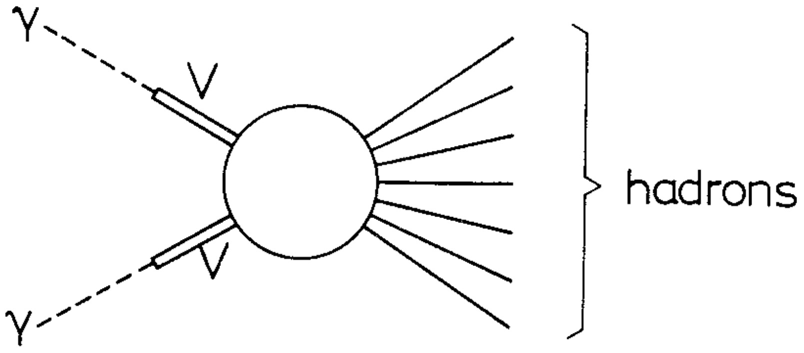

Fig. 4.9 - Vector-meson dominance diagram for $\gamma\gamma \rightarrow$ hadrons.

15.12.80

32101

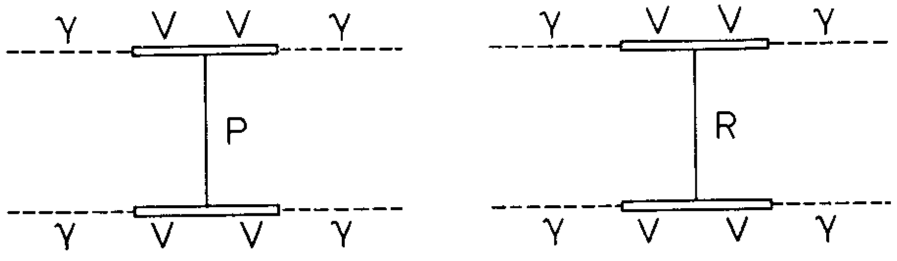

(a) Vector-dominance diagrams

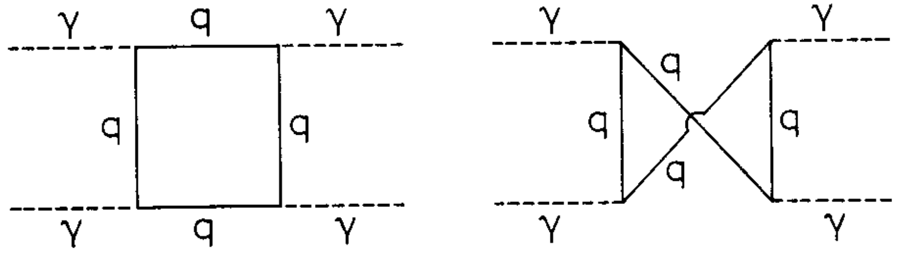

(b) Quark diagrams

15.12.80

32100

Fig. 4.10 - Diagrams for the total cross section $\gamma\gamma \to$ hadrons.

$\sigma_{\gamma\gamma} \cdot \sigma_{pp} = (\sigma_{\gamma p})^2$ and Regge exchange to be

$$\sigma_{\gamma\gamma}\ (W) = \sigma^{VMD}\ (W) = 240 \text{ nb} + \frac{270 \text{ nb} \cdot \text{GeV}}{W} \qquad (4.17)$$

Since the untagged events clearly cannot be used for the measurement of this total cross section, the single-tagged events are analyzed for this purpose. As shown in the example of section 4.2.2, the Q^2 for the photon from the tagged electron or positron is not negligible compared with mass squared of the vector meson even for the small-angle tagging of PLUTO. Extrapolation to $Q^2 = 0$ is therefore necessary. An extrapolation using a ρ pole form factor

$$\sigma_t\ (W,\ Q^2) = \sigma_{\gamma\gamma}(W)\ \left(\frac{m_\rho^2}{m_\rho^2 + Q^2} \right)^2$$

were made to the results of PLUTO and TASSO. Fig. 4.11 shows the results of $\sigma_{\gamma\gamma}(W)$ as a function of W. Both sets of data are seen to be larger than the expectations of the vector-domenance model (σ^{VDM}). The PLUTO[53] data are fitted to a form:

$$\sigma_{\gamma\gamma}(W) = A\, \sigma^{VMD}(W) + \frac{B}{W^2}$$

$$= A(240 \text{ nb} + \frac{270 \text{ nb GeV}}{W}) + \frac{B}{W^2}$$

where $A = 0.97 \pm 0.16$ and $B = 2250 \pm 500$ nb GeV^2. The term $1/W^2$ is expected from pointlike contribution (quark diagrams of Fig. 4.10(b)). The TASSO[51] data are fitted by

$$\sigma_{\gamma\gamma} = 380 \text{ nb} + \frac{520 \text{ nb GeV}}{W}$$

The statistical errors for both PLUTO and TASSO data are indicated by the hatched bands in Fig. 4.11 and in addition, there is a ±25% systematic error. The two results clearly differ in shapes.

4.2.5 $\gamma\gamma \to \rho^o\rho^o$

Since the result shown in Fig. 4.11 indicates the possible inadequacy of vector domenance model and hence importance of the quark diagrams of Fig.4.10(b) the TASSO Collaboration[54] has taken the next step of studying the process $\gamma\gamma \to \rho^o\rho^o$. According to the vector-dominance model, this process proceeds via the diagram of Fig. 4.12.

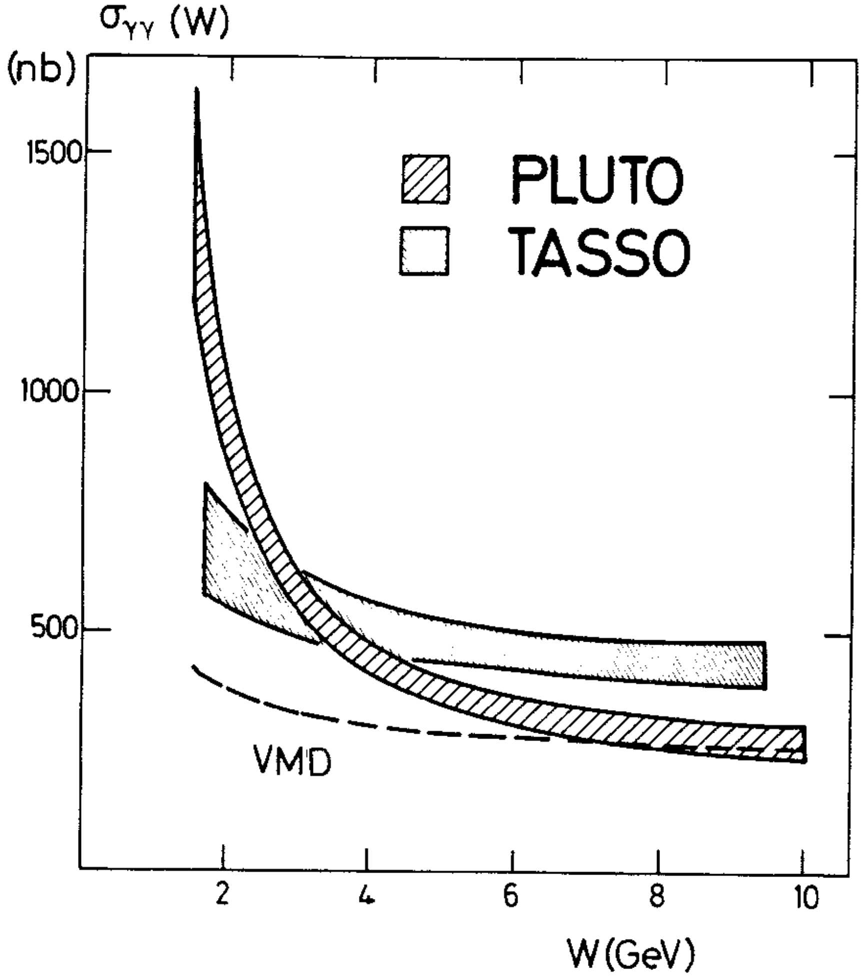

Fig. 4.11 - The total cross section for $\gamma\gamma \to$ hadrons plotted versus the mass of the produced hadron system. The hatched bands indicate the statistical errors only.

31710

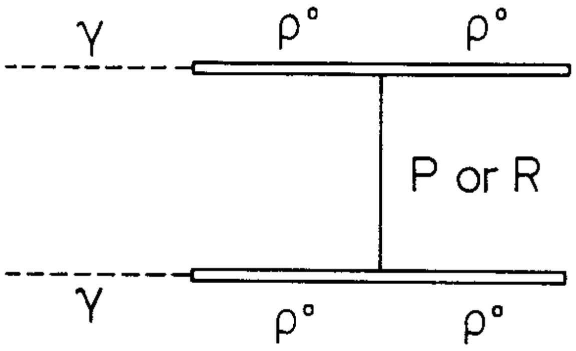

32101

Fig. 4.12 - Vector-dominance diagram for $\gamma\gamma \to \rho^o\rho^o$

Since each ρ^0 decays into a $\pi^+\pi^-$ pair, experimentally we observe

$$e^+e^- \rightarrow e^+e^- \pi^+\pi^+\pi^-\pi^- \quad . \qquad (4.18)$$

It is therefore possible to use the untagged events, and furthermore no extrapolation to $Q^2 = 0$ is needed. Events for (4.18) are identified by two positive and two negative tracks such that

$$|\sum_{j=1}^{4} \vec{p}_{jT}| < 0.15 \text{ GeV/c},$$

whre $\vec{p}_{jT}$ is the transverse momentum with respect to the beam axis. In the range $1.5 < W < 2.3$ GeV, 89 events are found that satisfy this cut. The TASSO result is shown in Fig. 4.13, where it is seen that for $W < 2$ GeV, the cross section for $\gamma\gamma \rightarrow \rho^o\rho^o$ peaks strongly near threshold and drops rapidly with energy and is very much larger than that expected from the vector-meson dominance model.

4.2.6 High p_T jets

In view of the results of the last two sections, it is interesting to study processes that may be attributed to the diagram of Fig. 4.5(b). Since the quark and the antiquark are expected to hadronize into jets, a good candidate is

$$e^+e^- \rightarrow e^+e^- + \text{two jets} \qquad (4.19)$$

Two such singletagged events are shown in Figs.4.14 and 4.15 from PLUTO and TASSO respectively. The jets are not colinear but are coplanar with the beam direction.

Since the scattering angles Θ_1 and Θ_2 for $e^\pm$ are at most several degrees, the transverse momenta p_T of the two jets with respect to the beam axis are nearly equal. In Fig.4.16 the PLUTO data, including both the untagged and single-tagged events, are given as a function of p_T^2. Two distinct slopes are clearly seen, for $p_T^2 \lesssim 1(\text{GeV/c})^2$, the data fit well with $e^{-5p_T^2}$, in agreement with the vector dominance model. For high p_T^2, the slope is consistent with $1/p_T^4$ as expected from hard component. Since the untagged events may be contaminated with processes without e^+e^- in the final state, the TASSO Collaboration uses only single-tagged data shown in Fig. 4.17. Again the data show an exponential fall of with a slope of -5 $(\text{GeV/c})^2$ for $p_T^2 < 0.8(\text{GeV/c})^2$ but show significant excess for $p_T^2 > 0.8$ $(\text{GeV/c})^2$. Thus both the PLUTO and the TASSO results

---

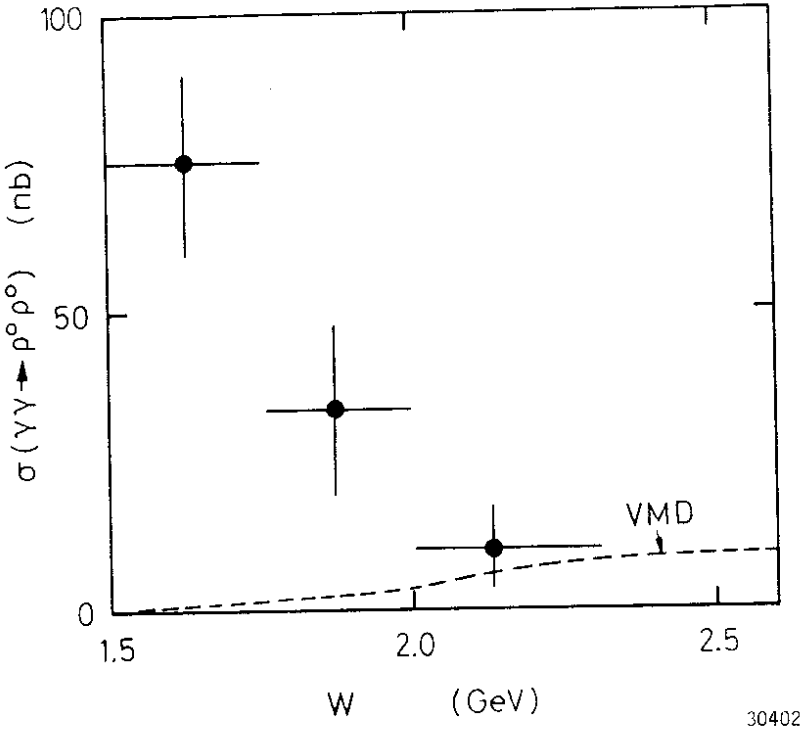

Fig. 4.13 - Cross section for $e^+e^- \rightarrow e^+e^- \rho^o\rho^o$ as measured by TASSO. An asymptotic VMD prediction is shown as the dotted line.

30037

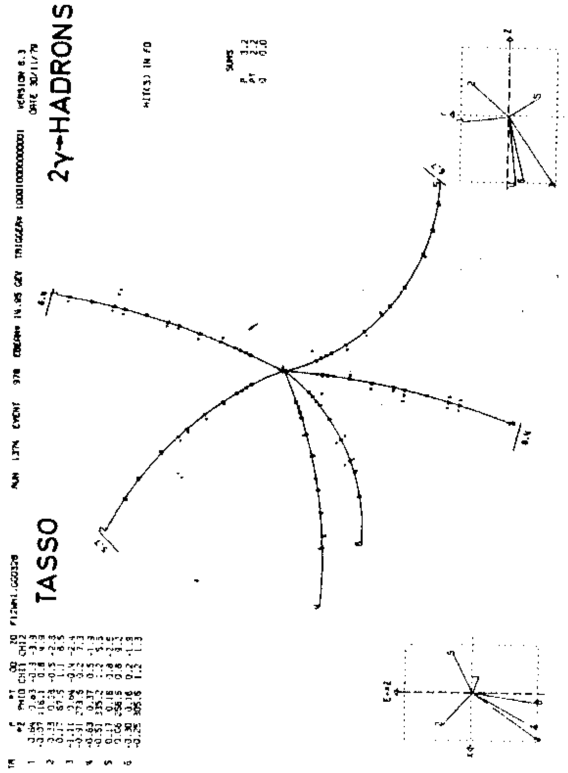

Fig. 4.15 - Candidate for $\gamma\gamma \to q\bar{q} \to$ two jets from TASSO.

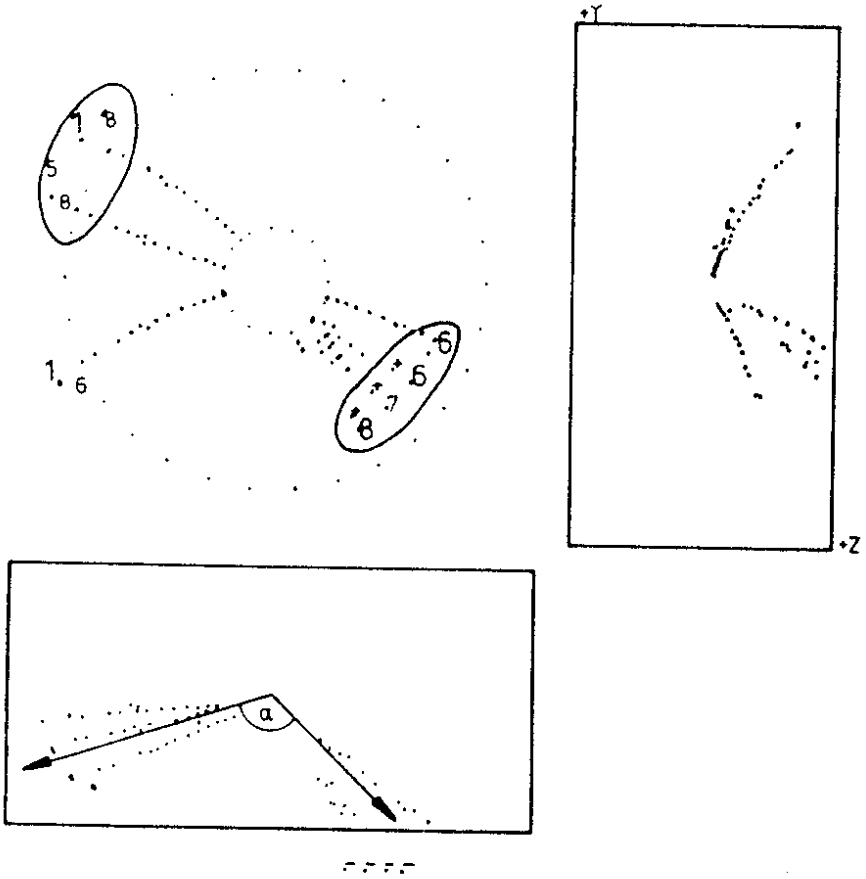

Fig. 4.14 - Candidate for $\gamma\gamma \to q\bar{q} \to$ two jets from PLUTO

31711

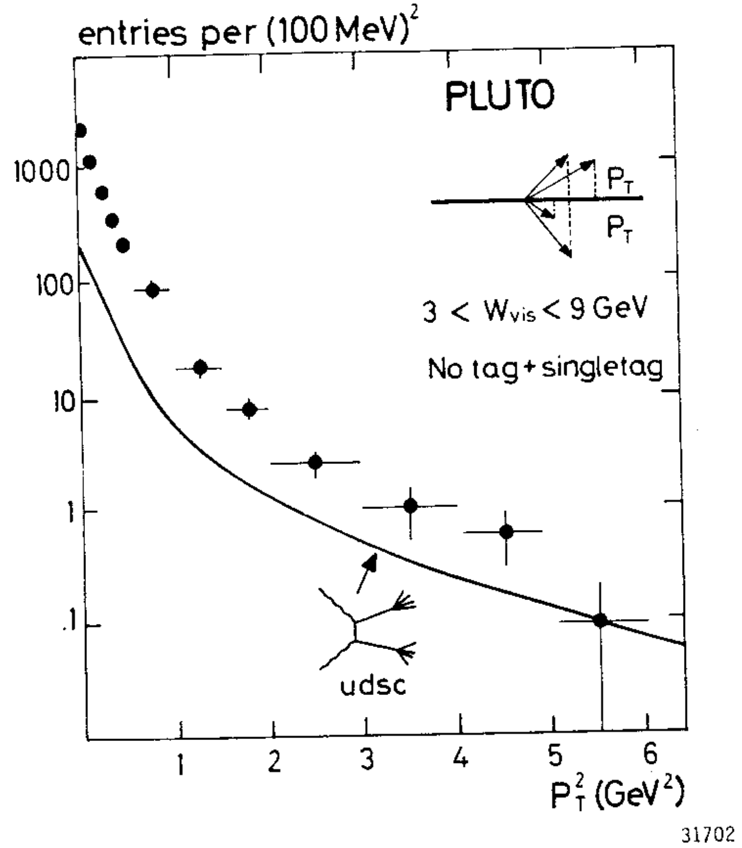

Fig. 4.16 - Number of tracks plotted versus the square of the transverse momentum with respect to the beam axis. The solid curve is a prediction based on $\gamma\gamma \to q\bar{q} \to$ hadrons with q = u, d, s, c quarks. Data are from PLUTO.

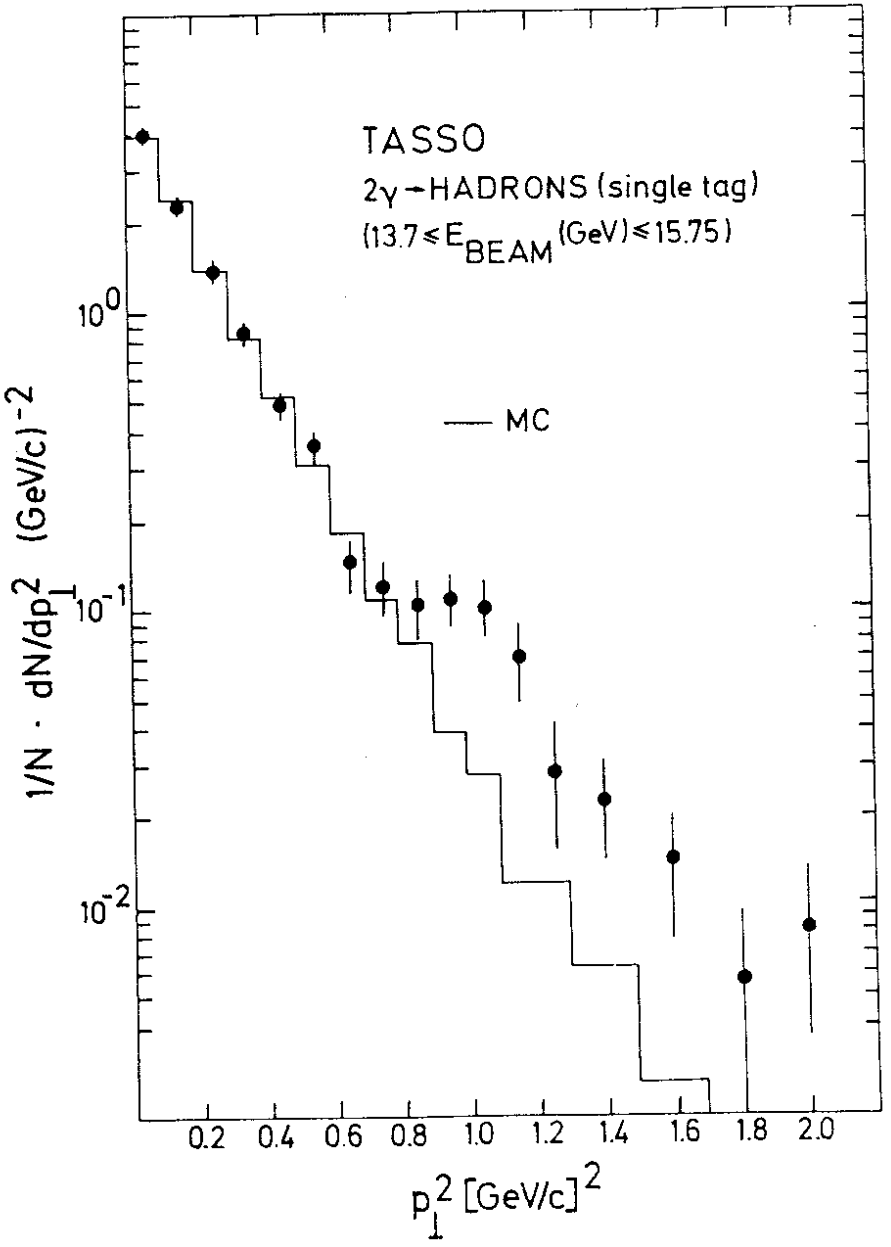

Fig. 4.17 - Distribution of the square of the transverse momentum with respect to the beam axis. Data are from TASSO for the $\gamma\gamma \to$ hadrons with a single tag. Solid line indicates Monte Carlo simulation according to VMD model.

30033

point to possible contributions at high p_T from

$$\gamma\gamma \rightarrow q\bar{q} \rightarrow \text{two jets} \qquad (4.20)$$

As seen from Figs. 4.16 and 4.17, it cannot be said with certainty that (4.20) has been observed unambiguously. It would be very important in the future to extend the data to higher values of p_T and to compare the properties of these observed jets with those from $e^+e^- \rightarrow$ two jets. It is perhaps not unreasonable to entertain the possibility that the jets from $\gamma\gamma$ are different in detailed structure from those of e^+e^- annihilation. If so, we may learn more about the hadronization of the quarks.

4.2.7 Deep inelastic eγ scattering - the photon structure function

Using the large angle tagging, the PLUTO Collaboration has measured the structure function of the photon. As described in section 4.2.2, the large angle tagging extends from 70 mr to 260 mr, and hence the maximum $|Q^2|$ is about 15 GeV^2. Since the other electron or positron is not tagged, the other photon is nearly on mass shell. Accordingly under this configuration the observed $e^+e^- \rightarrow e^+e^-$ + hadrons is closely related to the deep inealstic eγ scattering as shown in Fig. 4.18(a), analogous to for example deep inelastic νp scattering.

If Bjorken scaling applies here, then the photon structure function F_2 is a function of one variable:

$$x = \frac{|Q^2|}{|Q^2| + W^2} \qquad (4.21)$$

On the basis of 120 events where $|Q^2|$ is between 1 and 15 $(\mathrm{GeV}/c)^2$ with $<|Q^2|> = 5\ (\mathrm{GeV}/c)^2$, the PLUTO[55] Collaboration obtains the $F_2(x)$ shown in Fig. 4.19 for the photon.

The Born terms of the photon structure function as well as the higher order corrections can be calculated in QCD. In the leading log approximation we have

$$F_2^{\mathrm{Born}} = \frac{\alpha}{\pi}\,\Sigma e_q^4\, x\,(x^2 + (1-x)^2)\,\ln\frac{Q^2}{\Lambda^2}\ .$$

Note that F_2^{Born} increases with increasing x while vector-dominance model ($F_2^{\mathrm{VDM}} \sim 1-x$) expects a decrease in F_2 with increasing x. F_2^{Born} also shows a scale breaking factor $\ln Q^2/\Lambda^2$.

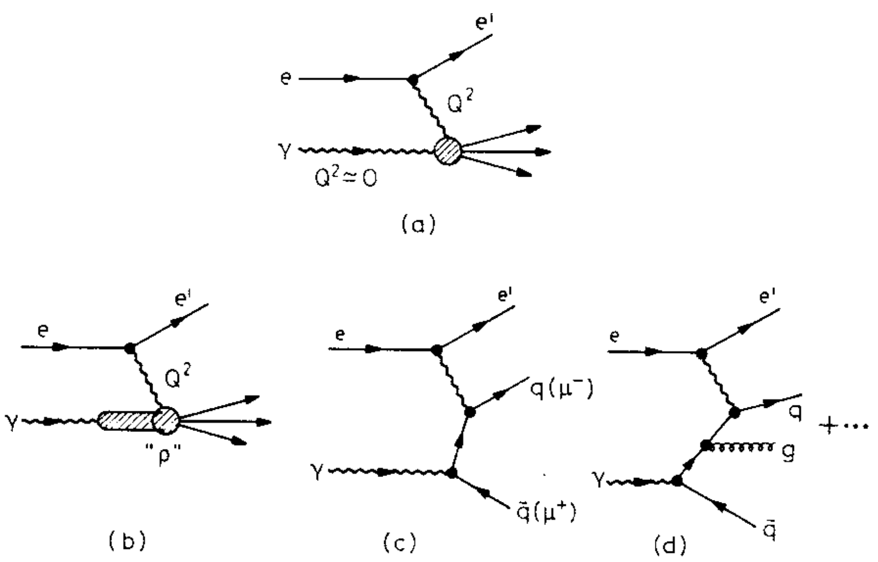

Fig. 4.18 - Diagrams contributing to
$e\,\gamma \rightarrow e'$ hadrons.

31864

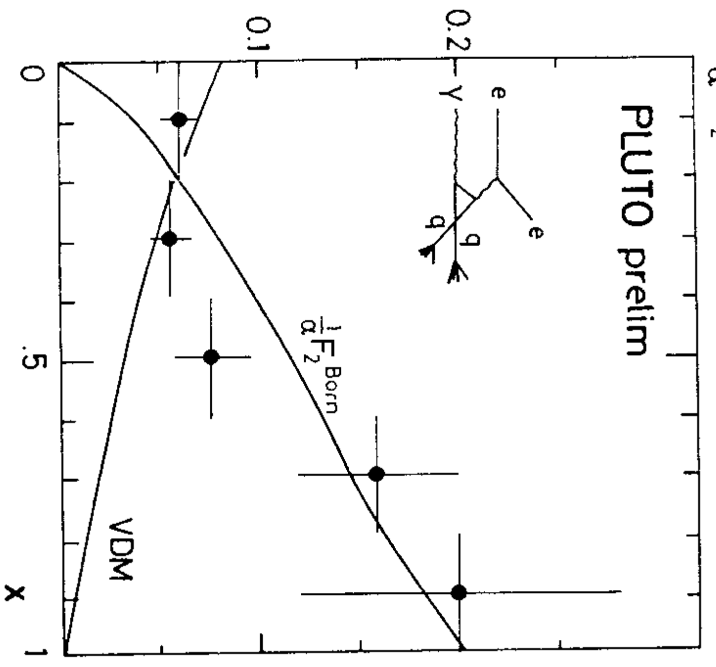

Fig. 4.19 - The photon structure from PLUTO.

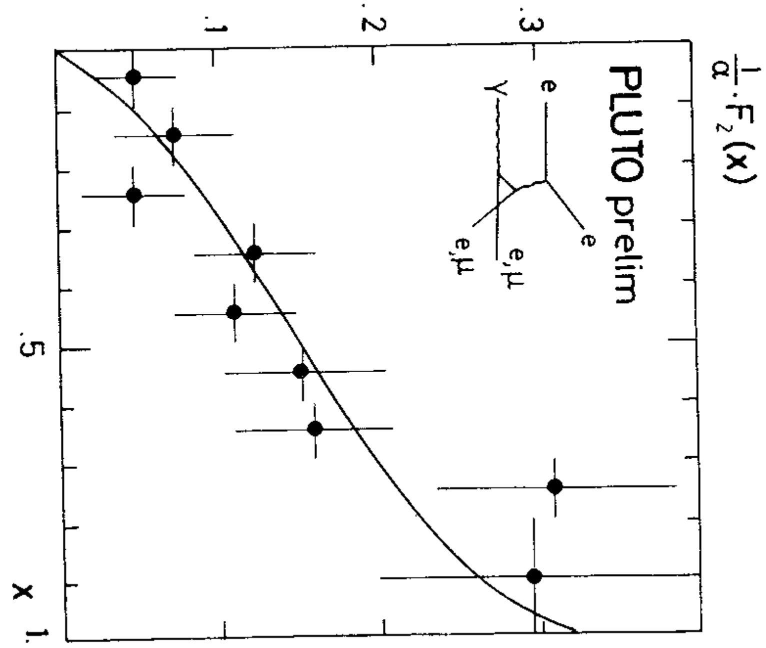

Fig. 4.20 - The lepton structure function from PLUTO.

31701

From the PLUTO data shown in Fig. 4.19, it is clear that the vector-meson dominance model (Fig. 4.18(b)) cannot account for the steep increase of $F_2(x)$ as a function of x, but with a better agreement with the quark model (Fig. 4.18(c)(d)) As a consistency check, the leptonic structure function was determined with the same procedure by using events of the type $e^+e^- \to e^+e^- e^+e^-$ and $e^+e^- \to e^+e^- \mu^+\mu^-$. The result in Fig. 4.20 shows good agreement with QED prediction.

We have therefore seen four separate pieces of evidence that the process $\gamma\gamma \to q\bar{q}$ may be important: from the $\gamma\gamma$ total cross section, the exclusive process $\gamma\gamma \to \rho^o\rho^o$, the high p_T jets, and the photon structure function. Since two-photon physics at such high energies has been investigated only for a few months, further understanding and clarification can certainly be expected in the near future.

4.3 Observation and properties of the gluon

4.3.1 Three-jet events

We shall be concerned mostly with the high-energy data where the center-of-mass energy W is between 27 and 37 GeV. At these energies, most of the hadron events consist of two back to back jets, and are interpreted as the production of a quark-antiquark pair: $e^+e^- \to q\bar{q}$. Last summer, shortly after PETRA reached 27 GeV, the TASSO Collaboration, using a method of generalized sphericity[56], found the first few events with a distinctly different shape. These events, with three jets instead of two, were reported [6,7] just over a year ago. Very soon after, the number of observed three-jet events had increased rapidly [8,9,10,11]. By now, there are several hundred such events from TASSO alone; the precise number is not well defined and depends on the somewhat artificial definition, because a three-jet event gradually changes over to a two-jet event if the angle between two of the jets is reduced. In spite of the ambiguity, the number of the observed three-jet events is roughly five times that expected from statistical fluctuations in the fragmentation process of the above mentioned process $e^+e^- \to q\bar{q}$. Instead, these three-jet events are most naturally explained by hard non-collinear gluon bremsstrahlung[57], $e^+e^- \to q\bar{q}g$, where the quark, the antiquark and the gluon each materializes as a jet of hadrons with limited transverse momentum.

A recent example of a three-jet event from TASSO is shown in Fig. 4.21. This example is especially interesting because, as seen on the right-hand side of Fig. 4.21, there is a 1.67 GeV/c positive track and a 1.32 GeV/c negative track, both entering one of the hadron arms of the TASSO detector and hence identified as K^+ and K^-, respectively. Since the invariant mass is 1.01 GeV, what is seen here is likely to be $\phi \to K^+K^-$.

4.3.2 TASSO method of three-jet analysis

Hansen et al.[5] discovered the two-jet structure of hadrons produced in e^+e^- annihilation by studying sphericity. In view of this success, the method of generalized sphericity[56] was devised to discover three-jet events. Let me describe this method briefly.

Let $\vec{p}_j$, $j = 1 \ldots N$ be the hadronic momenta and $p_{j\alpha}$ $\alpha = 1,2,3$, their rectangular components. From the momentum tensor $\Sigma_j\, p_{j\alpha}\, p_{j\beta}$, which is similar to one used by Bjorken and Brodsky[58], and Hanson et al.[5], one obtains eigenvalues λ_1, λ_2, λ_3 and corresponding eigenvectors $\hat{n}_1$, $\hat{n}_2$, $\hat{n}_3$. Define $Q_k = \lambda_k/(\lambda_1 + \lambda_2 + \lambda_3)$, arranged such that $0 \le Q_1 \le Q_2 \le Q_3$. The physical meaning of these normalized eigenvalues is such that

$Q_1 = \min\limits_{\hat{n}} \Sigma_j\, (\vec{p}_j \cdot \hat{n})^2 \,/\, \Sigma_j\, \vec{p}_j^{\,2}$ gives the flatness of the event ($\hat{n} = \hat{n}_1$),

$Q_2 = \min\limits_{\hat{n}\perp\hat{n}_1} \Sigma_j(\vec{p}_j \cdot \hat{n})^2 \,/\, \Sigma_j\, \vec{p}_j^{\,2}$ gives the width of the event ($\hat{n}=\hat{n}_2$), and

$Q_3 = \max\limits_{\hat{n}} \Sigma_j(\vec{p}_j \cdot \hat{n})^2 \,/\, \Sigma_j\, \vec{p}_j^{\,2}$ gives the length of the event ($\hat{n}=\hat{n}_3$).

Sphericity S and aplanarity A are respectively $3(Q_1 + Q_2)/2$ and $3Q_1/2$; the triangular plot is a two-dimensional plot with axes S and $Y = \sqrt{3}(Q_2-Q_1)/2$. TASSO event distribution at 30 GeV is shown in Fig. 4.22.

To a good approximation, the three jet axes of a three-jet event lie in the event plane defined by $\hat{n}_2$ and $\hat{n}_3$. Let $\vec{q}_j$ be the projection of $\vec{p}_j$ into this event plane, then, unlike $\vec{p}_j$, the $\vec{q}_j$ can be placed in a cyclic order according to their polar angles. Among all partitions of the $\vec{q}_j$ into three contiguous groups, the one which maximizes the sum of "lengths" is found. This particular partition is used to identify the three jets.

Although easy to describe, the justification of this method of generalized sphericity is quite complicated. As emphasized in the original paper, this procedure has the following desirable features.

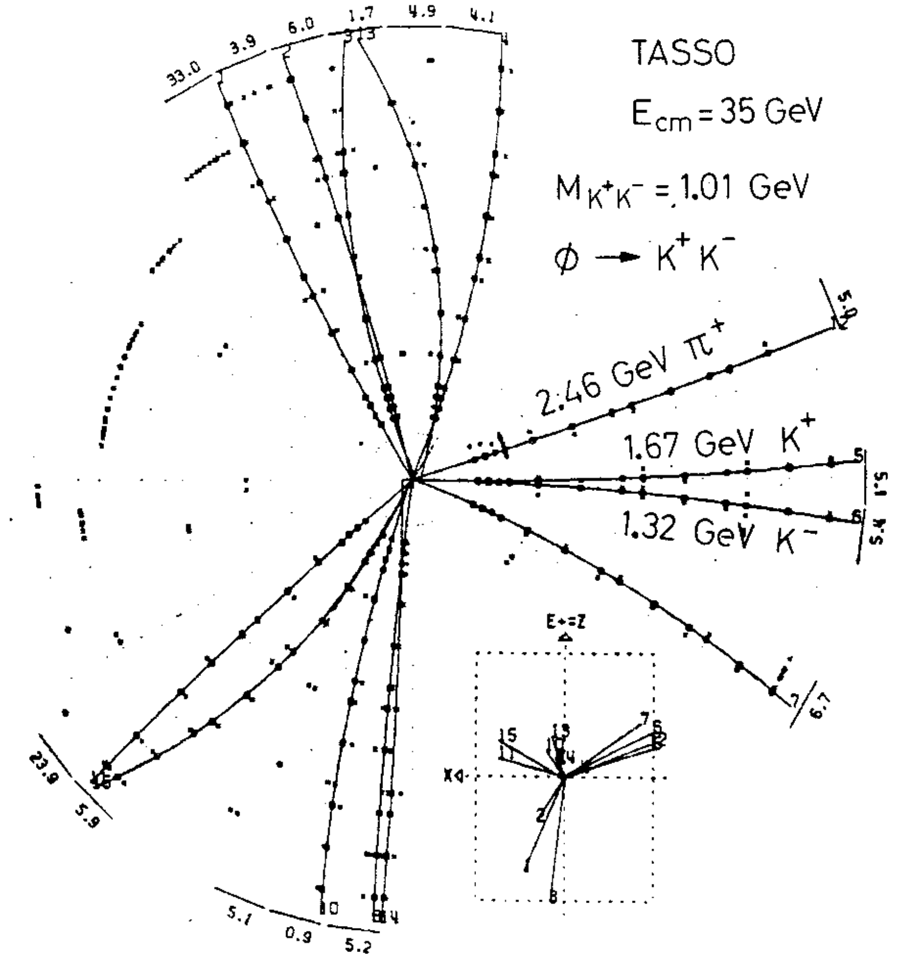

22.9.80

31712

Fig. 4.21 - A three-jet event from TASSO with $\phi \to K^+K^-$ as identified by the Cerenkov counters.

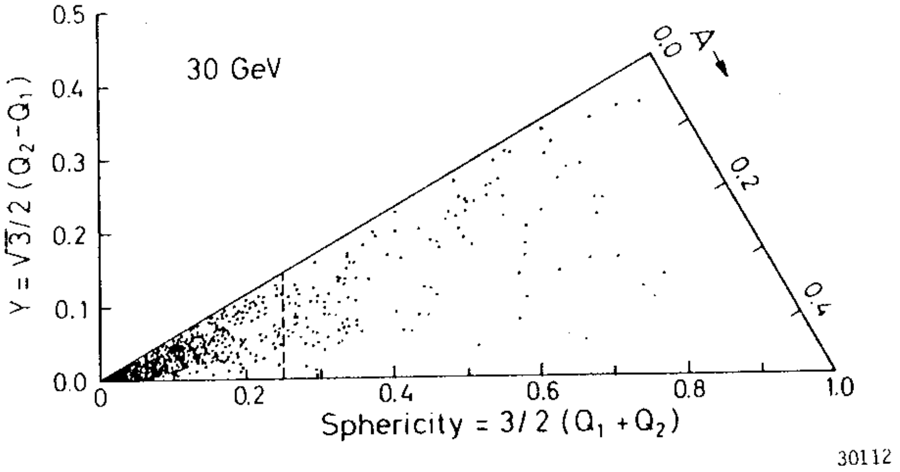

Fig. 4.22 - Distribution of the events from TASSO as a function of sphericity S and aplanarity A.

1. All three jet axes are determined.

2. It is not necessary to have the momenta of all produced particles. For example, this procedure can be used where there is no detection of neutral particles. Of course the loss of information leads to a larger error.

3. All measured momenta can be used; in other words, there is no need to introduce a cutoff for low momenta.

4. Computer time is moderate. For example, with IBM370/168 computer the C.P.U. time is about 1.5 sec for multiplicity 21 and 7 sec for multiplicity 35.

4.3.3 PLUTO method of three-jet analysis

Two different methods of three-jet analysis have been used by the PLUTO Collaboration. The first one is the method of triplicity, due to Brandt and Dahmen[59] and the second method is cluster analysis[60,61]. Since the results I am going to present here will be from the cluster analysis, I shall list here the basic steps in this new method:

A) Find pre-clusters.
B) Form total momentum vector of each pre-cluster.
C) Find clusters of pre-clusters; and
D) identify certain clusters as jets.

The PLUTO Collaboration has carried out this program in several different ways. one of which is as follows: At step (A), only the directions of charged and neutral particles are used, not their momenta. Pre-clusters are thus defined as a collection of particles such that any two of them are within a "collecting angle" α. Typically α is about 30^0. Let $\vec{C}_k$ be the total momentum of a pre-cluster:

$$\vec{C}_k = \sum_{\text{pre-cluster } k} \vec{p}_j \ ,$$

and $\hat{C}_k$ be the unit vector in the direction of $\vec{C}_k$. Pre-clusters are grouped together as clusters if the angle between $\hat{C}_k$ and $\hat{C}_k{}'$ is less then a pre-determined value β (typically 45^0). Finally in step (D), a cluster of particles is identified as a jet if the total energy of all these particles exceeds 2 GeV.

The PLUTO data with center-of-mass energy W between 27 and 32 GeV have been passed through the cluster program. For each event, the number n_J of jets is determined. In the sample of 859 selected hadronic events, 249 have been found to be three-jet candidates. The n_J distribution is shown in Fig.4.23 and is in good agreement with Monte Carlo results for $e^+e^- \to q\bar{q}$ together with

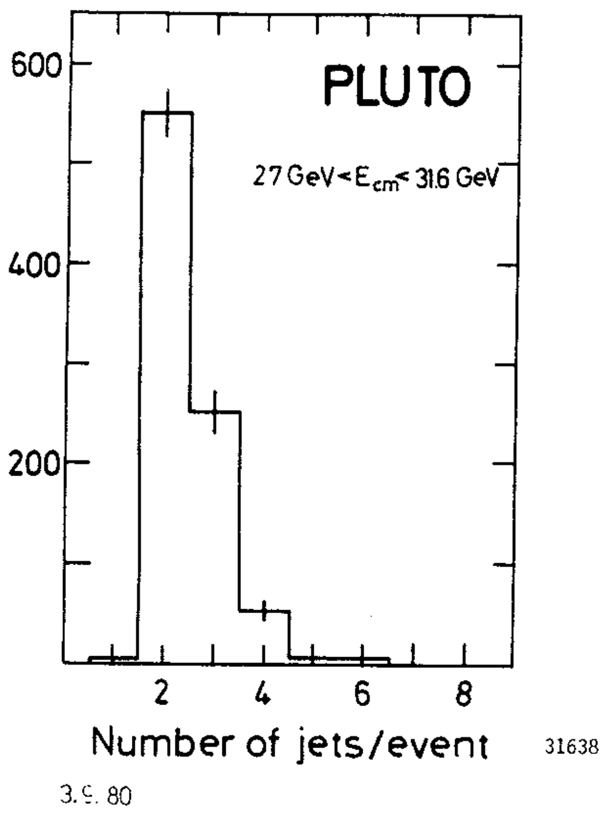

Fig. 4.23 - Distribution of the observed number of jets per event.

gluon bremsstrahlung $e^+e^- \rightarrow q\bar{q}g$ as shown in Table 4.1.

We note that, in the methods described in this and the preceeding section, the jets are treated on entirely equal footing and furthermore no Lorentz transformation is used.

Table 4.1
Distributions of the observed numbers of jets per event (n_J) for PLUTO data and different models, all normalized to the number of observed events. For the $q\bar{q}$ + $q\bar{q}g$-model α_s = 0.15 is assumed.

n_J =	1	2	3	4	5	6	7
Data	2	551	249	53	3	1	
$q\bar{q}$	3	680	152	23	1		
$q\bar{q}g$	2	229	509	113	5	1	
$q\bar{q}$+$q\bar{q}g$	3	567	247	46	2		
Phase space	1	30	154	306	268	86	14

4.3.4 Determination of the quark-gluon **strong** coupling constant α_s

Theorists tell us that it is very easy to determine α_s: it is essentially the ratio of the numbers of three-jet to two-jet events, or similarly that of four-jet to three-jet events. Acutally it is not so simple due to the fragmentation of quarks and gluons and the resulting ambiguity between two- and three-jet events already mentioned in section 4.3.1. Similar ambiguity between three- and four-jet events is even more severe. We shall return to this subject later.

For an accurate determination of α_s, it is essential to use a suitable QCD model. The PLUTO Collaboration chooses that of Hoyer et al.,[62] while the TASSO Collaboration uses that of Ali et al.[63], including in particular the improvements by Sander and Meyer on the Field-Feynman fragmentation[64] and the recent calculations of radiative corrections by Berends and Kleiss[65]. Since α_s measures the quark-gluon coupling, the experimental data used must be those where the gluon plays a significant role.

In order to use these QCD models, the following Field-Feynman parameters must be determined from the experimental data.

A) σ_q - The distribution of the transverse momentum k_T of the quarks in the jet cascade is assumed to be proportional to $\exp(-k_T^2/2\sigma_q^2)$.

B) P/(P+V) - Here P/V is the ratio of primordial pseudoscalar mesons to vector mesons produced in the fragmentation process.

C) a_F - For u, d, and s quarks, the primordial quark fragmentation into a hadron is parametrized as $1-a_F+3a_F(1-z)^2$, where $z = (E + p_\parallel)_h/(E + p_\parallel)_q$.

A simultaneous fit to all data with sphericity S < 0.25 yields the following results from TASSO[66]

$$\sigma_q = 0.32 \pm 0.04 \text{ GeV/c}, \; P/(P+V) = 0.56 \pm 0.15, \; a_F = 0.57 \pm 0.20. \qquad (4.22)$$

The first value may be compared with the PLUTO result

$$\sigma_q = 0.29 \pm 0.03 \text{ GeV/c}.$$

To determine the value α_s the TASSO Collaboration chose the kinematic region S > 0.25 and fit the two dimensional S vs. A distribution as shown in Fig. 4.22. The data with S > 0.25 were analyzed by two different procedures. In the first procedure, α_s is determined without any assumptions on the parameters of jet fragmentation. As shown in Table 4.2[66], we found that the value of α_s is totally insensitive to the values of the fragmentation parameters, and the result[66] is $\alpha_s = 0.16 \pm 0.04$ (statistical).

Table 4.2 - Fitted values of α_s and σ_q for different input values of a_F and P/(P+V)

a_F \ P/(P+V)	0.1	0.3	0.5	0.7	0.9
0.1	α_s = 0.17±0.03 σ_q = 0.44±0.11	0.17±0.03 0.46±0.10	0.17±0.03 0.47±0.10	0.16±0.03 0.48±0.09	0.16±0.03 0.48±0.08
0.3	α_s = 0.17±0.04 σ_q = 0.42±0.12	0.16±0.04 0.44±0.11	0.16±0.04 0.46±0.10	0.15±0.04 0.47±0.09	0.15±0.04 0.48±0.08
0.5	α_s = 0.17±0.04 σ_q = 0.35±0.12	0.16±0.04 0.38±0.12	0.16±0.04 0.41±0.12	0.15±0.04 0.43±0.10	0.14±0.04 0.44±0.09
0.7	α_s = 0.17±0.03 σ_q = 0.28±0.09	0.17±0.04 0.30±0.10	0.16±0.04 0.33±0.10	0.15±0.05 0.36±0.10	0.14±0.05 0.39±0.09
0.9	α_s = 0.17±0.03 σ_q = 0.21±0.08	0.17±0.04 0.23±0.08	0.16±0.04 0.26±0.08	0.15±0.04 0.30±0.09	0.14±0.05 0.33±0.08

To further reduce this error, in the second producedure, the result in (4.22) on the parameters of jet fragmentation is used. The result is consistent with the previous one, but of improved statistical accuracy:

$$\alpha_s = 0.17 \pm 0.02 \text{ (statistical)} \pm 0.03 \text{ (systematic)}.$$

It should be pointed out that in the QCD model of Ali et al.,[63] up to order of α_s^2, all the bremsstrahlung diagrams are included but not the virtual correction diagrams. Hence we must emphasize that this value of α_s should be taken within the context of the QCD model used.

The question may be raised whether this determination of α_s is sensitive to the particular distribution used in the triangular plot and the cut in sphericity. In Table 4.3 we show the results of applying the second procedure for various distributions and cuts. It is seen that the values of α_s obtained in this way are always between 0.16 and 0.19. This investigation, as well as the comparison with the model of Hoyer et al.[62] ($\alpha_s = 0.19 \pm 0.02$), led to the estimate of the systematic error given above.

Table 4.3 - α_s from various distributions and using different cuts (errors are statistical)

Distribution	cut	α_s
triangular plot (S vs A)	S > 0.25 All S	0.17 ± 0.02 0.18 ± 0.01
S	All S S > 0.2 S > 0.25	0.18 ± 0.01 0.17 ± 0.01 0.18 ± 0.01
A	All A A > 0.050 A > 0.060	0.16 ± 0.01 0.16 ± 0.01 0.17 ± 0.02
Q_2	All Q_2 Q_2 > 0.12 Q_2 > 0.14 Q_2 > 0.16	0.19 ± 0.01 0.18 ± 0.01 0.17 ± 0.02 0.17 ± 0.02
Y	Y > 0.10 Y > 0.15	0.18 ± 0.02 0.19 ± 0.02
Thrust T	All T T < 0.95 T < 0.90	0.19 ± 0.01 0.19 ± 0.01 0.18 ± 0.01

In QCD, α_s is expressed as

$$\alpha_s = \frac{12\pi}{(33 - 1N_f)\ \ln\ (Q^2/\Lambda^2)} \tag{4.23}$$

where N_f is the number of flavors , five for the energy range under consideration. It is less clear what Q^2 should be. With our value $S > 0.25$, and with Q identified with the center-of-mass energy (E_{cm} = 30 GeV), then Λ = 0.24 GeV. However, one could define alternatively by identifying Q^2 with the average mass squared of the virtual quark or antiquark. In this case $\langle Q^2 \rangle$ is found to be 140 GeV^2 and accordingly Λ = 0.095 GeV.

Using the sample of 249 three-jet events found by the cluster analysis method, the PLUTO Collaboration[61] found, after correcting for detector efficiencies, radiation and fragmentation:

$$\alpha_s = 0.15 \pm 0.03\ \text{(stat.error)} \pm 0.02\ \text{(syst.error)}.$$

The systematic error reflects the uncertainties introduced by cuts and the models, but does not take into account next order QCD effects. The correlation between α_s and σ_q is particularly small. Even assuming extreme values for σ_q such as 250 MeV and 350 MeV changes α_s only by +0.004 and -0.009 respectively.

In Table 4.4 we summarize all the PETRA results on α_s. As usual, the systematic error is given after the statistical error.

Table 4.4 - Values of the quark-gluon strong coupling constant α_s as determined by various collaborations at PETRA

MARK J[67]	0.23 ± 0.02 ± 0.04
TASSO [66]	0.17 ± 0.02 ± 0.03
PLUTO[61]	0.15 ± 0.03 ± 0.02
JADE [68]	0.18 ± 0.03 ± 0.03

4.3.5 Determination of the gluon spin

The gluon spin has been determined to be 1 from the three-jet events by both the TASSO [69] and PLUTO [61] Collaborations.

Before fragmentation, the $q\bar{q}g$ Dalitz plot can be described by the fractional energy variables

$$x_i = E_i \ / \ E_B \tag{4.24}$$

where E_i is the energy of quark or gluon i and E_B is the incident beam energy, so that

$$x_1 + x_2 + x_3 = 2. \tag{4.25}$$

We choose to order them such that,

$$x_3 \leq x_2 \leq x_1 \tag{4.26}$$

which implies

$$2/3 \leq x_1 \leq 1.$$

If the quarks and the gluon have negligible masses relative to E_B, the x_i are determined by the angles θ_i shown in Fig. 4.24(a):

$$x_i = \frac{2\ \sin\theta_i}{\sin\theta_1 + \sin\theta_2 + \sin\theta_3}$$

Furthermore, x_1 is then the thrust T of the $q\bar{q}g$ system. Thus, the three-jet directions completely define the $q\bar{q}g$ Dalitz plot.

Fig. 4.24(b) shows the angle $\tilde{\vartheta}$ suggested by Ellis and Karliner[70] to discriminate between vector and scalar gluons. In this figure, the $q\bar{q}g$ system has been Lorentz boosted to the center-of-momentum frame of partons 2 and 3. Assuming negligible quark and gluon masses, $\cos\tilde{\vartheta}$ is given by

$$|\cos\tilde{\vartheta}| = \frac{x_2 - x_3}{x_1} = \frac{\sin\theta_2 - \sin\theta_3}{\sin\theta_1} \tag{4.27}$$

The distribution function for the x_i in QCD and in the scalar gluon model, after averaging over the production angles relative to the incident e^+e^- beams, are given by[57]

$$\text{vector:}\quad \frac{1}{\sigma_0}\left(\frac{d\sigma}{dx_1 dx_2}\right)_V = \frac{2\alpha_s}{3\pi}\left[\frac{x_1^2+x_2^2}{(1-x_1)(1-x_2)} + \begin{matrix}\text{cyclic}\\ \text{permut.}\\ \text{of } 1,2,3\end{matrix}\right] \tag{4.28}$$

$$\text{scalar:}\quad \frac{1}{\sigma_0}\left(\frac{d\sigma}{dx_1 dx_2}\right)_S = \frac{\tilde{\alpha}_s}{3\pi}\left[\frac{x_3^2}{(1-x_1)(1-x_2)} + \begin{matrix}\text{cyclic}\\ \text{permut.}\\ \text{of } 1,2,3\end{matrix}\right] \tag{4.29}$$

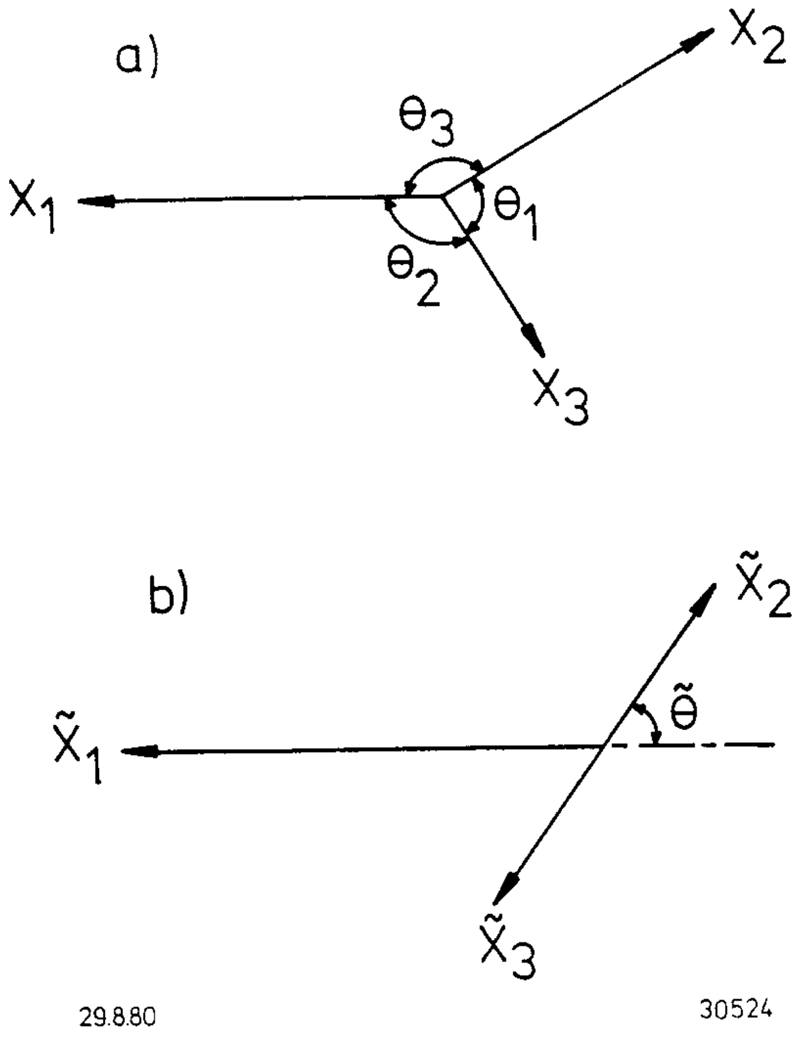

Fig. 4.24 a) Momenta and angles of a $q\bar{q}g$ final state in the center-of-momentum frame.
b) The $q\bar{q}g$ final state transformed to the rest frame of particles 2 and 3.

To avoid a number of difficulties associated with the singularities of these distributions at $x_1 = 1$, the TASSO Collaboration used the kinematic region defined by $1 - x_1 > 0.10$. In the three-jet region so defined, the distributions are not strongly peaked either for vector or scalar gluons, making the dependence on fragmentation smearing small. As a further precaution we only used distributions normalized to the number of events in this kinematic region. This means that the distinction between vector and scalar gluons is made only on the basis of the difference in shape of the two distributions in the three-jet region. In this way one eliminate, on the parton level, all dependence of our spin analysis on the values of the strong coupling constant α_s and $\tilde{\alpha}_s$ for vector and scalar gluons, respectively.

With this cut and the parameters of (4.22), the observed distribution of $|\cos\tilde{\theta}|$ is compared with the results for vector and scalar gluons in Fig. 4.25(a).

The model curves are normalized to 277 events[71]. The data clearly favor spin 1 over spin 0. The χ^2 values for 3 degrees of freedom calculated taking the finite statistics of the Monte Carlo into account are

$\chi^2 = 3.38$ CL 33% for vector gluons
$\chi^2 = 26.3$ CL 0.001% for scalar gluons

Thus, vector gluons are consistent with the data but scalar gluons are disfavored by 4.4 standard deviations.

Another way to express the result is to compare the mean of $|\cos\tilde{\theta}|$. From the data

$$<|\cos\tilde{\theta}|>_{exp} = 0.353 \pm 0.012$$

while for the vector and scalar gluon calculations,

$$<|\cos\tilde{\theta}|>_V = 0.341 \pm 0.004$$

$$<|\cos\tilde{\theta}|>_S = 0.298 \pm 0.003.$$

Combining the errors in quadrature, the data differ from the calculation by

0.9 standard deviations (CL = 37%) for vector gluons
4.5 standard deviations (CL = 0.001)% for scalar gluons,

again highly favoring spin 1 over spin 0.

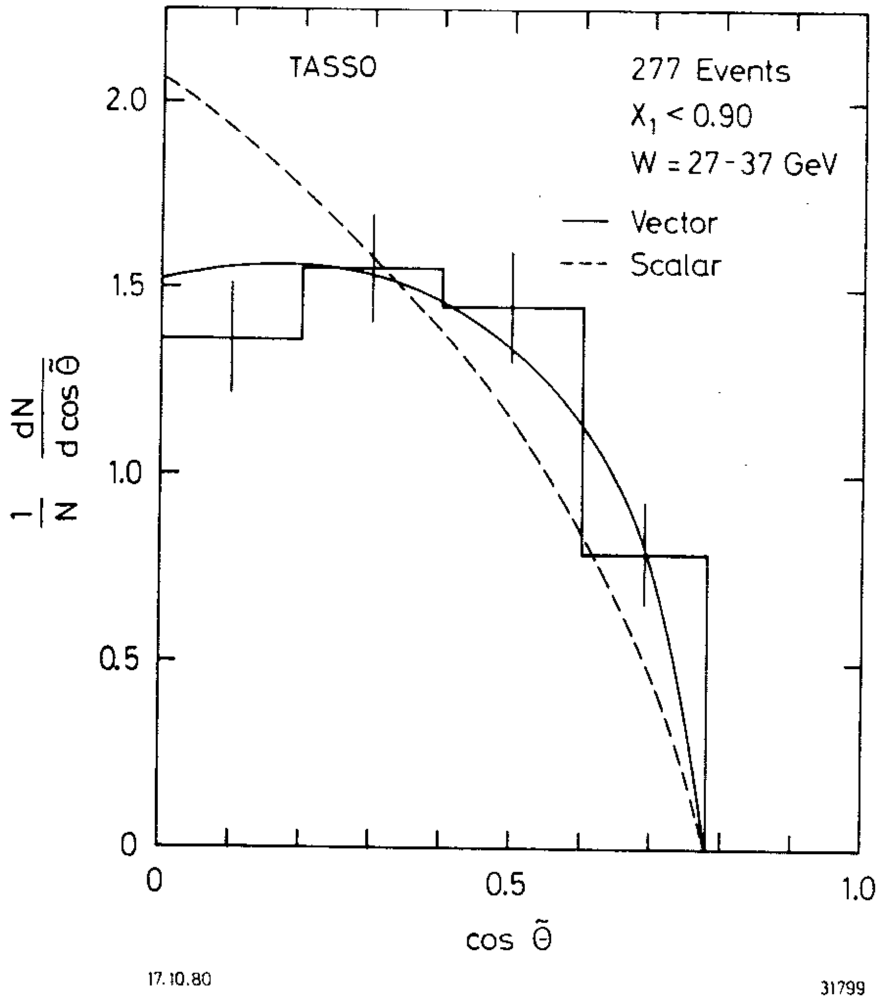

Fig.4.25(a) Observed distribution of the data in the region $1-x_1 > 0.10$, as a function of the cosine of the Ellis-Karliner angle $\tilde{\vartheta}$ defined in Fig. 4.24(b). The solid line shows the QCD prediction, the dotted line the prediction for scalar gluons, both normalized to the number of observed events.

Best use of the information contained in the x_1 distributions is of course made by a two-dimensional analysis. This is difficult with a small number of events. There is however an optimal way to rebin the two-dimensional distribution to one dimension. Let D be any observed two-dimensional distribution, and let D_S and D_V be the corresponding distributions for two different hypotheses. For the purpose of distinguishing D_S and D_V, the optimal way of obtaining a one-dimensional distribution with the least loss of information is the one where the events corresponding to the same D_S/D_V are binned together. Any other way of forming a one-dimensional distribution from the two-dimensional one, involves adding together events of larger ratio D_S/D_V with those of smaller D_S/S_V causing a partial cancelling of information.

When this general procedure is applied to the present case, D_S and D_V are the two dimensional distributions corresponding to spin 0 and spin 1 after jet analysis and going through the detector. They are therefore very difficult to determine. We have used instead the variable, derived from equations (4.28) and (4.29)

$$\xi = 2\left[\frac{x_3^2}{(1-x_1)(1-x_2)} + \text{permut.}\right] \Bigg/ \left[\frac{x_1^2 + x_2^2}{(1-x_1)(1-x_2)} + \text{permut.}\right]$$

$$= 2\left[\frac{x_1^2 + x_2^2 + x_3^2}{x_1^3 + x_2^3 + x_3^3} - 1\right] \qquad (4.30)$$

This approximation corresponds to the negligence of fragmentation of jets and detector efficiency. The factor of 2 is included so that $0 \leq \xi \leq 1$. Fig. 4.25(b) shows the contours of constant ξ plotted in the (x_1, x_2, x_3) plane.

With this variable, it is found from the TASSO data that

$$\langle\xi\rangle_{exp} = 0.663 \pm 0.011$$
$$\langle\xi\rangle_V = 0.666 \pm 0.003$$
$$\langle\xi\rangle_S = 0.703 \pm 0.003$$

Hence with this method we obtain

0.3 standard deviations (CL =79 %) for vector gluons
and 3.6 standard deviations (CL = 0.03%) for scalar gluons.

This supports our conclusions from the analysis of $\langle|\cos\tilde{\vartheta}|\rangle$.

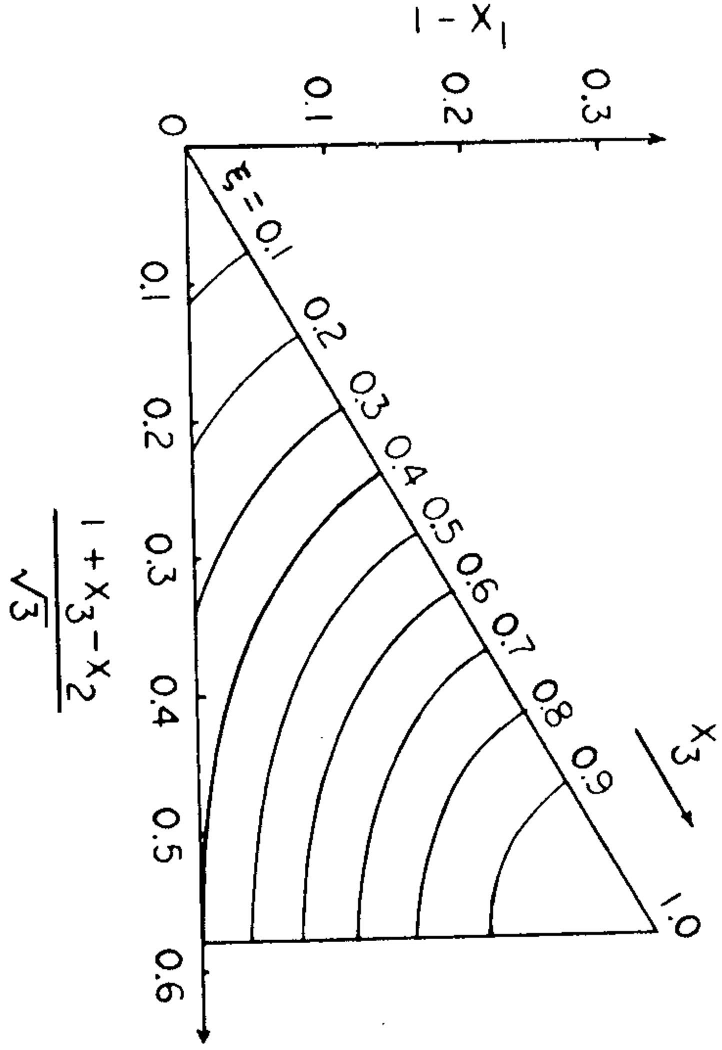

Fig. 4.25(b) The contours of constant ε plotted in the (x_1, x_2, x_3) plane.

Using the cluster analysis method, the PLUTO Collaboration[61] plotted the x_1 distributions of the three-jet events as shown in Fig. 4.26 (a) and (b). The solid curve in the Fig. 4.26(a) is the prediction from first order QCD for vector gluons. A fit of the scalar gluon prediction[57] to the data points yields a $\chi^2/ND = 9.1/4$ as shown in Fig. 4.26 (b) (dashed curve). If one averages the x_1-distribution for $2/3 < x_1 < 0.95$, the predictions for vector and scalar gluons are 0.891 and 0.871 respectively. For the data obtained by PLUTO $\langle x_1 \rangle = 0.893 \pm 0.005$. Hence the hypothesis of scalar gluons is strongly disfavored.

4.3.6 Energy-energy correlations

We report a study by the PLUTO Collaboration[72] on energy-energy correlations defined by

$$f(\theta) = 2 \sum_{a,b} \iint \frac{d^3\sigma}{dz_a dz_b d\theta_{ab}} z_a z_b dz_a dz_b \qquad (4.31)$$

where z_a, z_b are the fractional energies $(E_{a,b}/E_{cm})$ carried away by hadrons a and b, and θ_{ab} is the angle between their directions of flight.

In Fig. 4.27 the resulting energy-energy correlations are shown in the range of energies between 7.7 and 31.6 GeV. The data below 12 GeV are from an earlier experiment at DORIS[73]. At the lowest energies the data show little structure, but with rising energy the peaks at around 50^0 and 150^0 move away from the valley at 90^0 and become more pronounced. This behavior reflects the increasing development of two distinct jet structures. Above 20 GeV these peaks have moved towards small values of θ and 180-θ, and within errors the data have become nearly energy independent. This behavior is well reproduced by the Monte Carlo simulation[62], as indicated by the full curves in Fig. 4.27.

As a possible alternative description of these data PLUTO also shows in Fig. 4.27 as dashed curves the predictions from a model[74] which uses the leading log same side predictions[74] for the angular range $\theta \lesssim 50^0$, first order calculations[75] in the central region $50^0 \lesssim \theta < 120^0$ and leading log opposite side predictions[76] in the backward regime $120^0 < \theta$. The dotted lines represent the continuation of these predictions out of the regions defined above. These predictions depend on only one parameter, namely the strong coupling constant α_s or the QCD scale parameter Λ. The value Λ = 200 MeV has been taken, corresponding to $\alpha_s = 0.165$ at $E_{cm} = 30$ GeV.

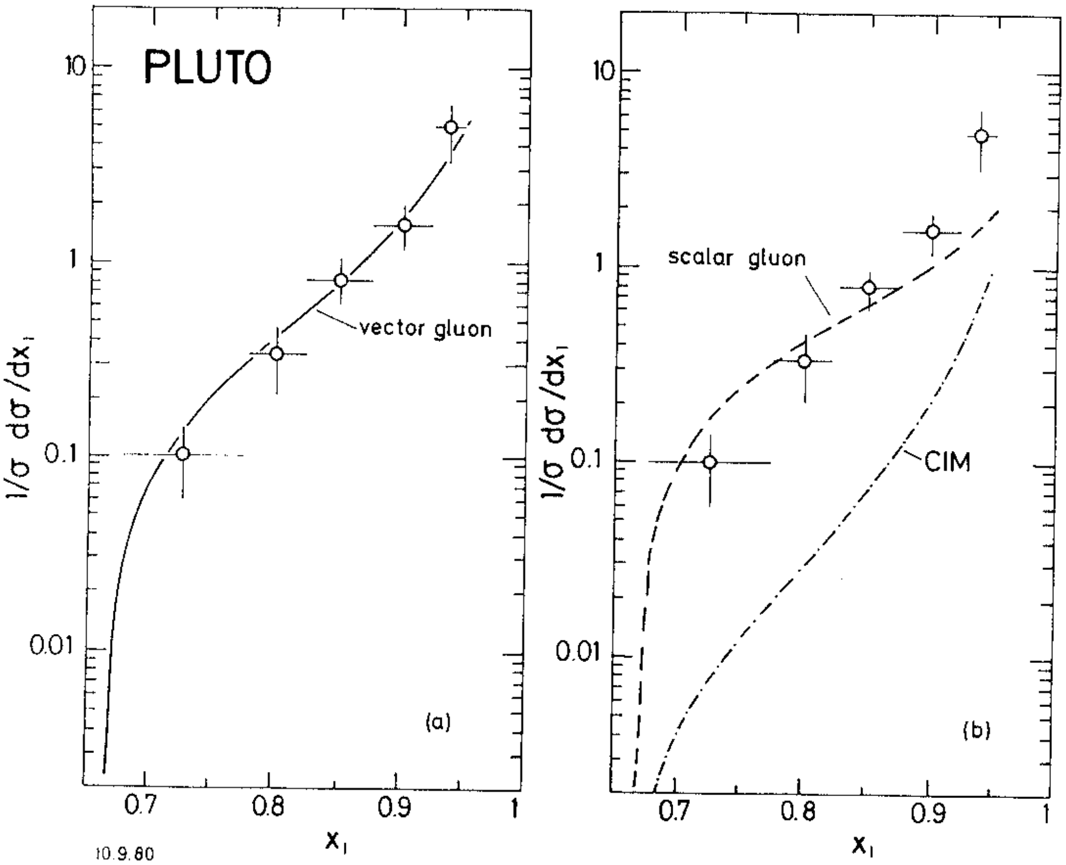

10.9.80

31639

Fig. 4.26 Distribution of the relative energy of the fastest parton (x_1). The data points are corrected for detector acceptance, radiation and hadronisation. The curves are (a) first order QCD, (b) dotted: scalar gluon hypothesis and dashed dotted: CIM(Constituent Interchange Model).

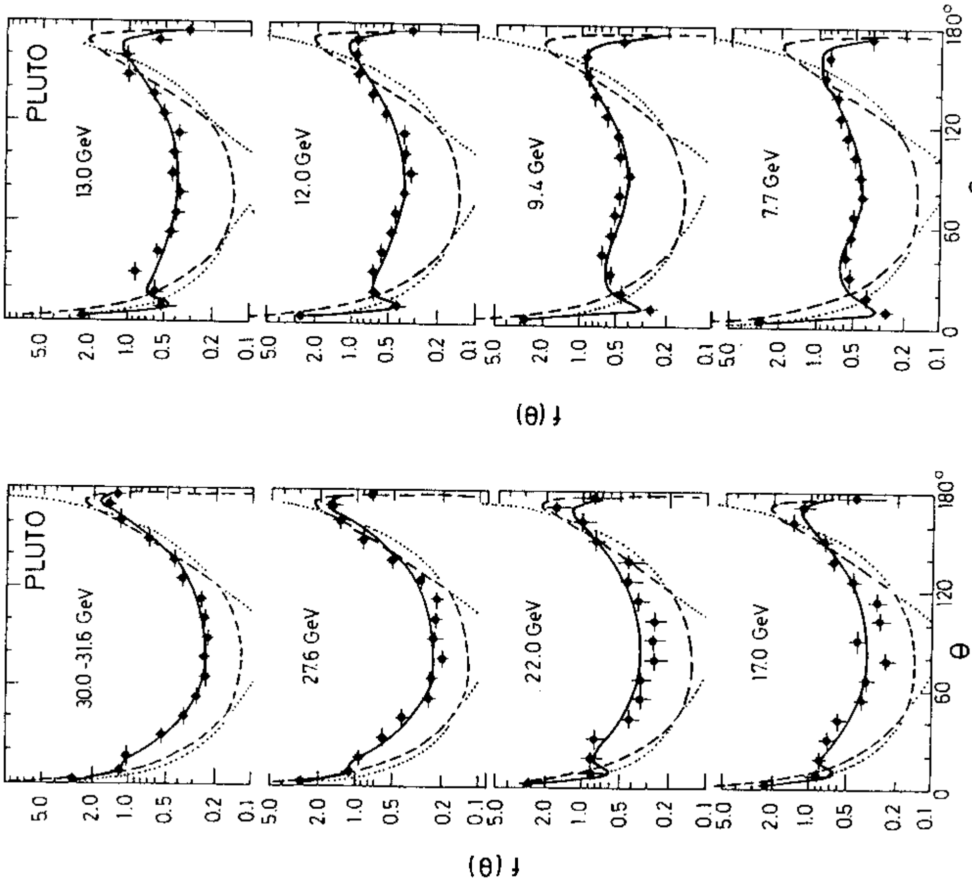

Fig 1a

31861

Fig. 4.27 - Energy-energy correlations from PLUTO data and theoretical predictions.

4.4 Four-jet analysis

Since there are three-jet events, there must also be four-jet events[77] With the three-jet events interpreted as gluon bremsstrahlung, double gluon bremsstrahlung leads to four-jet events:

$$e^+e^- \rightarrow q\bar{q}gg\ .$$

Alternatively, the bremsstrahlung gluon may materialize into a $q\bar{q}$ pair.

$$e^+e^- \rightarrow q\bar{q}q\bar{q}\ .$$

The lowest-order QCD diagrams for these two types of four-jet events are shown respectively in Fig. 4.28(a) and Fig. 4.28 (b). With α_s determined (see Table 4.4), the number of four-jet events can in principle be calculated.

Experimentally, a few clear four-jet events have been seen, with one example shown in Fig. 4.29. However, the ambiguity between three- and four-jet events is even more severe than that between two- and three-jet events, because any two of the four jets may make a small angle with each other. A plot of the 191 TASSO events with $S > 0.25$ is shown in Fig. 4.30. together with the Monte-Carlo result, as a function of the aplanarity A. In this and in a number of similar plots, the number of three-jet events is everywhere larger than that of four-jet events. Nevertheless, subtracting from the experimental data the $q\bar{q}$ and the $q\bar{q}g$ contributions according to the QCD model of Ali et al.[63] there remains a total of 36 four-jet events, in good agreement with the expectation for four-jet events from the QCD model calculation.

We discuss here the TASSO method of four-jet analysis[78]. In principle, four-jet analysis can be carried out by partitioning the observed tracks into four subsets and minimizing the sum of the sphericities (or maximizing the sum of the thrusts) of these four subsets. Similar to the case of the three-jet analysis, the fundamental difficulty of the four-jet analysis is due to the extremely large number of partitions. The number of ways to partition N observed tracks into four non-empty sets is

$$\frac{1}{6}\,(4^{N-1} - 3^N + 3.2^{N-1} - 1). \qquad (4.34)$$

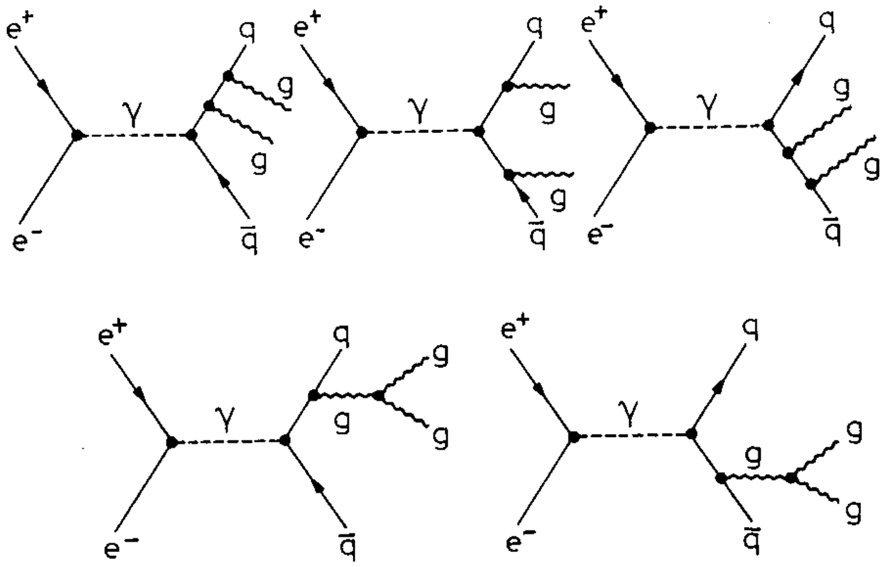

(a) $e^+e^- \rightarrow q\bar{q}\,gg$

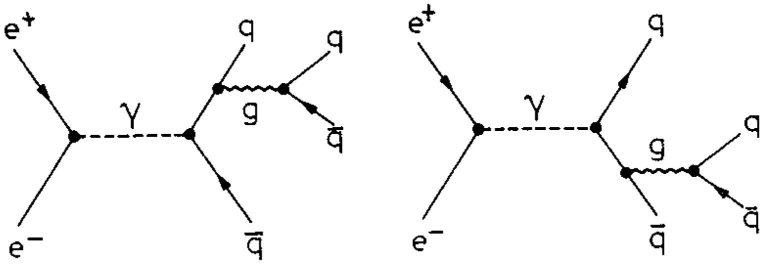

(b) $e^+e^- \rightarrow q\bar{q}\,q\bar{q}$

15.12.80

32105

Fig. 4.28 - Feynman diagrams for four-jet events.

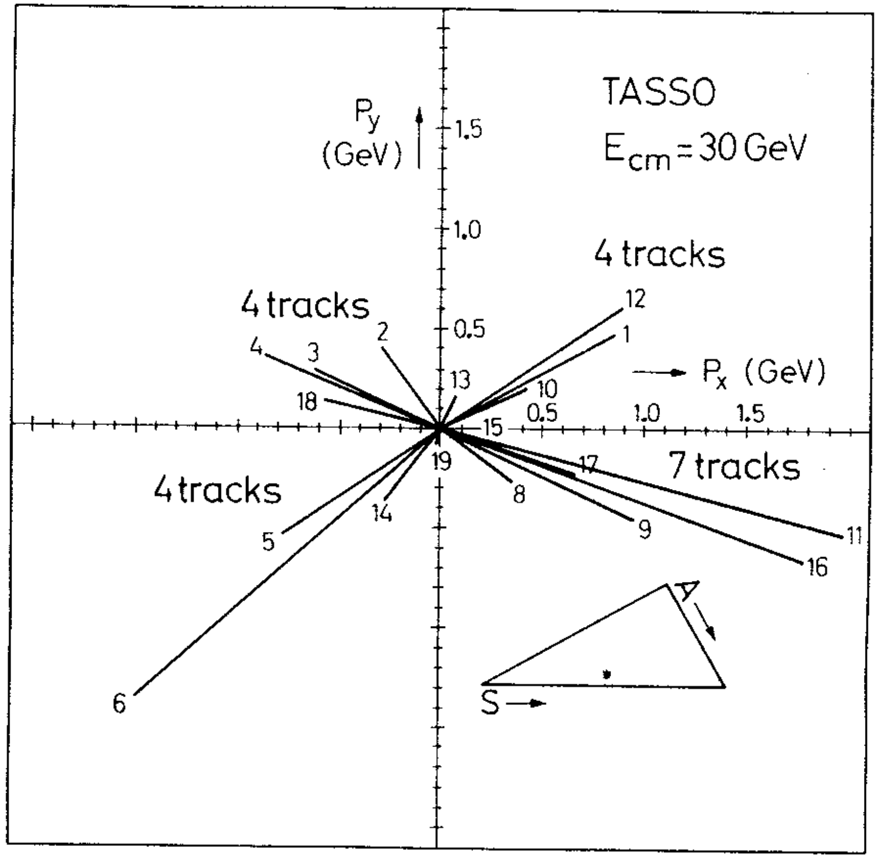

22.9.80 31714

Fig. 4.29 - A TASSO four-jet event viewed on the event plane.

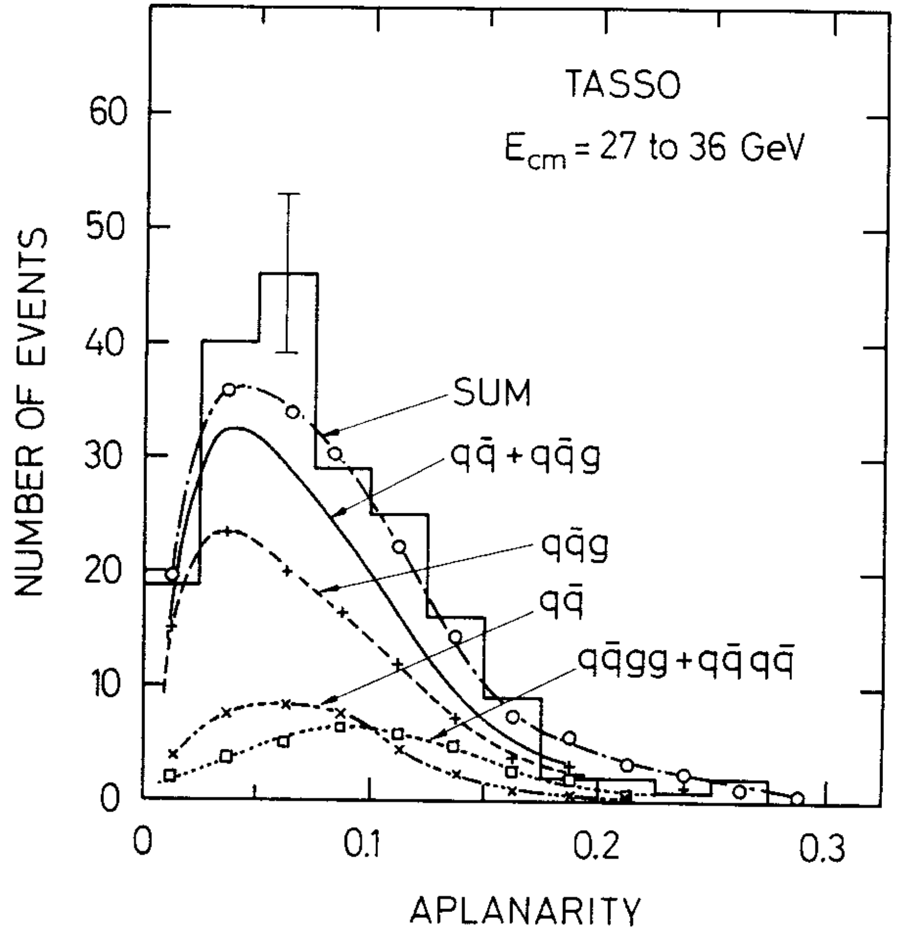

22.9.80 31717

Fig. 4.30 - Distribution of events as a function of aplanarity for S > 0.25.

This number is ridiculously large even for moderate values of N; it is for example1.8 x 10^{11} for N = 21. It is just about impossible to search over such a large number of combinations.

In the case of three-jet analysis, an efficient way to reduce greatly the number of combinations is to project all the measured momenta into the event plane, as explained in section 4.3.2. The main point there is that the projections can be placed in a cyclic order according to their polar angles, and only contiguous partitions need to be studied. In the present case of four-jet analysis, no event plane can be usefully defined, and hence a new idea is needed. The idea is to apply the three-jet analysis twice. Suppose the three-jet analysis of section 4.3.2 is applied to a four-jet event, then in most cases two of the four jets are not separated in this projection. More precisely, when the three-jet analysis of reference 56 is applied to a four-jet event, then in most cases two of the three partitions consist of one jet each, while the third partition contains two jets. Occasionally, one of the four jets is divided between two of the partitions; thus one of the partitions concists of one jet while the other three jets are split between the other two partitions. Only very rarely is one of the four jets divided between all three partitions. We ignore these very rare cases. By identifying the "thinnest" of the three partitions as one jet, its removal makes it possible to apply the three-jet analysis a second time to identify the other three jets. More precisely, the procedure followed for the four-jet analysis is as follows.

A) Use the program for three-jet analysis.

B) Determine the three jet axes by adding the momenta of the tracks in the jet. In general these three jet axes are not coplanar.

C) Find the average transverse momenta for the three jets with respect to their own jet axes as defined above. To avoid possible confusion with the average transverse momenta used in the three-jet analysis, let us call them <PT'>.

D) Among the three jets being considered so far, define jet A as the one with the smallest value of <PT'>

E) Remove all the tracks of jet A, and study the remaining tracks, i.e. the tracks that are not in jet A.

F) Add up the energies and momenta of these remaining tracks to find the motion of the center of mass. Perform a Lorentz transformation to this center of mass of these remaining tracks.

G) Apply three-jet analysis to the transformed momenta for these remaining tracks. This gives the three new partitions. In particular, determine whether this is itself a three-jet event.

H) If these remaining tracks form an acceptable three-jet event, go back to the original laboratory coordinate system.

I) In the laboratory coordinate system, determine the four jet axes by adding up the momenta of the tracks in each jet.

J) Find the angles between all the momentum directions and all the four jet axes. Each momentum should make the smallest angle with respect to the jet axis that it belongs to. If this is indeed the case, then the jet axes have been found properly.

K) If not, then such a momentum should be reassigned to the jet that gives the smallest angle. After reassignment, repeat steps I and J.

L) The energies of the four jets are determined under the assumption that the jet masses can be neglected. Let $\hat{n}_i$ with i = 1, 2, 3, and 4 be the unit vectors in the directions of the jet axes, then the energies E_i of the jets are determined by the energy-momentum conservation

$$\sum_{i=1}^{4} E_i \hat{n}_i = 0$$
$$\sum_{i=1}^{4} E_i = E_{cm} . \qquad (4.32)$$

As an illustration, the method is applied to a TASSO event of large sphericity S and large aplanarity A. As shown in the triangular plot of Fig. 4.31 (a), S = 0.56 and A = 0.14 for this particular event. The first application of the three-jet analysis (step A) gives in the event plane the result of Fig. 4.31 (b). There are three groups with respectively 4, 7,

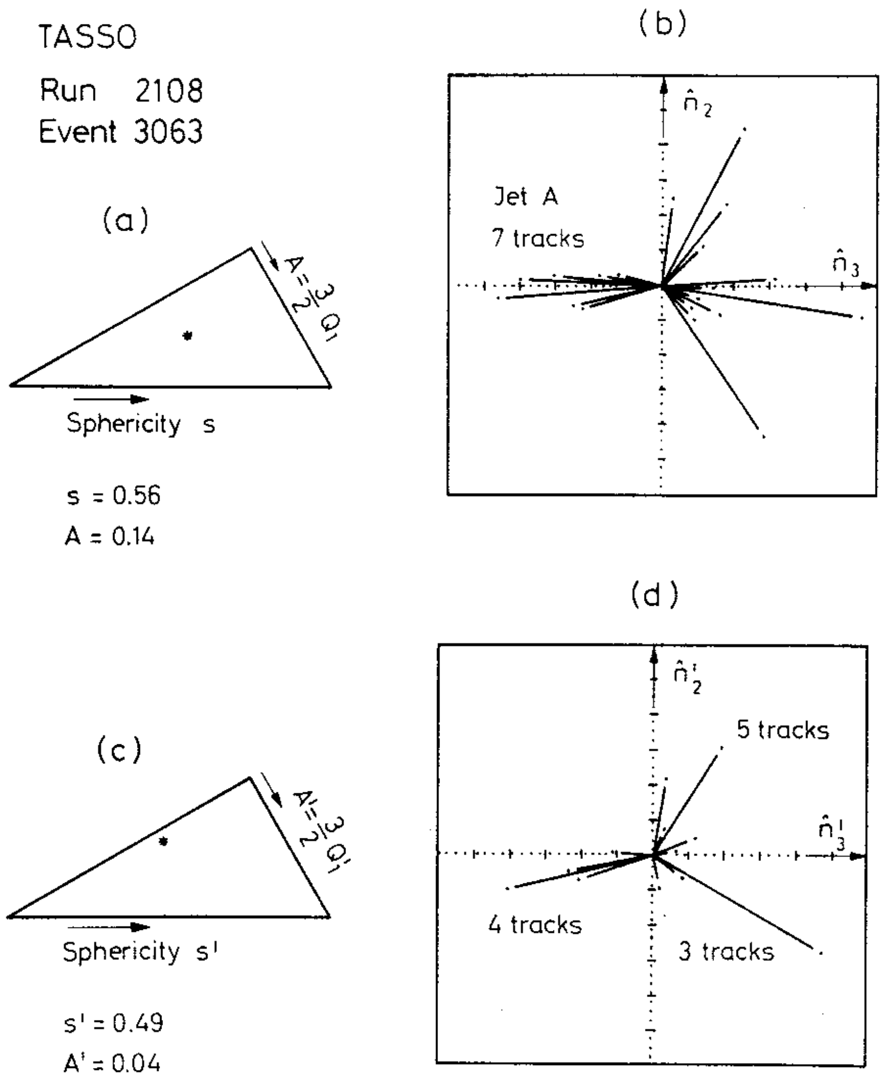

Fig. 4.31 - Application of four-jet analysis to a TASSO event:
a) position of the event in the triangular plot;
b) the event as viewed in the event plane and the identification of jet A;
c) position of the event after the removal of jet A and Lorentz transformation to the center of mass of the remaining tracks;
d) these remaining tracks as viewed on the event plane of the boosted system.

15.12.80

32107

and 8 charged tracks. Of these three, the one with 7 tracks has the smallest value of <PT'> and is hence designated as jet A (step D). After Lorentz transformation to the center-of-mass of the remaining 12 particles it is found, as shown in Fig. 4.31 (c), that the sphericity of the boosted system is still large ($S' = 0.49$), while the aplanarity of the boosted system is small ($A' = 0.04$). The second application of the three-jet analysis (step G) yields in the new event plane the three jets of Fig. 4.31 (d), consisting respectively of 3, 4, and 5 tracks. In this example, as in most cases, no reassignment of momenta (step K) is needed.

This procedure of four-jet analysis has all the advantages listed in section 4.3.2 for the three-jet analysis using the method of generalized sphericity. It has the further advantage that it requires very little additional programming on the computer. The computer time required is dominated by the two three-jet analysis of steps A and G. Since there are fewer momenta in step G than step A, the computer time of four-jet analysis is not much more than that of three-jet analysis for the same number of observed tracks. For example, with IBM 370/168 computer, this is about 2 seconds for 21 observed tracks, where the number of partitions is 1.8×10^{11}, and about 9 seconds for 35 observed tracks, where the number of partitions is 5×10^{19}!

4.5 Conclusion

It was only a little over a year ago when the first three-jet events were observed. Even at that time, the only natural explanation was e^+e^- annihilation to produce quark, antiquark, and gluon. With the accumulation of more data, the distributions can all be understood in terms of QCD models with hadronization of both quarks and gluons. Quite recently, with the determination of the spin as discussed in detail in section 4.3.5, it can now be said with confidence that the gluon has been experimentally established, in the same sense that the quark was several years ago. We are therefore beginning to explore a new deeper layer of the fundamental constituents of matter, the quarks and the gluons.

Acknowledgements

I wish to thank Professors H. Miettinen and M. Roos for their hospitality at The Arctic School of Physics. I am grateful to Professors A. Ali, D. Cassel, W. Chinowsky, J. Freeman, W. Koch, T. Meyer, G. Rudolph, G. Schierholz, P. Söding, T. Walsh, B. Wiik, G. Wolf, and G. Zobernig for helpful and stimulating discussions. Finally I would like to thank the supports of the University of Wisconsin and DESY.

References

1) J.J.Aubert et al., Phys.Rev.Lett. 33, 1404 (1974)
J.-E.Augustin et al., Phys.Rev.Lett. 33, 1406 (1974)
2) G.Goldhaber et al., Phys.Rev.Lett. 37, 255 (1976)
I.Peruzzi et al., Phys.Rev. Lett. 37, 569 (1976)
3) S.W.Herb et al., Phys.Rev.Lett. 39, 252 (1977)
W.R.Innes et al., Phys.Rev.Lett. 39, 1240 (1977)
4) M.L.Perl et al., Phys.Rev.Lett. 35, 1489 (1975)
5) G.Hanson et al., Phys.Rev.Lett. 35, 1609 (1975)
6) B.H.Wiik, Proceedings of the International Neutrino Conference, Bergen, Norway, 18-22 June 1979, p. 113
7) P.Söding, Proceedings of the European Phys.Society Intern.Conf. on High Energy Phys., Geneva, Switzerland, 27 June - 4 July, 1979, p. 271
8) TASSO-Collaboration, R.Brandelik et al., Phys.Lett. 86B, 243 (1979)
9) MARK J Collaboration, D.P.Barber et al., Phys.Rev.Lett. 43, 830 (1979)
10) PLUTO Collaboration, Ch.Berger et al., Phys.Lett. 86B, 418 (1979)
11) JADE Collaboration, W.Bartel et al., Phys.Lett. 91B, 142 (1980)
12) H.D.Bremer et al., DESY Report 80/76 (1980). For early theoretical analysis,see:
A.A.Sokolov and I.M.Ternov, Soviet Physics - Doklady 8, 1203 (1964)
V.N.Baier, Soviet Physics - Uspekhi 14, 695 (1972)
J.D.Jackson, Rev.Mod.Phys. 48, 417 (1976)
13) S.Yamada, Proceedings of the 1977 International Symposium on Lepton and Photon Interactions at High Energies, Hamburg, August 17-23, 1977
14) Jonathan Dorfan, Proceedings of the XXth International Conference on High Energy Physics, Madison, Wisconsin, USA, July 17-23, 1980 and J.M.Dorfan et al., SLAC-PUB-2566, August 1980 (to be published in Physical Review Letters)
15) R.Brandelik et al., Z.für Phys. C1, 233 (1979)
16) G.S.Abrams et al., Phys.Rev.Lett. 43, 1555 (1979)
17) Jasper Kirkby, Proceedings of the 1979 International Symposium on Lepton and Photon Interactions at High Energies, Fermilab, August 23-29, 1979
18) Y.S.Tsai, SLAC-PUB-2450 December 1979, and Proceedings of Guangzhou Conference on Theoretical Particle Physics, Jan. 5-14, 1980 Canton, People's Republic of China
19) K.Niu, Proceedings of the XXth International Conference on High Energy Physics, Madison, Wisconsin, USA, July 17-23, 1980

20) N.Ushida et al., Phys.Rev.Lett. 45, 1049 (1980) and
Phys.Rev.Lett. 45, 1053 (1980)
21) W.Bacino et al., Phys.Rev.Lett. 45, 329 (1980)
22) A.J.Lankford, Proceedings of the XXth International Conference on High Energy Physics, Madison, Wisconsin, USA, July 17-23, 1980
23) G.H.Trilling, rapporteur talk, Proceedings of the XXth International Conference on High Energy Physics, Madison, Wisconsin, USA, July 17-23, 1980
24) R.Brandelik et al., Phys.Lett. 80B, 412 (1979)
25) B.D'Almagne, Session A-11, and S.Wojcicki, rapporteur talk, Proceedings of the XXth International Conference on High Energy Physics, Madison, Wisconsin, USA, July 17-23, 1980
26) R.Ammar et al., Proceedings of the XXth International Conference on High Energy Physics, Madison, Wisconsin, USA, July 17-23, 1980
27) F.Porter, Proceedings of the XXth International Conference on High Energy Physics, Madison, Wisconsin, USA, July 17-23, 1980
28) For detail results on direct photon production at J/ψ, see:
MARK II Collaboration, SLAC-PUB-2513, June 1980 (to be published in Phys.Rev.D)
29) W.Braunschweig et al., Phys.Lett. 67B, 243 (1977)
R.Brandelik et al., Z.für Phys. C1, 233 (1979)
30) R.Brandelik et al., Phys.Lett. 74B, 292 (1978)
31) R.Partridge et al., Phys.Rev.Lett. 44, 712 (1980)
K.Berkelman, Proceedings of the XXth International Conference on High Energy Physics, Madison, Wisconsin, USA, July 17-23, 1980
32) D.L.Scharre, Proceedings of the XXth International Conference on High Energy Physics, Madison, Wisconsin, USA, July 17-23, 1980 and SLAC-PUB-2550
33) W.Bartel et al., Phys.Lett. 64B, 483 (1976) and 66B, 489 (1977)
34) G.Alexander et al., Phys.Lett. 72B, 493 (1978)
35) D.L.Scharre et al., SLAC-PUB-2514, May 1980 (to be published in Phys.Rev.Letters)
36) D.L.Scharre, SLAC-PUB-2519, May 1980 (to be published in the Proceedings of the VIth International Conference on Experimental Meson Spectroscopy, Brookhaven National Laboratory, Upton, Long Island, NY, April 25-26, 1980)
37) R.Partridge et al., Phys.Rev.Lett. 45, 1150 (1980)
38) T.M.Himel et al., Phys.Rev.Lett. 45, 1146 (1980)

39) H.F.W.Sadrozinski, SLAC-PUB-2589, August 1980 and Proceedings of the XXth International Conference on High Energy Physics, Madison, Wisconsin, USA, July 17-23, 1980
40) A.J.Lankford, Proceedings of the XXth International Conference on High Energy Physics, Madison, Wisconsin, USA, July 17-23, 1980
41) W.Schmidt-Parzefall, Proceedings of the XXth International Conference on High Energy Physics, Madison, Wisconsin, USA, July 17-23, 1980
Ch.Berger et al., Phys.Letters 93B, 497 (1980)
H.Albrecht et al., Phys.Letters 93B, 500 (1980)
B.Niczyporuk et al., LENA Collaboration, DESY 80/53, June 1980
42) K.Berkelman, rapporteur talk, Proceedings of the XXth International Conference on High Energy Physics, Madison, Wisconsin, USA, July 17-23, 1980
43) E.H.Thorndike, Proceedings of the XXth International Conference on High Energy Physics, Madison, Wisconsin, USA, July 17-23, 1980
Connell preprint CLNS - 80/464
D.Andrews et al., Phys.Rev.Lett. 45, 219 (1980) and 44, 1108 (1980)
44) J.K.Yoh, Proceedings of the XXth International Conference on High Energy Physics, Madison, Wisconsin, USA, July 17-23, 1980
G.Finocchiaro et al., Phys.Rev.Lett. 45, 222 (1980)
T.Böhringer et al., Phys.Rev.Lett. 44, 1111 (1980)
45) Ch.Berger et al., PLUTO Collaboration, Phys.Lett. 78B, 176 (1978) and 82B, 449 (1979)
S.Brandt, Proceedings of the Int. Conf. on High Energy Physics, Geneva, Switzerland, 1979
H.Meyer, Proceedings of the 1979 International Symposium on Lepton and Photon Interactions at High Energies, August 1979, Fermilab, Batavia, IL, 1979
46) C.Grupen, Proceedings of the XXth International Conference on High Energy Physics, Madison, Wisconsin, USA, July 17-23, 1980 and Internal Report SI-80-11 Siegen University, 5900 Siegen 21, Germany
K.Koller and H.Krasemann, Phys.Lett, 88B, 119 (1979)
47) C.Bebek et al., CLEO Collaboration (to be published)
48) K.Chadwich et al., CLEO Collaboration (to be published)
49) TASSO Collaboration (Presented by Sau Lan Wu) Proceedings of the XXth International Conference on High Energy Physics, Madison, Wisconsin, USA, July 17-23,1980 and R.Brandelik et al., TASSO Collaboration (to be published)

50) Ch.Berger et al., PLUTO Collaboration, DESY Report 80/34, April 1980

51) E.Hilger and TASSO Collaboration, DESY Report 80/75, July 1980

52) J.J.Sakurai, Ann.Phys. 11, 1 (1960)

53) Ch.Berger et al., PLUTO Collaboration, DESY Report 80/94, October 1980

54) R.Brandelik et al., TASSO Collaboration, Phys.Lett. 97B, 448 (1980)

55) W.Wagner, Proceedings of the XXth International Conference on High Energy Physics, Madison, Wisconsin, July 17-23, 1980

56) S.L.Wu and G.Zobernig, Particle and Fields; Z.Phys. C2, 107 (1979)

57) J.Ellis, M.K.Gaillard and G.G.Ross, Nucl.Phys. B111, 253 (1976)
T.A.DeGrand, Y.J.Ng and S-H.Tye, Phys.Rev. D16, 3251 (1977)
A.DeRujula, J.Ellis, E.G.Floratos and M.K.Gaillard, Nucl.Phys. B138, 387 (1978)

58) J.D.Bjorken and S.J.Brodsky, Phys.Rev. D1, 1416 (1970)

59) S.Brandt and H.D.Dahmen,Z.Phys. C1, 61 (1979)

60) H.J.Daum, H.Meyer, and J.Bürger, DESY Report 80/101, October 1980

61) Ch.Berger et al., PLUTO Collaboration, DESY Report 80/93 October 1980

62) P.Hoyer, P.Osland, H.E.Sander, T.F.Walsh, and P.M.Zerwas, Nucl. Phys. B161, 349 (1979)

63) A.Ali,E.Pietarinen, G.Kramer, and J.Willrodt, Phys.Lett. 93B, 155 (1980)

64) R.D.Field and R.P.Feynman, Nucl.Phys. B136, 1 (1978)
H.E.Sander and Tom Meyer, private communication

65) F.A.Berends and R.Kleiss, DESY-Report 80/73 (1980)

66) TASSO Collaboration, R.Brandelik et al., Phys.Lett. 94B, 437 (1980)

67) D.P.Barber et al., MARK J Collaboration, Phys.Lett. 89B, 139 (1979)

68) S.Yamada, Proceedings of the XXth International Conference on High Energy Physics, Madison, Wisconsin, USA, July 17-23, 1980

69) R.Brandelik et al., TASSO Collaboration, Phys.Lett. 97B, 453 (1980)

70) J.Ellis and I.Karliner, Nucl.Phys. B148, 141 (1979)

71) We have here used a higher statistical event sample than in reference 69. See J.Freeman PhD thesis 1981, Physics Department, University of Wisconsin, Madison, Wisconsin, USA

72) Ch.Berger et al., PLUTO Collaboration, DESY Report 80/78 (1980)

73) Ch.Berger et al., PLUTO Collaboration, Phys.Lett. 78B, 176 (1978)

74) K.Konishi, A.Ukawa and G.Veneziano, Phys.Lett. 80B, 259 (1979) and Nucl.Phys. B157, 45 (1979)
Y.L.Dokshitzer, D.I.T'yakonov and S.T.Troyan, Phys.Rep. 58C, 269 (1980)

75) C.L.Basham, L.S.Brown, S.D.Ellis and T.S.Love, Phys.Rev.Lett. 41, 1585 (1978); Phys.Rev. D19, 2018 (1979)

76) G.Parisi and R.Petronzio, Nucl.Phys. B154, 427 (1979)

77) A.Ali, J.G.Körner, G.Kramer, Z.Kunst, E.Pietarinen, G.Schierholz and J.Willrodt, Phys.Lett. 82B 285 (1979) and Nucl.Phys. B167, 454 (1980)
K.J.F.Gaemers and J.A.M. Vermaseren, CERN Preprint TH-2816 (1980)

78) Sau Lan Wu, DESY report 80/127 (1980)